Light-Matter Interaction in Nano-Photonic Systems: Harnessing the Weakly Interacting Emitter-Cavity System for Controlling Single Photon Emission

C. Praise Anyanwu

A dissertation
submitted in partial fulfillment of the
requirements for the degree of

Doctor of Philosophy

University of Washington

2024

Reading Committee:

David J. Masiello, Chair

Brandi M. Cossairt

Bruce H. Robinson

Program Authorized to Offer Degree:
Chemistry

University of Washington

Abstract

Light-Matter Interaction in Nano-Photonic Systems:
Harnessing the Weakly Interacting Emitter-Cavity System
for Controlling Single Photon Emission

C. Praise Anyanwu

Chair of the Supervisory Committee:
David J. Masiello
Department of Chemistry

This thesis investigates the light-matter interaction of the quantum-electrodynamic system that consists of a quantum emitter weakly interacting with a nanophotonic cavity, in order to control single-photon emission through the cavity's mode. State-of-the-art single-photon sources that are used to generate nonclassical states of light rely on strong interaction between the emitter-cavity system. This strong light-matter interaction between the two-state quantum emitter and the cavity achieves single-photon nonlinearity in the cavity's mode, such that a cavity populated with a single-photon state will repel a subsequent photon upon excitation, a mechanism often referred to as photon blockade. Thus, the cavity transmits one photon at a time. This study's principal result as presented in Chapter 2 is that photon blockade can be achieved in a cavity that is weakly interacting with a two-state quantum system, when the cavity is excited by the field of a weakly interacting scattering emitter. The scattering emitter is pumped by a laser and energy flows from the emitter to the cavity. However, the contrasting loss rates of energy dissipation between the "lossy" scattering emitter and the "low-loss", high-quality cavity yields a Fano interference, such that at the Fano antiresonant frequency, photons are blocked from flowing through the scattering emitter into the cavity. Thus the cavity populated

with a single-photon state, from weak interaction to a two-state quantum system, experiences photon blockade when excited through weak interaction with a scattering emitter under a pump-laser operating at the Fano antiresonance. This result of photon-blockade through the Fano interference mechanism is novel because it operates in the weak light-matter interaction regime, for a cavity with a linear response. This study shows that this photon blockade through the Fano interference mechanism is akin to the so called non-Hermitian photon blockade, which we generalize, and is also related to the quantum interference mechanism of the unconventional photon blockade that has been demonstrated for systems having a large degree of nonlinear response through strong intra-cavity interactions; fundamental to such systems is the cooperativity factor—that is the ratio between the light-matter interaction to the rates of energy's dissipation of the emitter-cavity system. This cooperativity factor must be greater than one, a prerequisite for photon-blockade via quantum interference.

The ability of nanophotonic cavities to confine and store light to nanoscale dimensions also has important implications for enhancing molecular, excitonic, phononic, and plasmonic optical responses. Spectroscopic signatures of processes that are ordinarily exceedingly weak such as pure absorption and Raman scattering have been brought to the single-particle limit of detection, while new emergent polaritonic states of optical matter have been realized through coupling material and photonic cavity degrees of freedom across a wide range of experimentally accessible interaction strengths. Chapters 3 and 4 present both optical and electron beam spectroscopies of cavity-coupled material systems in different light-matter interaction regimes, which provides a theoretical basis for understanding the physics inherent to each, and highlights recent experimental advances and exciting future directions.

TABLE OF CONTENTS

Page

Chapter 1: Overview on Light-Matter Interaction 1
1.0.1 The Governing Hamiltonian from First Principles 6

Chapter 2: Nonclassical Light through the Fano Antiresonance 14
2.1 State-of-the-Art Generation of Nonclassical Light 14
2.1.1 Nonclassical Light from Conventional and Unconventional Photon Blockade 14
2.1.2 Nonclassical Light from Fano Antiresonance 17
2.2 The Nonclassical Probability Distribution of the Light in the Emitter-Cavity System Laser-Excited at the Fano Antiresonance 17
2.2.1 Deconstructive Fano Interference of the Second-Order Correlation of the Fields in the Cavity-Modes at the Fano Antiresonance 20
2.2.2 Comparison Between the Photon-Blockade through Fano Antiresonance and the Unconventional Photon Blockade through Quantum Interference. 26
2.3 Theoretical Description of the Weakly Driven, Weakly Interacting Emitter-Cavity System for Photon Blockade 27

Bibliography 34

Chapter 3: Spectroscopy in Nanoscopic Cavities – Models and Recent Experiments 41
3.1 Abstract 41
3.2 Introduction 41
3.3 Weakly Coupled Systems 44
3.3.1 Fano Resonance 49
3.3.2 Absorption 51
3.3.3 Reflection, Transmission, and Electron Probes 53

3.3.4 Purcell Enhancement 55
3.3.5 Plasmonic-Photonic Coupled Systems for Emission Control . . 58
3.3.6 Surface-Enhanced Raman Scattering 58
3.4 Strongly Coupled Systems 64
3.4.1 Jaynes-Cummings Model 68
3.4.2 Characterizing Strongly Coupled Systems – Near-Field Probes 70
3.4.3 Free Electron Probes 71
3.4.4 Ultrastrong Coupling Regime 73
3.5 Summary and Future Outlook 73

Bibliography 77

Chapter 4: Nanoscale Characterization of Individual Three-Dimensional Split Ring Resonator Systems 90
4.1 Abstract 90
4.2 Introduction 91
4.3 Results and Discussion 93
4.4 Conclusion 104
4.5 Materials and Methods 105
4.6 Acknowledgements 106

Bibliography 108

ACKNOWLEDGMENTS

The author wishes to express sincere appreciation to University of Washington, where he has had the opportunity to work with the Masiello group, and to the authors Kevin C. Smith and David J. Masiello, $\alpha\rho\chi\iota\tau\acute{\epsilon}\kappa\tau\omega\nu$.

DEDICATION

To Adaku, Vincent, and Benedict Anyanwu.

Chapter 1

OVERVIEW ON LIGHT-MATTER INTERACTION

In 1865 James Clerk Maxwell published the so called Maxwell equations that illustrate the existence of electromagnetic waves traveling at the speed of light. This has led to the proposition of light being as a mode of the electromagnetic field [1]. Fundamental understanding of how the electromagnetic field interacts with matter has advanced our ability to use light to observe and manipulate matter at the atomic scale. For instance, the ion-trap procedure invented in the 1950s by Wolfgang Paul uses an oscillating electric field to trap a charged particle, about a confining saddle point of the field's harmonic potential [2]. Conversely, advances have been made in using the state of matter to manipulate light. A remarkable example being the plasmonic quasi-particles of metallic nanostructures that confine the electromagnetic field at the subwavelength nanoscale, and thereby facilitating strong light-matter interactions [3, 4, 5].

Later on, in 1946 Edward Purcell's seminal work on nuclear magnetic resonances showed that there is an increase in the relaxation rate of a single magnetic spin interacting with an electric current of a resonant circuit, as opposed to the non-interacting magnetic spin in vacuum [6], a phenomenon now known as the Purcell enhancement. This discovery has led to the understanding that the electromagnetic environment, that is the electromagnetic local density of states, can greatly influence the relaxation rate—the rate of spontaneous emission of radiation by an excited state of matter. This insight has given rise to a new frontier of studying light-matter interactions in a controllable context, which in turn has launched the development of

cavity quantum electrodynamics, i.e., the study of light-matter interactions between individual atoms and the spatially confined resonant electromagnetic modes of a cavity resonator, e.g. the Fabry-Pérot cavity, as shown in Fig. 1.2 [7].

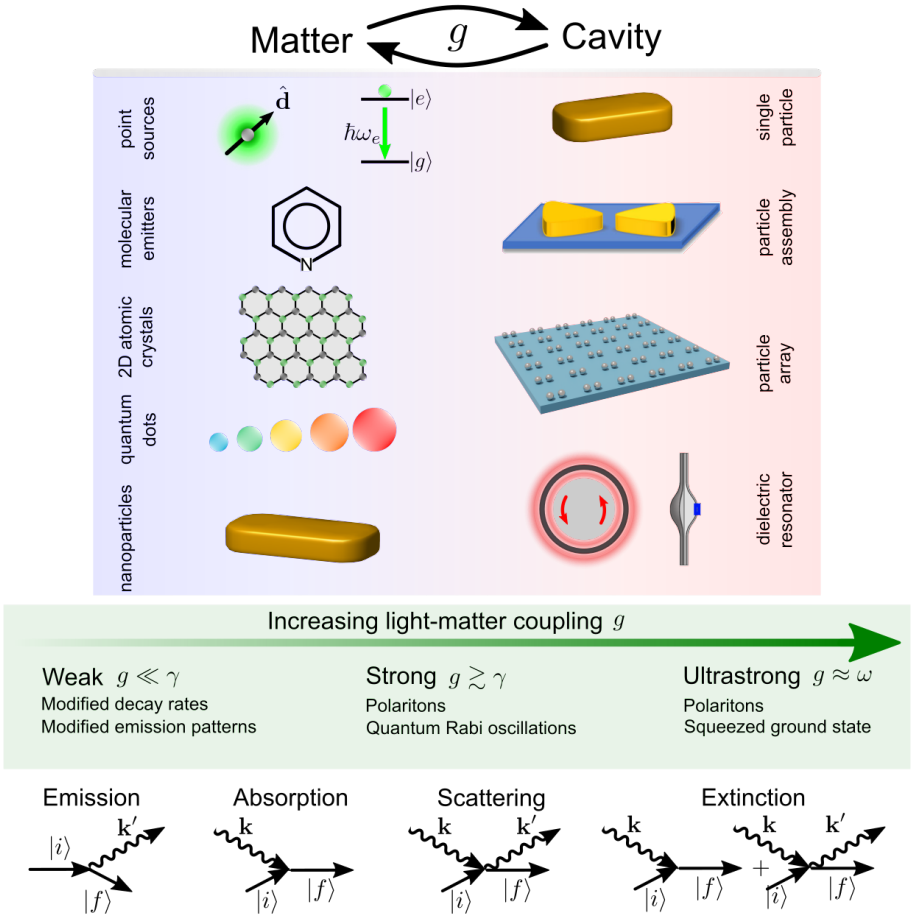

Figure 1.1: Overview of coupled light-matter degrees of freedom involving atomic, molecular, excitonic, plasmonic, and phononic material components interacting with individual, composite, and structured nanophotonic cavity environments. The degree of light–matter coupling (g) relative to loss (γ) dictates the observed physical characteristics of each system. Displayed at the bottom are diagrammatic representations of familiar light–matter interaction processes which may be probed using both far-field and near-field optical and electron beam sources. The sinusoidal arrows represent photons of wavevector $\mathbf{k}$ and $\mathbf{k}'$, while the straight arrows represent initial and final material states labeled by $|i\rangle$ and $|f\rangle$, respectively. Panels reproduced with permission from Reference [8].

In 2005, Birbaum et al. [9] demonstrated the trapping of a single atom in an optical cavity, thereby overcoming the inherent weak interaction between light and atom. (Such weak interaction between light and atom stems from the fact that the absorption cross-section of an atom is so small [10], on the order of the fine-structure constant.) However, the multiple reflections of the light's field in the cavity's walls increases the probability of absorption by the trapped atom, and thus increases the interaction strength between the atom and the cavity's field. Such a system with strong light-matter interactions has led to the successful experimental investigation of fundamental concepts as the Rabi-frequency (the frequency at which the probability amplitude of the atom's two-state system, ground and first excited states, fluctuate in the resonant electromagnetic field), and as well to the generation of hybrid light-matter states known as polaritons, depicted in Fig 1.2. Significantly, the electric field's potential of this hybrid light-matter state is anharmonic, and exhibits an important phenomenon known as single-photon blockade, where by when a single photon populates the electromagnetic field of the strongly coupled atom-cavity system, then a subsequent photon is repelled, as such, the system can transmit only a single photon at a time.

Matter systems, such as single atoms, Rydberg atoms, quantum dots, nitrogen-vacancy centers, and transition-metal dichalcogenides that behave as effective two-state quantum system, are often strongly coupled to the electromagnetic modes of a cavity in order to achieve single-photon blockade, and thus, serve as single-photon sources [11, 12, 13, 14, 15]. Encoding information in the state of a single photon (using degrees of freedom of polarization, momentum, or energy) is highly desirable in secure quantum communication since photons travel at the speed of light and interact weakly with the environment over long distances [16, 17]. For example, in the quantum key distribution protocol, Alice encodes information in the qubit of a photon polarization state that is securely transmitted through a quantum channel to Bob [18].

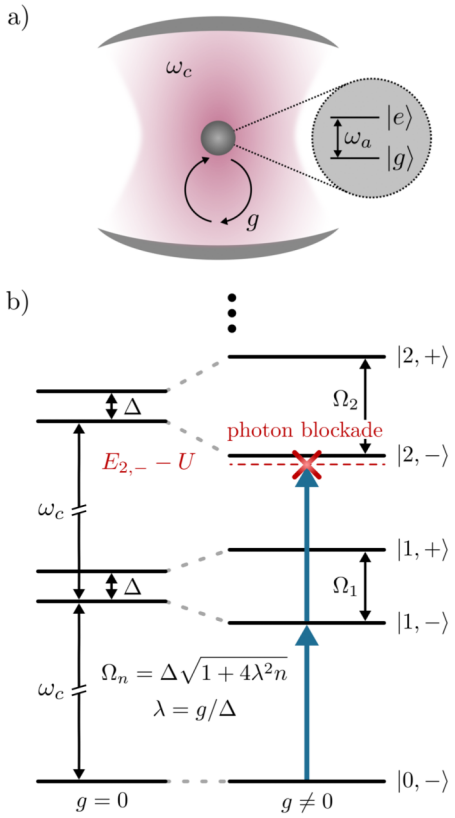

Figure 1.2: a.) A Fabry-Pérot cavity resonator whose resonance frequency is ω_c. This cavity's field interacts with a two-state quantum system whose excitation frequency is ω_a. Quanta of energy is exchanged between the mode of the cavity's field and the dipole excitation of the two-state system at the rate g. For a cavity's field with a single mode, this is the so called Jaynes-Cummings system. b.) The eigenspectrum of the Jaynes-Cummings Hamiltonian with detuned matter, cavity frequencies, i.e. $\Delta = \omega_a - \omega_c$. The left set of horizontal black lines indicates the eigenenergies of the bare cavity mode and two-state system, while the right portrays the impact of light-matter coupling. Pairs of states with the same total number of excitations n hybridize to form new pairs of eigenstates $|n, \pm\rangle$ known as polaritons, which are split by the Rabi-frequency Ω_n. For the hybridized system that begins in the ground state $|0, -\rangle$, absorption of one photon of frequency $(E_{1,-} - E_{0,-1})$ prohibits absorption of a second of the same frequency due to the additional energy cost U. This phenomenon is known as photon blockade, and may be used to realize effective photon-photon interactions and single-photon transmission through cavity mode. Figure reproduced with permission from Reference [19]

In this study, we investigate the possibility to achieve single-photon blockade in the regime of weak light-matter interaction within an emitter-cavity system. The emitter is the matter having an effective two-state system, due to a large degree of nonlinearity in its anharmonic potential, which makes other excited states inaccessible. Strong interaction between the emitter and the field of the cavity's mode is required in order to achieve the same degree of anharmonicity, and therefore single-photon blockade in the field of the cavity's mode. However, here we employ a well-known phenomenon in the weak interaction regime known as Fano interference as a means to construct, in general, a nonclassical state of light in that field of the cavity's mode that is weakly nonlinear. This is the thesis focus, which is presented in Chapter 2. Broadly speaking, the thesis illustrates that a nonclassical state of light can be transmitted through an emitter-cavity system that is in the weak interaction regime, when a laser excites the emitter-cavity system at the Fano antiresonance.

The Fano effect was originally observed in the autoionization spectrum of Helium vapor by Silverman and Lassettre [20] in 1959. Fano understood the pronounced asymmetric lineshape observed in that spectrum was due to the interaction of two electronic configurations of He [21]—the discrete $2s2p$ double excitation, which is above the first ionization threshold, and the subsequent autoionization to the continuum. In the years that have followed, such asymmetric lineshapes (now called Fano antiresonances, Fano resonances, or Fano interferences) have been observed in many different physical systems characterized under both optical [22, 23, 24, 25, 26] and electron beam [27, 28, 29, 30] probes whenever discrete and continuum channels weakly interact. In such cases, the spectrum of the interacting system taken in ratio to the spectrum of the continuum channel can be arranged as $\sigma_{\text{interaction}}(\omega)/\sigma_{\text{continuum}}(\omega) = |(q_F + \epsilon)/(\epsilon + i)|^2$, where the Fano asymmetry parameter q_F is a frequency-independent number in the vicinity of the antiresonance that can be positive, negative, or zero and completely characterizes the asymmetry of the lineshape, while ϵ is a reduced frequency taken with respect to the frequency of the

discrete mode.

The thesis periphery as given by Chapter 3 and 4 details spectroscopic techniques in nanoscopic cavities. In particular, emphasis is given to spectroscopic observations of weakly and strongly interacting plasmonic, excitonic, molecular, and nanophotonic cavity-systems reported in the recent literature (Figure 1.1) [8, 31]. Spectroscopic observables of relevance include both near-field (nanoscale Fourier transform infrared) and far-field (absorption, Surface-enhanced Raman scattering) optical measurements, as well as those based upon the inelastic scattering of focused electron beams, such as electron energy loss, electron energy gain, and cathodoluminescence spectroscopies performed in an electron microscope.

1.0.1 The Governing Hamiltonian from First Principles

Here we present the general theory for describing a system of charged particles interacting with the electromagnetic field. Without specifying the underlying details *a priori* this description can be applied to various platforms comprising electromagnetic and matter degrees of freedom as presented in the succeeding chapters of this work, and allows for either a classical or quantum mechanical description depending on the particular problem we shall address. Comprehensive study on the approach presented here is detailed in the following references [32, 33, 34, 35]. Based on Hamilton's principle, the Lagrangian $L = T - V$ describes the relationship between the kinetic and potential energies, T and V respectively, of a mechanical system. First we apply the Lagrangian approach to the electromagnetic field and illustrate its wave-like behavior from Maxwell equations. Thereafter we consider the interactions between the fields and the charged particles that produce the fields. Then under the Legendre transformation, we derive the light-matter system's Hamiltonian $H = T + V = E$ that expresses the conservation of energy and that further allows for the field's quantization.

Given the electromagnetic field's Lagrangian

$$\begin{aligned} L_{\text{field}} &= \int \frac{\mathrm{d}x^3}{8\pi} \left[\epsilon(\mathbf{x})\mathbf{E}^2 - \mathbf{B}^2\right] \\ &= \int \frac{\mathrm{d}x^3}{8\pi} \left[\epsilon(\mathbf{x})\frac{\dot{\mathbf{A}}^2}{c^2} - (\nabla \times \mathbf{A})^2\right]. \end{aligned} \tag{1.1}$$

where the electric field has been expressed in terms of the potential $\mathbf{A}$ from a source whose current produces the field such that $\mathbf{E} = -\dot{\mathbf{A}}/c$, and Maxwell equation tells us that $\mathbf{B} = \nabla \times \mathbf{A}$. Of interest is the fact that this potential $\mathbf{A}(\mathbf{x}, t)$ can be expanded in terms of the a time-dependent amplitude $q(t)$ that yields the harmonic motions of the electromagnetic wave in a dielectric medium $\epsilon(\mathbf{x})$, and a spatial part $\mathbf{f}(\mathbf{x})$ (referred to as the mode function) that yields the profile of the electromagnetic field, such that

$$\mathbf{A}(\mathbf{x}, t) = \sum_m \frac{c\sqrt{4\pi}}{V_m} q_m(t)\mathbf{f}_m(\mathbf{x}). \tag{1.2}$$

For example, $\mathbf{f}_m(\mathbf{x})$ describes the set of modes of standing waves on a string or a dielectric medium of a Fabry-Pérot cavity, where $m = 1, 2, 3, ...,$ denotes the fundamental and overtone modes, and V_m is the normalized modal volume of the bounded region in which the mode exists, defined as

$$V_m = \frac{\int \mathrm{d}^3x\, \epsilon(\mathbf{x})|\mathbf{E}_m|^2}{\max\{\epsilon(\mathbf{x})|\mathbf{E}_m|^2\}} = \int \mathrm{d}^3x\, \epsilon(\mathbf{x})|\mathbf{f}_m(\mathbf{x})|^2. \tag{1.3}$$

The harmonic nature of the electromagnetic wave is revealed upon expressing the Lagrangian in terms of the temporal and spatial expansion of the field's potential, such that

$$\begin{aligned} L_{\text{field}} &= \frac{1}{2}\sum_{m,n} \int \mathrm{d}^3x \left[\frac{\dot{q}_m\dot{q}_n}{V_mV_n} \underbrace{\epsilon\mathbf{f}_m(\mathbf{x}) \cdot \mathbf{f}_n(\mathbf{x})}_{\delta_{mn}} - c^2\frac{q_mq_n}{V_mV_n} \underbrace{(\nabla \times \mathbf{f}_m(\mathbf{x})) \cdot (\nabla \times \mathbf{f}_n(\mathbf{x}))}_{\mathbf{f}_m(\mathbf{x})\cdot(\omega_n^2/c^2)\mathbf{f}_n(\mathbf{x})}\right] \\ &= \frac{1}{2}\sum_m \left[\frac{1}{V_m}\dot{q}_m(t)^2 - \frac{1}{V_m}\omega_m^2 q_m(t)^2\right], \end{aligned} \tag{1.4}$$

where the first term corresponds to the analogous mechanical oscillator with the kinetic energy $m\dot{\mathbf{x}}(t)^2$ while the second term corresponds to its harmonic potential energy $m\omega^2 x(t)^2$ with the resonance frequency ω; however in the above equation $q_m(t)$ is a generalized coordinate of the mode m.

The Interaction of the Electromagnetic Fields from Two Dielectric Media

Next let us consider the interaction of the electromagnetic fields from two dielectric media denoted by $\epsilon_1(\mathbf{x})$ and $\epsilon_2(\mathbf{x})$, with each medium containing a single mode—without loss of generality. Since the fields abide by the superposition principle, such that, the displacement field $\mathbf{D}$ of the dielectric media is given by

$$\mathbf{D} = \epsilon_1 \mathbf{E}_1 + \epsilon_2 \mathbf{E}_2 \tag{1.5}$$

it follows that

$$\begin{aligned} L_{\text{field}-\text{interaction}} &= \int \frac{\mathrm{d}^3 x}{8\pi} \left[\mathbf{D}\cdot\mathbf{E} - \mathbf{B}^2\right] \\ &= \sum_{i=1,2} \int \frac{\mathrm{d}^3 x}{8\pi} \left[\underbrace{\epsilon_i \mathbf{E}_i^2 - \mathbf{B}_i^2}_{L_{\text{field}}} + \underbrace{(\epsilon_1+\epsilon_2) 2\mathbf{E}_1\cdot\mathbf{E}_2 - 2\mathbf{B}_1\cdot\mathbf{B}_2}_{L_{\text{interaction}}} \right]. \end{aligned} \tag{1.6}$$

Considering the part of the Lagrangian describing the field's interaction, in terms of the time-dependent amplitudes and the mode functions, yields the electric and magnetic interaction constants, such that

$$\begin{aligned} L_{\text{interaction}} &= \int \frac{\mathrm{d}^3 x}{8\pi} (\epsilon_1+\epsilon_2) 2\mathbf{E}_1\cdot\mathbf{E}_2 - 2\mathbf{B}_1\cdot\mathbf{B}_2 \\ &= \frac{1}{2}\sum_{m,n} \frac{1}{\sqrt{V_{1m}V_{2n}}} \left[g^{(E)}_{mn} \dot{q}_{1m}\dot{q}_{2n} - g^{(M)}_{mn} q_{1m} q_{2n}, \right] \end{aligned} \tag{1.7}$$

where the electric and magnetic constants $g^{(E)}_{mn}$ and $g^{(M)}_{mn}$ are [36]:

$$\begin{aligned} g^{(E)}_{mn} &\approx \frac{1}{\sqrt{V_{1m}V_{2n}}} \int \mathrm{d}^3 x \, (\epsilon_1+\epsilon_2) \mathbf{f}_{1m}(\mathbf{x})\cdot\mathbf{f}_{2n}(\mathbf{x}) \\ g^{(M)}_{mn} &= \frac{1}{\sqrt{V_{1m}V_{2n}}} \int \mathrm{d}^3 x \, (\omega^2_{1m}\epsilon_1 + \omega^2_{2n}\epsilon_2) \mathbf{f}_{1m}(\mathbf{x})\cdot\mathbf{f}_{2n}(\mathbf{x}). \end{aligned} \tag{1.8}$$

Note that the interaction constants depend both on the mode overlap of the field profiles from the dielectric media, i.e., $\mathbf{f}_{1m}(\mathbf{x}) \cdot \mathbf{f}_{2n}(\mathbf{x})$; and the mode volume $V_{m,n}$. For free space fields the mode volume is large, and thus diminishes the degree of light-light interactions; on the other hand nano-photonic systems have the ability to couple with light and thus confine the fields within nanoscale dimensions, thus providing a platform for strong interaction of the electromagnetic fields (as discussed in Chapters 3 and 4).

Also, this interaction term $L_{\text{interaction}}$ illustrates how the electromagnetic field interacts with a state matter that produces such a field. Consider the case where the electric and magnetic fields $\mathbf{E}_1$ and $\mathbf{B}_1$ are produced by the electric and magnetic dipole-sources $\mathbf{d}_1$ and $\mathbf{m}_1$ of charged particles centered at $\mathbf{r}_0$. Within the vicinity of the dipole-source, the field's profile is identical to the state of matter which produces it, such that, $\mathbf{E}_1(\mathbf{x}) = \mathbf{d}_1 \delta(\mathbf{x} - \mathbf{x}_0)$ [1]. Thus for such a case we find that $L_{\text{interaction}}$ yields the light-matter interaction:

$$\begin{aligned} L_{\text{interaction}} &= \int \frac{\mathrm{d}^3 x}{8\pi} \left[2\epsilon_1 \mathbf{E}_1(\mathbf{x}_0) \cdot \mathbf{E}_2(\mathbf{x}_0) - 2\mathbf{B}_1(\mathbf{x}_0) \cdot \mathbf{B}_2(\mathbf{x}_0) \right] \\ &= \mathbf{d}_1 \cdot \mathbf{E}_2 - \mathbf{m}_1 \cdot \mathbf{B}_2. \end{aligned} \tag{1.9}$$

The Electromagnetic Field Interacting with Matter

Formally, the Lagrangian describing the light-matter system can be partitioned as follows: $L = L_{\text{matter}} + L_{\text{field}} + L_{\text{interaction}}$, where

$$L = \underbrace{\sum_i \frac{1}{2} m_i \dot{\mathbf{r}}_i^2 - V_{\text{Coulomb}}}_{L_{\text{matter}}} + \underbrace{\int \frac{d^3 x}{8\pi} \left[\epsilon(\mathbf{x}) \frac{\dot{\mathbf{A}}^2}{c^2} - (\nabla \times \mathbf{A})^2 \right]}_{L_{\text{field}}} + \underbrace{\frac{1}{c} \sum q_i \dot{\mathbf{r}}_i \cdot \mathbf{A}(\mathbf{r}_i)}_{L_{\text{interaction}}}. \tag{1.10}$$

The first part is the kinetic energy of the system of charged particles at position $\mathbf{r}_i$ where the total potential is the Coulomb potential defined by $V_{\text{Coulomb}} = 1/2 \int \mathrm{d}^3 x \rho_f \Phi$. The second part is the energy of the electromagnetic field confined

within the cavity's dielectric medium with the relative electric permittivity constant $\epsilon(\mathbf{x}) = 1 + 4\pi\chi(x)$, such that in the radiation gauge:

$$\begin{aligned} \epsilon(\mathbf{x})\mathbf{E} &= -\epsilon(\mathbf{x})\frac{\dot{\mathbf{A}}}{c} \\ \mathbf{B} &= \nabla \times \mathbf{A}. \end{aligned} \tag{1.11}$$

where $\mathbf{A}$ is the vector potential of the field defined above.

The third part $L_{\text{interaction}}$ is the interaction energy between the matter's charged particles and the cavity's electromagnetic field's potential $\mathbf{A}(\mathbf{r}_i)$ evaluated at the positions of the charged particles $\mathbf{r}_i$. From this, one can show that the interaction energy is due to the transition dipole moment of the matter's charged particles and the electromagnetic field of the cavity. To see this it is instructive to consider the limiting case where the spatial extent of the charged particles given by the scale a is much less than the wavelength λ of the electromagnetic field ($\lambda \gg a$). Then, the field felt by the system is constant and position independent such that

$$\begin{aligned} L_{\text{interaction}} &= \frac{1}{c}\sum q_i \dot{\mathbf{r}}_i \cdot \mathbf{A}(\mathbf{r}_i) \\ &\approx \frac{1}{c}\sum q_i \dot{\mathbf{r}}_i \cdot \mathbf{A}(\mathbf{r}_0) \\ &= \frac{1}{c}\dot{\mathbf{d}} \cdot \mathbf{A}(\mathbf{r}_0), \end{aligned} \tag{1.12}$$

where the constant potential is now evaluated at $\mathbf{r}_0$ the center of mass of the particles in the long-wavelength (dipole) approximation, and $\mathbf{d} = \sum q_i \mathbf{r}_i$ is the net dipole moment of the matter's system about $\mathbf{r}_0$. Finally, recalling that a total time derivative can be added to the Lagrangian, which leaves the system's evolution unchanged according to the principles of least action [35], then we arrive at the result that

$$\begin{aligned} L_{\text{interaction}} &= \frac{1}{c}\dot{\mathbf{d}} \cdot \mathbf{A}(\mathbf{r}_0) + \frac{1}{c}\frac{\mathrm{d}}{\mathrm{d}t}(\mathbf{d} \cdot \mathbf{A}(\mathbf{r}_0)) \\ &= -\frac{1}{c}\mathbf{d} \cdot \dot{\mathbf{A}}(\mathbf{r}_0) \\ &= \mathbf{d} \cdot \mathbf{E}(\mathbf{r}_0). \end{aligned} \tag{1.13}$$

The Hamiltonian for the Electromagnetic Field Interacting with a Two-State Quantum System

Next, we make a connection between the Lagrangian and the Jaynes-Cummings model that describes the two-state quantum system of matter interacting with a single mode of the cavity's electromagnetic field. The Legendre transformation from the generalized coordinate to the generalized momenta $(\mathbf{r},\, \dot{\mathbf{r}}) \rightarrow (\mathbf{r},\, \mathbf{p})$ allows us to define the Hamiltonian in order to quantize the system. Thus, defining the conjugate momenta to the matter and field coordinates as

$$\begin{aligned} p_{ik} &= \frac{\partial L}{\partial \dot{r}_{ik}} = m_i \dot{r}_{ik} \\ \Pi_k &= \frac{\partial \mathcal{L}}{\partial \dot{A}_k} = \frac{\epsilon(\mathbf{x})}{4\pi c^2}\dot{A}_k - (d_k/c)\delta(\mathbf{r}-\mathbf{r}_0) \end{aligned} \tag{1.14}$$

yields the following Hamiltonian

$$\begin{aligned} H &= \sum_i \frac{\mathbf{P}^2}{2m_i} + V_{\text{Coulomb}} + \int \frac{d^3x}{8\pi}\left[\frac{(4\pi c)^2}{\epsilon(\mathbf{x})}\mathbf{\Pi}^2 + (\nabla \times \mathbf{A})^2\right] \\ &\approx \underbrace{\sum_i \frac{\mathbf{P}^2}{2m_i} + V_{\text{Coulomb}}}_{H_{\text{matter}}} + \underbrace{\int \frac{d^3x}{8\pi}\left[\epsilon(\mathbf{x})\mathbf{E}^2 + \mathbf{B}^2\right]}_{H_{\text{field}}} + \underbrace{\mathbf{d}\cdot\mathbf{E}}_{H_{\text{interaction}}} . \end{aligned} \tag{1.15}$$

Then the Jaynes-Cummings Hamiltonian can be derived by expanding the above matter-field Hamiltonian in terms of the ground state $|g\rangle$ and the excited state $|e\rangle$ of the two-state quantum system [33], such that

$$\begin{aligned} H_{\text{matter}} &= (|g\rangle\langle g| + |e\rangle\langle e|)H_{\text{matter}}(|g\rangle\langle g| + |e\rangle\langle e|) \\ &= \hbar\omega_g |g\rangle\langle g| + \hbar\omega_e |e\rangle\langle e| \\ &\equiv \hbar\omega_e/2\,(1|e\rangle\langle e| - 0|g\rangle\langle g|)\,, \end{aligned} \tag{1.16}$$

where the zero of energy is set to the ground state energy $\hbar\omega_g = 0$, and the resonance energy of transition between the two-state system of the matter is $\hbar\omega_e$. Carrying out the same expansion for the matter-field interaction term yields

$$\begin{aligned} H_{\text{interaction}} &= (|g\rangle\langle g| + |e\rangle\langle e|)\mathbf{d}(|g\rangle\langle g| + |e\rangle\langle e|)\cdot\mathbf{E} \\ &= \langle g|\mathbf{d}|e\rangle \cdot \mathbf{E}\Big(|g\rangle\langle e| + |e\rangle\langle g|\Big), \end{aligned} \tag{1.17}$$

where $\langle g|\mathbf{d}|e\rangle = \langle e|\mathbf{d}|g\rangle$ is the matrix element of the transition dipole moment between the two-state system of the matter. Finally, defining the quantized single-mode electromagnetic field [37],

$$\begin{aligned} \int \frac{d^3x}{8\pi}\left[\epsilon(\mathbf{x})\mathbf{E}^2 + \mathbf{B}^2\right] &= \hbar\omega_c\left(\hat{a}^\dagger\hat{a} + 1/2\right) \\ \mathbf{E} &= \sum_\lambda \hat{\mathbf{e}}_\lambda\left(\mathcal{E}\hat{a} + \mathcal{E}^*\hat{a}^\dagger\right) \\ \mathbf{B} &= c/\omega\sum_\lambda \mathbf{k}\times\hat{\mathbf{e}}_\lambda\left(\mathcal{E}\hat{a} + \mathcal{E}^*\hat{a}^\dagger\right), \end{aligned} \tag{1.18}$$

with the creation and annihilation operators $\hat{a}, \hat{a}^\dagger$ associated with the amplitude of the single-mode electromagnetic field having the unit vector of polarization $\hat{\mathbf{e}}_\lambda$, the modal amplitude $\mathcal{E}$ and the resonance energy in the cavity's dielectric medium $\hbar\omega_c$, thus yields the fully quantized Hamiltonian

$$H = \underbrace{\frac{\hbar\omega_e}{2}\hat{\sigma}_z}_{H_{\text{matter}}} + \underbrace{\hbar\omega_c\left(\hat{a}^\dagger\hat{a} + 1/2\right)}_{H_{\text{field}}} + \underbrace{\hbar g(\hat{a} + \hat{a}^\dagger)(\hat{\sigma}_+ + \hat{\sigma}_-)}_{H_{\text{interaction}}}, \tag{1.19}$$

where the Pauli-matrix operator $\hat{\sigma}_+ = |e\rangle\langle g|$ denotes the transition from the ground state to the excited state upon the matter's interaction with the field, and vice-versa for $\hat{\sigma}_- = |g\rangle\langle e|$. The matter-field interaction constant is defined as

$$g = \frac{\langle g|\mathbf{d}|e\rangle\cdot\mathbf{e}_\lambda\mathcal{E}}{\hbar}, \tag{1.20}$$

which, for a resonant excitation, defines the Rabi-frequency $\Omega_{\text{n}} = |g|2\sqrt{n}$ of energy exchange between the matter-field polaritonic states in the strong light-matter interaction regime (see Fig. 1.2). Neglecting the constant term $\hbar\omega_c/2$ that does not contribute to the system's dynamics, and then transforming into the co-rotating frame (as described in the theoretical section of Chapter 2 and in [33]) with the rotating wave approximation, thus yields the Jaynes-Cummings Hamiltonian describing a two-state quantum system of matter interacting with a single-mode electromagnetic field:

$$H = \underbrace{\frac{\hbar\omega_e}{2}\hat{\sigma}_z}_{H_{\text{matter}}} + \underbrace{\hbar\omega_c\hat{a}^\dagger\hat{a}}_{H_{\text{field}}} + \underbrace{\hbar g(\hat{a}^\dagger\hat{\sigma}_- + \hat{a}\hat{\sigma}_+)}_{H_{\text{interaction}}}. \tag{1.21}$$

The description of the Jaynes-Cummings Hamiltonian is applicable to the evolution of the emitter-cavity system discussed in Chapter 2, for the generation of nonclassical light in the weak light-matter interaction regime.

Chapter 2

NONCLASSICAL LIGHT THROUGH THE FANO ANTIRESONANCE

2.1 State-of-the-Art Generation of Nonclassical Light

A fundamental example of a nonclassical state of light is the single-photon state radiated by a quantum emitter. The basic idea for generating single photons on demand in state-of-the-art approaches involves the pulsed excitation of a single quantum emitter, and thereafter, filtering of the emitted single-photon with the desired properties [38]. A scheme for selecting the desired single-photon involves embedding the quantum emitter in an optical cavity that has a high-quality factor and a small mode volume, in order to improve the efficiency, direction, polarization, and ultimately the indistinguishability of the single-photon emitted. This is often achieved by the resonant excitation of the cavity that strongly interacts with the emitter; such strong interaction induces a photon blockade at the Rabi-frequency of the coupled emitter-cavity system that guarantees the desired single-photon emission [9, 39, 40, 41, 42]. It is known that epitaxial III-V semiconductor quantum dots in cavities have been the leading platform for nonclassical light generation. However not only does this system suffer from large inhomogeneous broadening [39] that prevents scaling of the system to large generation of many indistinguishable single photons, it also suffers from the need of cryogenic temperatures, in only which the quantum dot can operate [38].

2.1.1 Nonclassical Light from Conventional and Unconventional Photon Blockade

Having smaller inhomogeneous broadening and the ability to operate at room temperature, color-centers in group IV semiconductors have recently emerged as alternative

quantum emitters. (c.f. Beverators et al. 2002b; Neu et al, 2011; Rogers et al., 2014; Widmann et al., 2015 in [38].) Although ensembles of color-centers in group IV semiconductor cavities present a promising platform for the implementation of new regimes of photon blockade, there is still the challenge imposed by the requirements of the photon blockade mechanism: strong light-matter interaction between the optical mode of the cavity and the dipole mode of the quantum emitter. Achieving such strong light-matter interaction between the emitter-cavity system requires such complex experiments of ion-trapping in order to place the quantum emitter in the optimal region of the cavity's spatial mode profile [9]. More so, this strong interaction is a prerequisite for the unnatural degree of nonlinearity that the coupled cavity system must have in order to achieve photon blockade, and thus single-photon transmission through the optical mode of the cavity.

Recently, an unconventional photon blockade (UPB) mechanism has emerged as a companion approach towards generating nonclassical light [43, 44]. The nature of this UPB mechanism is such that the need for an unnaturally high degree of nonlinearity is relaxed. The UPB framework could be applied to a silicon photonic cavity where the $\chi^{(3)}$ response naturally yields a weakly nonlinear Kerr-medium. [45, 46] (c.f. refs. 20, 35, 36 in [43]) The key requirement is to couple at least two optical cavity modes with one of the modes having a non-negligible degree of nonlinearity, in order to assist quantum interference between excitation pathways [47, 48, 46, 43]. Thus by means of a coupled pair of driven-dissipative Kerr-resonators —with an arbitrarily small single-photon Kerr-nonlinearity —this UPB framework can achieve the non-Guassian (nonclassical) state of light that has a strongly sub-Poissonian photon statistics, a signature often referred to as photon antibunching. Although the drawback is to work with a pair of intracavity modes having fields below unity occupation, and to accept a probabilistic single-photon emission, it is still a promising pathway for integrable and scalable single-photon source because it forgoes the need for the large degree of single-photon nonlinearity afforded by quantum emitters.

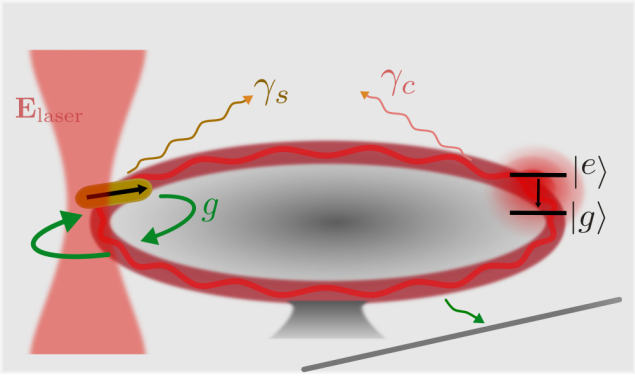

Figure 2.1: A schematic of a mode of a microresonator (cavity), that is weakly interacting with a two-state quantum system, which populates the cavity with a single-photon state. Excitation of the cavity occurs through weak interaction with a scattering emitter (here depicted as a metallic nanoparticle) that is laser-excited by $\mathbf{E}_{\text{laser}}$. The rate of energy exchange between the laser-excited emitter and the cavity is given by g which is proportional to the emitter-cavity interaction energy. Here, γ_s and γ_c are the rates of energy's dissipation from the scattering emitter and the cavity to the environment. In the regime of weak emitter-cavity interaction, such that $\gamma_c \gg g > \gamma_s$, then Fano interference can result to photon blockade in the cavity's mode, when the system is excited at the Fano antiresonance.

Evidence of the UPB system as a viable path for single-photon emission has been successfully demonstrated [44] [cite the one from Science]. However, there are two accepted technical challenges involved in the experimental realization of UPB [43]: (i.) the optimal sub-Poissonian photon statistics is obtained only for certain parameter regimes of the cavity-cavity interaction strength, the nonlinearity, and the pump-laser detuning with respect to the cavity, and thus requires fine tuning of these parameters of the system [45, 46] (ii.) the weak nonlinearity imposes a need for strong intracavity interaction that results in fast oscillation of the achieved nonclassical light; this oscillation is on a time scale much smaller than the cavity's lifetime, which makes it difficult to detect the nonclassical light.

2.1.2 Nonclassical Light from Fano Antiresonance

Leveraging the aforementioned works, this study envisions the feasible QED-like system that incorporates a photonic mode of a microcavity weakly interacting with the dipole mode of an emitter (see Fig. 2.1, top panel). This system is akin to that of the hybrid metallodielectric cavity, c.f. [49, 50, 51, 22, 52, 53, 54] in [55], where the contrasting losses (that is the rate of energy's dissipation) between the scattering emitter and high-quality cavity yields a Fano resonance upon weak interaction. This Fano resonance has recently provided a novel platform for single-photon emission experiments [56, 57] that differs from the unconventional-photon-blockade counterpart because it bypasses not only the need for a high degree of nonlinearity in the cavity's degrees of freedom, but also the need for a strong light-matter interaction between the emitter-cavity system.

Here we illustrate how the deconstructive Fano interference occurring at the antiresonant frequency can be used to achieve photon blockade in a high-quality cavity that is excited through weak interaction with a scattering emitter, as illustrated in Fig. 2.1. Here, the cavity has a negligible degree of nonlinearity, and the cavity is under weak interaction with a two-state quantum system (where the two-state quantum system is the source of single photon emission in the cavity). This hitherto missing description of photon-blockade through Fano interference—which we also show is akin to the recently explored non-Hermitian photon blockade [57] —stands to harness the degree of antibuching and thus the purity of the single-photon state observed in the experiment [56].

2.2 The Nonclassical Probability Distribution of the Light in the Emitter-Cavity System Laser-Excited at the Fano Antiresonance

To determine the nonclassical nature of the light transmitted through the emitter-cavity system, we calculate the photon-statistics. The coherent state of light from a laser is characterized by a field whose amplitude has a spatial probability distribu-

tion that is Poissonian, i.e., the mean squared deviation (the variance) of the field's amplitude is equal to the square of the mean field's amplitude [58, 59], i.e.

$$\langle I(t,\omega)I(t+\tau,\omega)\rangle - \langle I(t,\omega)\rangle^2 = \left[g^{(2)}(t,\tau,\omega)-1\right]\langle I(t,\omega)\rangle^2. \tag{2.1}$$

where $\langle I(t,\omega)\rangle^2$ is the square of the mean field's amplitude; and $\langle I(t,\omega)I(t+\tau,\omega)\rangle$ is the variance of the field's amplitude. This variance is determined by the mean-product of the split-beam from the light source, where the field's intensity count $I(t,\omega)$ is measured at one detector at a time t, and $I(t+\tau,\omega)$ is measured at a second detector at a time $t_2 = t+\tau$. This variance defines the correlation between the split beams, such that for a coherent state: $\langle I(t,\omega)I(t+\tau,\omega)\rangle = \langle I(t,\omega)\rangle^2$, and the normalized correlation as defined above is $g^{(2)}(t,\tau,\omega) = 1$. However, for a single photon-state radiated by the quantum emitter, $g^{(2)}(t,\tau=0,\omega) = 0$. The latter result follows from the fact that the single-photon amplitude can only exist in either one of the two detectors and not both. Thus a sub-Poissonian photon-statistics, as defined by $g^{(2)}(t,\tau=0,\omega) < 1$, characterizes a nonclassical state of light.

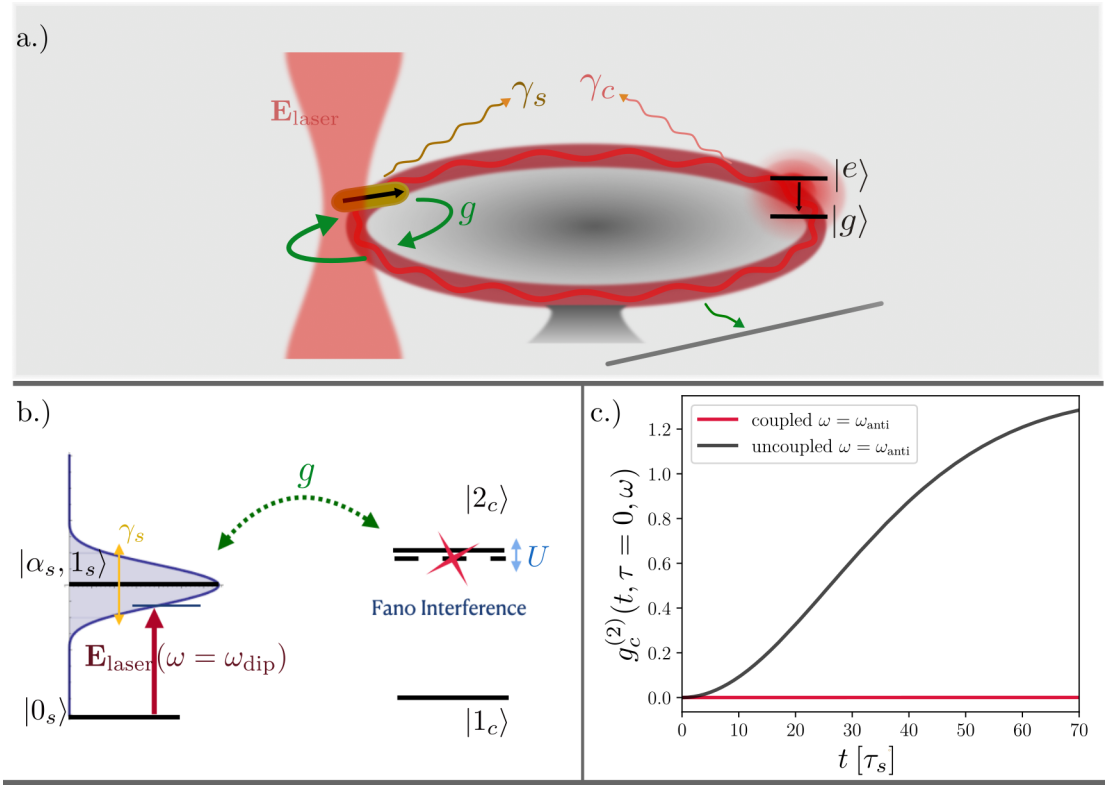

Figure 2.2: Top panel: a.) Scheme of a single-mode cavity, depicted as a microresonator, that is populated with a single-photon state through weak interaction with a two-state quantum system; the cavity's mode is excited through weak interaction with a laser-excited scattering emitter, in the Fano regime $\gamma_s \gg g > \gamma_c$, as described in Fig. 2.1. b.) Scheme of the photon blockade through the Fano interference mechanism of the above system a. Photon blockade occurs in the cavity's high-quality mode when the system is excited at the antiresonant frequency $\omega = \omega_{\text{anti}}$. c.) The second order correlation of the light's field in the cavity $g_c^{(2)}(t, \tau = 0, \omega)$. For the cavity with a single-photon state: $g_c^{(2)}(t, \tau = 0, \omega = \omega_{\text{anti}}) \approx 0$ when the cavity is excited through interaction with the scattering emitter while $g_c^{(2)}(t, \tau = 0, \omega = \omega_{\text{anti}}) > 1$ when the cavity is non-interacting with the scattering emitter and is excited through some other channel (i.e., in the non-Fano regime), black curve. The Fano anti-resonant frequency is $\omega_{\text{anti}} = \tilde{\omega}_c$, which is the dressed resonance frequency of the cavity defined by $\tilde{\omega}_c(N) = \omega_c + UN$; the $\chi^{(3)}$ Kerr-nonlinearity is proportional to $U = \gamma_c \to 0$; $N = 1$, is the average photon-number in the cavity; $|\mathbf{E}_{\text{laser}}| = g$; $g = 4.9 \times 10^{-2}\gamma_s$; $\gamma_c = 10^{-9}\gamma_s$; $\gamma_s = 63.5$ meV; all results produced from QuTip simulation [60], with the Hamiltonian defined in §2.3, Eq. 2.15 or Eq. 2.16.

Here we set out to determine the $g^{(2)}(t, \tau = 0, \omega)$ of the field in a harmonic cavity mode that is initialized with a single-photon state and then excited by a weakly interacting scattering emitter Fig. 2.2. We note that the single-photon state that initially populates the cavity could be achieved by weak coupling to a two-state quantum emitter (described in §2.3). Thus, the initial state of the emitter-cavity system is defined as:

$$|\psi_0\rangle = |0_s\rangle|1_c\rangle|0_{f_{\mathbf{k}}}\rangle \tag{2.2}$$

where $|0_s\rangle$ is the vacuum state of the scattering emitter's mode, $|1_c\rangle$ is the single-photon state in the cavity's mode; and for the first proof of concept we assume an initially evacuated bath, $|0_{f_{\mathbf{k}}}\rangle$, such that the Boltzmann population distribution of the thermal bath is $n_{th} = 0$ (as described see §2.3). We want to explain the result of Fig. 2.2 c that at the Fano antiresonance the deconstructive interference—due to the field of the high-quality cavity's mode that is resonant and out-of-phase with the excitation from the field of the laser-excited scattering emitter—yields $g^{(2)}(t, \tau = 0, \omega = \omega_{\text{anti}}) \rightarrow 0$. Here, $\omega = \omega_{\text{dip}}$ is the antiresonant frequency such that $\omega_{\text{anti}} = \tilde{\omega}_c$; where $\tilde{\omega}_c$ is the dressed resonant frequency of the cavity. This dressed resonant frequency depends on the degree of nonlinearity and the field's amplitude (photon-number) in the cavity, such that $\tilde{\omega}_c(N_c) = \omega_c + UN_c$, where U is proportional to a Kerr-nonlinearity (see section §2.3); and N_c is the average photon-number in the cavity. For our purpose U is negligible.

2.2.1 Deconstructive Fano Interference of the Second-Order Correlation of the Fields in the Cavity-Modes at the Fano Antiresonance

In general, we define the second-order correlation for the photon-amplitudes of the fields from both the modes of the scattering emitter and cavity:

$$g^{(2)}_{s,\,c}(t, \tau = 0, \omega) = \frac{\langle I(t, \omega) I(t + \tau, \omega)\rangle}{\langle I(t, \omega)\rangle^2} = \left| \frac{\Psi^{(2)}_{s,\,c}(t, \omega)}{\left(\Psi^{(1)}_{s,\,c}(t, \omega)\right)^2} \right|^2, \tag{2.3}$$

which depends on the single-photon and two-photon detection amplitudes [61]:

$$\begin{aligned}\Psi^{(1)}_{s,\,c}(t,\omega) &= \Sigma_m \big\langle m_c, 0_s \big| \hat{E}^{+}_{s,\,c}(t,\omega) \big| \psi_0 \big\rangle. \\ \Psi^{(2)}_{s,\,c}(t,\tau=0,\omega) &= \Sigma_m \big\langle m_c, 0_s \big| \hat{E}^{+}_{s,\,c}(t+\tau,\omega) \hat{E}^{+}_{s,\,c}(t,\omega) \big| \psi_0 \big\rangle.\end{aligned} \tag{2.4}$$

These detection-amplitudes are of the positive/negative frequency components of the field, such that: $\hat{E}^{\pm}_{s,\,c}(t,\omega) = \mathcal{E}_{s,\,c} e^{\pm i t \Delta_s} \left[\hat{A}_{s,\,c}(t,\omega) \right]$; with the transformed annihilation operator: $\hat{A}_{s,\,c}(t,\omega) = \hat{\tilde{a}}_{s,\,c} e^{i t \Delta_s}$, described in §2.3, Eqs. 2.22-2.24.

To solve for the two-photon amplitude of the cavity's field, first we solve for the operator associated with the amplitude of the cavity's field, i.e. $\hat{A}_c(t,\omega)$, using the Heisenberg-Langevin equations of motion derived in §2.3, Eq. 2.24. We find that the two-photon amplitude of the cavity's field is

$$\begin{aligned}\Psi^{(2)}_{c}(t,\omega) \approx\; & e^{-it\gamma_s[q - i(g/(\gamma_s/2))^2]} \langle 0_c | \hat{A}^2_c(0) | 1_c \rangle - (\gamma_s/2)^{-1} V e^{it\Delta_s} g \mathcal{F}\left(q(N_c), \delta, t, t'\right) \times \\ & \Big[e^{-it(\gamma_s/2)[q - i(g/(\gamma_s/2))^2]} \left[1 + \mathcal{F}\left(q(N_c), \delta, t, t'\right) \mathcal{F}\left(q(N_c - 1), \delta, t, t'\right) \right] \langle 0_c | \hat{A}_c(0) | 1_c \rangle \\ & + (\gamma_s/2)^{-1} V e^{it\Delta_s} g \mathcal{F}\left(q(N_c), \delta, t, t''\right) \Big].\end{aligned} \tag{2.5}$$

The first term in $\Psi^{(2)}_c(t,\omega)$ is purely due to the amplitude from the single-photon state that initially populates the cavity's mode, and it does not contribute to the two-photon amplitude. It follows that the two-photon amplitude of the field in the cavity is due to the second term, the interference between the amplitudes of the single-photon state and the coherent state from the excitation field of the weakly interacting, laser-excited scattering emitter, where the energy-transfer rate between the laser and the scattering emitter is given by $|\mathbf{E}_{\text{laser}}| = V$, and the energy-transfer rate from the scattering emitter to the cavity is given by g.

The defined integrated phase factor, $\mathcal{F}\left(q(N_c), \delta, t, t'\right)$, describes the evolution of these fields that interfere in the cavity's mode. This interference is due to the phase of the laser-excited emitter's scattered field, $\delta = \Delta_s(\gamma_s/2)^{-1} = (\omega_s - \omega)(\gamma_s/2)^{-1}$, and

the phase of the interacting cavity's field $q(N_c)$ given by

$$\begin{aligned} q(N_c) &= \left[\left(\omega_c + U\langle n_c|\hat{\tilde{a}}_c^{\dagger}(t)\hat{\tilde{a}}_c(t)|n_c\rangle - i\gamma_c/2\right) - \omega_s\right](\gamma_s/2)^{-1} \\ &\approx \left[(\omega_c + UN_c - i\gamma_c/2) - \omega_s\right](\gamma_s/2)^{-1}, \end{aligned} \tag{2.6}$$

with the assumption that the average photon-number in the cavity's mode doesn't vary in time, in the regime $(\gamma_s/2)^{-1} \ll t < (\gamma_c/2)^{-1}$. Also, in the Fano regime, $(\gamma_s/2) \gg g \gg (\gamma_c/2)$, then $q(N_c) \approx [(\omega_c + UN_c) - \omega_s](\gamma_s/2)^{-1} = [\tilde{\omega}_c(N_c) - \omega_s](\gamma_s/2)^{-1}$.

Thus the two-photon amplitude due to the interference of the fields is negligible when $\mathcal{F}(q(N_c), \delta, t, t') \to 0$. Given the expression of the integrated phase factor,

$$\begin{aligned} \mathcal{F}(q(N_c), \delta, t, t') &= \int_0^t \mathrm{d}t' \ \exp\left[-i(t-t')(\gamma_s/2)\big(\delta + q(N_e) - i\left(g/(\gamma_s/2)\right)^2\big)\right] \\ &\approx -\frac{1 - \exp\left[-it(\gamma_s/2)\big(\delta + q(N_c)\big)\right]}{\left[\omega - \underbrace{(\omega_c + UN_c)}_{\tilde{\omega}_c} - ig^2(\gamma_c/2)^{-1}\right]}, \end{aligned} \tag{2.7}$$

we find that the two-photon amplitude from the interfering fields in the cavity's mode vanishes for two cases: when the system is resonant, i.e. $\omega = \omega_s = \omega_c$, and with a high degree of nonlinearity, $U = 20\gamma$; this is the conventional single-photon blockade. However, the main result of this study, as shown in Fig. 2.2 c is that this single-photon blockade can be achieved even for a negligible degree of nonlinearity $U \approx \gamma_c \to 0$, in the Fano regime, when the cavity is excited through a broadband scattering emitter, at the Fano antiresonance, i.e., $\omega = \omega_{\mathrm{anti}}$. At this antiresonance there is an out-of-phase, deconstructive interference, $\delta = -q$, between the laser-excited cavity's mode and the interacting cavity's mode.

Since the field of the scattering emitter is due to the pumping of coherent laser, and as well as due to the interaction with the field of single-photon state of the cavity, we find that the state of light from the scattering emitter's field is akin to the so called single-photon-added coherent state [62]. Here the degree of nonclassical light, $g_s^{(2)}(t, \tau = 0, \omega = \omega_{\mathrm{anti}}) < 1$, becomes more evident for smaller initial amplitudes of

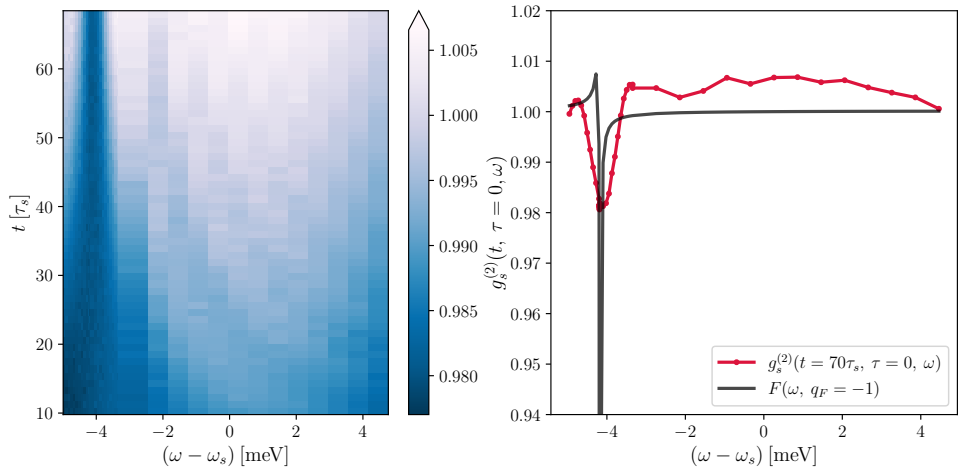

Figure 2.3: Left panel: The photon-statistics of the field in the laser-excited scattering emitter that is weakly interacting with the single-photon state of the cavity. The second-order correlation attains a minimum value at the Fano antiresonance: $\omega_{\text{anti}} = \tilde{\omega}_c$; $g^{(2)}(t >> \tau_s, \tau = 0, \omega = \tilde{\omega}_c) < 1$. Right panel: The Fano profile, black curve, and a line segment of the second-order correlation function, red curve, at the cavity's steady state $t \gg \tau_s = (\gamma_s/2)^{-1}$; the correlation function attains its minimum value at the Fano antiresonance $\epsilon(\tilde{\omega}_c) = q_F$. Here $\omega_c - \omega_s = (1/16)\gamma_s$; $|\mathbf{E}_{\text{laser}}| = 0.69g$; all other parameters as above in Fig. 2.2.

the laser's coherent state, $|\alpha|^2 \approx V^2(\gamma_s/2)^{-2} \ll 1$. Thus given that the field of the laser-excited scattering emitter is

$$\hat{E}_s^+(t,\omega) = i\mathcal{E}_s e^{-i\Delta_s t}\left[(\gamma_s/2)^{-1}Ve^{it\Delta_s} + (\gamma_s/2)^{-1}g\hat{A}_c(t)\right], \tag{2.8}$$

where the amplitude of the scattering emitter's field is due the coupled laser's coherent amplitude $(\gamma_s/2)^{-1}V$ and that of the interacting cavity's single-photon amplitude $(\gamma_s/2)^{-1}g\hat{A}_e$. From this follows that the two-photon amplitude from the field of the

scattering emitter is

$$\Psi_s^{(2)}(t,\omega) \approx (\gamma_s/2)^{-2}\big\langle 0_s\big|V^2 e^{i2\Delta_s t} - 2gVe^{i\Delta_s t}\Big[e^{-i(\gamma_s/2)t[q-i(g/(\gamma_s/2))^2]}\times \\ \Big(1-\frac{1}{2}(\gamma_s/2)^{-1}g^2[\mathcal{F}\left(q(N_c),\delta,t,t'\right)+\mathcal{F}\left(q(N_c-1),\delta,t,t'\right)]\Big)\langle 0_c|\hat{A}_c|1_c\rangle \\ +(\gamma_s/2)^{-1}Ve^{i\Delta_s t}g\mathcal{F}\left(q(N_c),\delta,t,t'\right)\Big(1-\frac{1}{2}(\gamma_s/2)^{-1}g^2\mathcal{F}\left(q(N_c),\delta,t,t''\right)\Big)\Big]\big|0_s\big\rangle. \tag{2.9}$$

As Figure 2.3 shows, for a weak laser-excitation amplitude $(\gamma_c/2)^{-1}V \ll 1$, with a weak nonlinearity $U \approx \gamma$, and at the antiresonance where $\mathcal{F}\left(q(N_c),\delta,t,t'\right) \to 0$, then $g_s^{(2)}(t,\tau=0,\omega=\omega_{\text{anti}}) < 1$ but $g_s^{(2)}(t,\tau=0,\omega_{\text{anti}}) > 0.5$. This is the case, as observed in ref. [56], for the field of the pumped broadband mode (which in our study is that of the scattering emitter). Therefore, total deconstructing interference occurs in the narrow mode, here represented as the high-quality microresonator cavity, whose field yields $g_c^{(2)}(t,\tau=0,\omega_{\text{anti}}) \to 0$.

The Fano Antiresonance and the Fano Profile

In Fig. 2.4 (top left panel) the spectral distribution of the scattering emitter's field shows the characteristic Fano profile that arises from the weakly interacting scattering emitter and high-quality cavity modes with contrasting losses: i.e., the scattering emitter's broadband mode weakly interacting with the cavity's high-quality mode. We see that, first, defining the spectral distribution of the scattering emitter-cavity spectral distribution [63]:

$$\begin{aligned}\mathcal{S}(\omega) &= \lim_{t\to\infty} 1/\pi \mathbf{Re}\int \mathrm{d}\tau \langle \hat{A}_s^\dagger(t,\omega)\hat{A}_s(t+\tau,\omega)\rangle e^{-i\tau\Delta_s}\delta(\tau) \\ &= \frac{1}{\pi}\left|\frac{V}{\Delta_s - i\gamma_s/2}\right|^2\left|\frac{q_F+\epsilon}{\epsilon+i}\right|^2\end{aligned} \tag{2.10}$$

yields the prefactor that is the spectral distribution of the non-interacting (uncoupled) scattering emitter's spectrum, i.e., $\mathcal{S}(\omega)_{g=0} = \lim_{t\to\infty} 1/\pi|V/(\Delta_s - i\gamma_s/2)|^2$, see black curve in the top left panel of Fig. 2.4. The reduced spectral distribution defined as

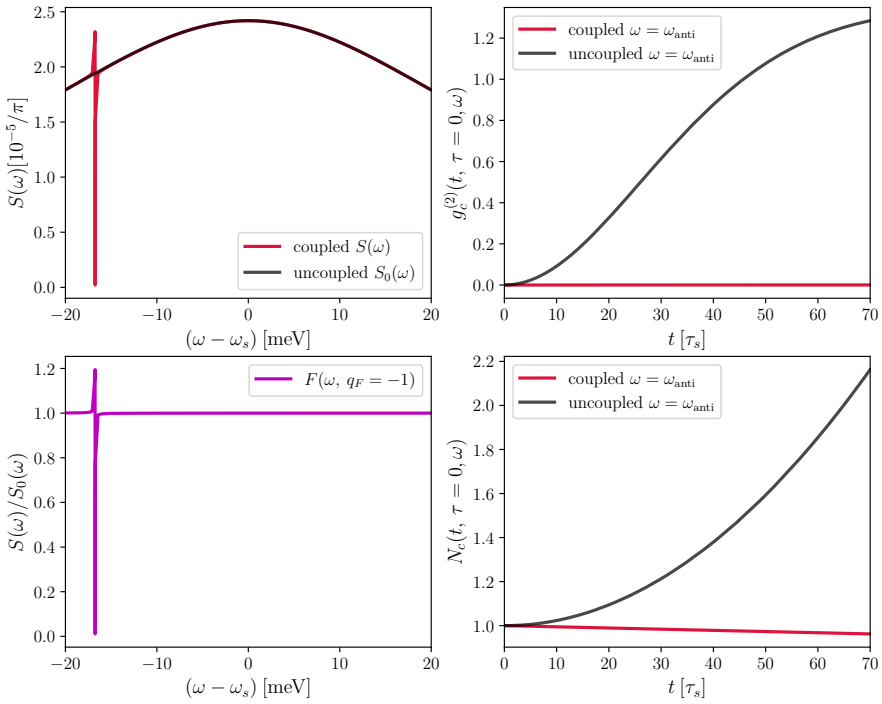

Figure 2.4: Top left: spectra profiles of the laser-excited scattering emitter weakly interacting with the cavity, red curve $S(\omega)$, and that of the isolated laser-excited scattering emitter, black curve, $S_0(\omega)$, where $g = 0$. For the interacting emitter, an asymmetric spectral profile—due to Fano interference—arises about the resonance frequency of the cavity's high-quality mode $\tilde{\omega}_c$. Bottom left: the reduced spectra that reveals the Fano profile $F(\epsilon(\omega), q_F) = S(\omega)/S_0(\omega)$. The minimum of the asymmetric spectral profile occurs at the antiresonant frequency $\omega_{\text{anti}} = \tilde{\omega}_c$ where there is deconstructing interference between the scattering emitter and the high-quality cavity. Top right: The second-order correlation of the cavity's mode in a single-photon state. Photon blockade occurs at the Fano antiresonance, $g_c^{(2)}(t, \tau = 0, \omega = \omega_{\text{anti}}) \approx 0$, as described in Fig 2.2c c.) Bottom left: the average photon number in the cavity's mode, corresponding to the calculations in the top right panel. Note that photon blockade at the antiresonance occurs for times $\tau_s \ll t < \tau_c$, where $\tau_{s,\,c} = (\gamma_{s,\,c}/2)^{-1}$ are the coherence times of the scattering emitter and cavity modes.

$\mathcal{S}(\omega)/\mathcal{S}(\omega)_{g=0}$ is the characteristic asymmetric Fano profile $\mathcal{F}(\epsilon, q_F) = |(q_F + \epsilon)/(\epsilon + i)|^2$ of the Fano interference [22, 50], as shown in the bottom left panel of Fig. 2.4. The

deconstructing interference occurs when $\epsilon = (\omega - \Omega_c)/(\Gamma/2)$ is equal and opposite to $q_F = (\Omega_c - \tilde{\omega}_c)/(\Gamma/2)$, with Γ being the line-width of the Fano profile; this occurs at the aforementioned antiresonance $\omega = \omega_{\text{anti}} = \tilde{\omega}_c$, where $\epsilon(\omega_{\text{anti}}) = -q_F$; and at the Fano antiresonance photon is blocked from transmitting through the scattering emitter and into the cavity with a single-photon state, such that $g_c^{(2)}(\tau = 0, \omega = \omega_{\text{anti}}) \to 0$.

2.2.2 Comparison Between the Photon-Blockade through Fano Antiresonance and the Unconventional Photon Blockade through Quantum Interference.

Ultimately, the photon antibunching through the mechanism of Fano interference can still be understood as a quantum interference of the transition probabilites in the excitation pathways, where the nonclassical effect of photon antibunching is pronounced for the so called cooperativity: $g^2/\gamma_s\gamma_c \gg 1$ [47, 46, 55]. Note that this cooperativity is satisfied for both conventional and unconventional photon blockade, and for the proposed scheme through Fano interference in the weak interaction regime. Also, as observed in ref. [47] the amplitude of the cavity's field is formed by the (out-of-phase) interference of the radiated dipole's field and the empty cavity excitation: we also note that such out-of-phase deconstructive interference is the principle behind the Fano interference at the antiresonance.

We also observe that this blockade effect through Fano interference is akin to the non-Hermitian photon-blockade [55], where photon antibunching has been shown to occur only when the laser's frequency is resonant with the cavity's mode. We note that this non-Hermitian photon-blockade corresponds to the photon blockade from the Fano interference mechanism when the weakly interacting emitter-cavity system is resonant, i.e., $q \approx q_F = 0$, as shown in the middle panel of Fig. 2.5. However, this study generalizes this condition for weakly interacting emitter-cavity modes that are non-resonant, $q_F > 1$ left panel Fig. 2.5 or $q_F < 1$ right panel Fig. 2.5, with the result that the photon antibunching occurs when the laser's frequency is at the anti-resonant frequency, which is approximately the frequency of the low-loss mode,

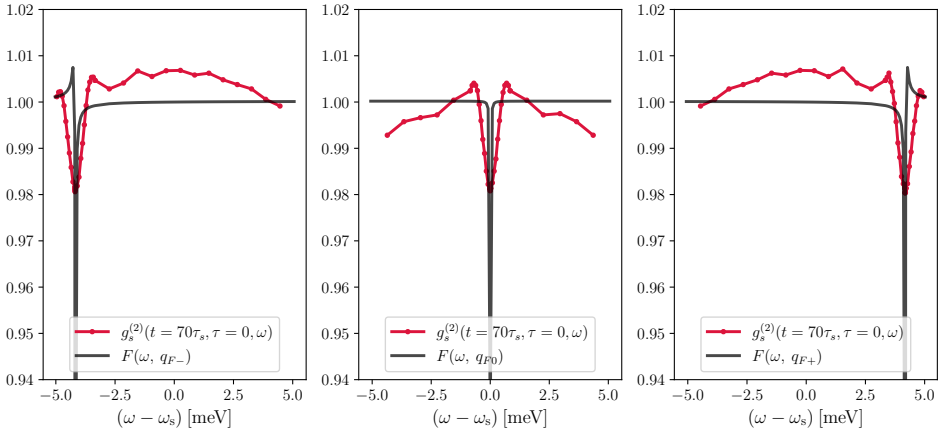

Figure 2.5: Photon-statistics of the laser-excited scattering emitter's field that is interacting with the field of the single-photon state from the high-quality cavity, as function of the Fano asymmetric parameter, black curves: left, $q_F < 1$; middle, $q_F = 0$; right, $q_F > 1$. In each case, the second-order correlation function, red curve, is calculated at the scattering emitter's steady state: $t \gg \tau_s = (\gamma_s/2)^{-1}$; the correlation function attains its minimum value at the Fano antiresonance $\epsilon(\tilde{\omega}_c) = -q_F$.

i.e. $\epsilon(\omega = \tilde{\omega}_c) = -q_F$.

2.3 Theoretical Description of the Weakly Driven, Weakly Interacting Emitter-Cavity System for Photon Blockade

The Analogous Jaynes-Cummings Hamiltonian

It is known that a two-state quantum emitter that is interacting with a single-mode cavity is described by the Jaynes-Cummings Hamiltonian §1.0.1:

$$\hat{\mathcal{H}}_{\text{JC}} = \frac{\hbar\omega_e}{2}\hat{\sigma}_z + \hbar\omega_k \hat{a}_k^\dagger \hat{a}_k + \hbar g(\hat{a}_k^\dagger \hat{\sigma}_- + \hat{a}_k \hat{\sigma}_+) \tag{2.11}$$

where $\hat{\sigma}_-$, $\hat{\sigma}_+$, and $\hat{\sigma}_z$, are the Pauli operator amplitudes describing the relaxation and excitation of the dipolar mode of the two-state quantum system; while $\hat{a}_k$, and $\hat{a}_k^\dagger$ are the operator amplitudes describing the annihilation or creation of photon in the cavity's single-mode labeled k; and $\hbar g$ is the interaction energy between the fields

of the dipolar mode of the emitter and the single-mode of the cavity. The nonlinear spectral distribution of the field of the two-state quantum system can be mapped onto an analogous nonlinear system of a Kerr resonator [45] or that of a transmon [64], such that, $\hat{\sigma}_- \rightarrow \hat{a}_c$ and $\hat{\sigma}_+ \rightarrow \hat{a}_c^\dagger$, $\omega_e \rightarrow \omega_c$:

$$\hat{\mathcal{H}}_{\mathrm{JC-analog}} = \hbar\omega_c \hat{a}_c^\dagger \hat{a}_c + \hbar\frac{U}{2}\hat{a}_c^\dagger \hat{a}_c^\dagger \hat{a}_c \hat{a}_c + \hbar\omega_k \hat{a}_k^\dagger \hat{a}_k + \hbar g(\hat{a}_k^\dagger \hat{a}_c + \hat{a}_k \hat{a}_c^\dagger) \tag{2.12}$$

with the degree of Kerr nonlinearity given by U. This analogous Hamiltonian to that of a two-state quantum system is valid when the degree of nonlinearity is much greater than the inhomogeneous broadening, γ_c, such that $U \approx 20\gamma_c$ [45].

However, in this study, photon blockade is considered in such a single-mode Kerr cavity with negligible nonlinearity, i.e. $U \approx \gamma_c \rightarrow 0$, and this weak nonlinear Kerr cavity, or rather harmonic high-quality cavity is populated with a single-photon via weak interaction with the field of a two-state quantum system. We find that photon blockade can be achieved in this harmonic cavity that is weakly interacting with a two-state quantum system when the cavity is excited via weak coupling to a scattering emitter's field, given by the operator amplitude $\hat{a}_k \equiv \hat{a}_{\omega_s/c} \equiv \hat{a}_s$. The conditions being that the scattering emitter's field must have a spectral line-width broadening γ_s that is much larger than that of the cavity γ_c, i.e. in the Fano regime $\gamma_s \gg g > \gamma_c$; and that the excitation must occur at the Fano antiresonant frequency where deconstructing interference prevents transfer of energy from the scattering emitter into the cavity's mode occupied with a single-photon. The Hamiltonian for such a system is defined as

$$\hat{\mathcal{H}}_{\mathrm{emitter-cavity}} = \hbar\omega_c \hat{a}_c^\dagger \hat{a}_c + \hbar\frac{U}{2}\hat{a}_c^\dagger \hat{a}_c^\dagger \hat{a}_c \hat{a}_c + \hbar\omega_s \hat{a}_s^\dagger \hat{a}_s + \hbar g(\hat{a}_s^\dagger \hat{a}_c + \hat{a}_s \hat{a}_c^\dagger) + \hbar g_2(\hat{a}_c^\dagger \hat{\sigma}_- + \hat{a}_c \hat{\sigma}_+), \tag{2.13}$$

where $\hat{a}_s$, $\hat{a}_s^\dagger$ are the annihilation, creation operator amplitudes associated with the field of the scattering emitter.

The emitter-cavity system is pumped by a coherent continuous wave of a laser, whose monochromatic field is given by $\mathbf{E}_{laser}(t) = \frac{\mathcal{E}_l}{2}\hat{\mathbf{e}}_l(e^{-i\omega t} + e^{i\omega t})$, with amplitude

$\mathcal{E}_l$, and the unit vector of polarization $\hat{\mathbf{e}}_l$. Since the laser pumps the emitter-cavity system through the mode of the scattering emitter, this part of the Hamiltonian is described by

$$\hat{\mathcal{H}}_{\text{pump}} = \hbar V(e^{-i\omega t} + e^{i\omega t})(\hat{a}_s - \hat{a}_s^\dagger) \tag{2.14}$$

where $\hbar V = \mathbf{E}_{laser} \cdot \mathbf{d}_s \equiv J_l(t)\hat{\mathbf{e}}_l \cdot \hat{A}_s(t)\hat{\mathbf{e}}_s$ is the interaction energy between the laser's field and scattering emitter's induced dipole moment $\mathbf{d}_s$; and $\mathbf{J}_d(t)$ is the current density of the laser's field and $\hat{\mathbf{A}}_s(t)$ is the vector potential of the field of the scattering emitter's induced dipolar mode.

Thus the Hamiltonian describing the weakly pumped emitter-cavity system is given by

$$\hat{\mathcal{H}}_{\text{system}} = \hat{\mathcal{H}}_{\text{emitter-cavity}} + \hat{\mathcal{H}}_{\text{pump}}. \tag{2.15}$$

and the the system's initial state is $|\psi_0\rangle = |0_s\rangle|0_c\rangle|e\rangle$. Numerical calculations of the Lindbladian show that the above Hamiltonian $\hat{\mathcal{H}}_{\text{system}}$ yields results in Fig. 2.2 c that are equivalent to the following Hamiltonian

$$\hat{\mathcal{H}}^{(1)}_{\text{system}} = \hat{\mathcal{H}}^{(1)}_{\text{emitter-cavity}} + \hat{\mathcal{H}}_{\text{pump}}, \tag{2.16}$$

$$\hat{\mathcal{H}}^{(1)}_{\text{emitter-cavity}} = \hbar\omega_c \hat{a}_c^\dagger \hat{a}_c + \hbar\frac{U}{2}\hat{a}_c^\dagger \hat{a}_c^\dagger \hat{a}_c \hat{a}_c + \hbar\omega_s \hat{a}_s^\dagger \hat{a}_s + \hbar g(\hat{a}_s^\dagger \hat{a}_c + \hat{a}_s \hat{a}_c^\dagger), \tag{2.17}$$

with the following initial state: $|\psi_0\rangle = |0_s\rangle|1_c\rangle$. In other words, the effect of coupling to the excited state of the two-state quantum system is to populate the cavity mode with a single-photon state. This is the starting point of the analytic discussion presented in §2.2.

For the analytic discussion presented in §2.2, we use the Heisenberg-Langevin formalism to describe the interaction of the modes with the environment, which introduces the rates of energy dissipation to the environment, γ_s and γ_c, that broadens the line-width of the spectral distributions of the bosonic modes of the scattering emitter and high-quality cavity. This part of the Hamiltonian is

$$\hat{\mathcal{H}}_{\text{dissipation}} = \Sigma_{\mathbf{k}} \hbar\omega_{\mathbf{k}} \hat{f}_{\mathbf{k}}^\dagger \hat{f}_{\mathbf{k}} + \Sigma_{\mathbf{k}} \left[\hbar V_{\mathbf{k}}^s \hat{f}_{\mathbf{k}}^\dagger \hat{a}_s + \hbar V_{\mathbf{k}}^c \hat{f}_{\mathbf{k}}^\dagger \hat{a}_c + \text{h.c.}\right]. \tag{2.18}$$

This formalism describes the environment as a continuum of bosonic modes associated with the annihilation and creation operators $\hat{f}_{\mathbf{k}}, \hat{f}^{\dagger}_{\mathbf{k}}$, and the modes of the scattering emitter and cavity dissipate energy to this environment through the weak interaction energy $\hbar V^{c}_{\mathbf{k}}$ and $\hbar V^{s}_{\mathbf{k}}$.

Thus the Hamiltonian describing the weakly pumped emitter-cavity system is given by

$$\hat{\mathcal{H}} \equiv \hat{\mathcal{H}}_{\text{system}-\text{environment}} = \hat{\mathcal{H}}^{(1)}_{\text{system}} + \hat{\mathcal{H}}_{\text{dissipation}}. \tag{2.19}$$

This Hamiltonian is time-dependent due to the coherent oscillation of the laser's amplitude. We simplify the Hamiltonian by performing a unitary transformation, with the operator $U = e^{S}$ and $S = -i\omega t(\hat{a}^{\dagger}_{s}\hat{a}_{s} + \hat{a}^{\dagger}_{c}\hat{a}_{c} + \hat{f}^{\dagger}_{\mathbf{k}}\hat{f}_{\mathbf{k}})$, that rotates the Hamiltonian into a frame now oscillating with the laser's resonant frequency. This unitary transformation is defined by [65]

$$T : \hat{\mathcal{H}} \equiv \hat{\tilde{\mathcal{H}}} = U^{\dagger}\hat{\mathcal{H}}U + i\hbar\dot{U}^{\dagger}U, \tag{2.20}$$

and if the period $T = 2\pi/\omega$ is very small with respect to a reference time, i.e. the experimental observation, then the effective Hamiltonian that averages over a period would suffice for any further analysis. This approximation is akin to the rotating wave approximation, which yields the time-independent Hamiltonian:

$$\begin{aligned}
\hat{\mathcal{H}}_{\text{eff}} &= \int_{0}^{T} dt \hat{\tilde{\mathcal{H}}}(t) \\
&= \hbar\Delta_{c}\hat{\tilde{a}}^{\dagger}_{c}\hat{\tilde{a}}_{c} + \hbar\frac{U}{2}\hat{\tilde{a}}^{\dagger}_{c}\hat{\tilde{a}}^{\dagger}_{c}\hat{\tilde{a}}_{c}\hat{\tilde{a}}_{c} + \hbar\Delta_{s}\hat{\tilde{a}}^{\dagger}_{s}\hat{\tilde{a}}_{s} + \hbar g(\hat{\tilde{a}}^{\dagger}_{s}\hat{\tilde{a}}_{c} + \hat{\tilde{a}}_{s}\hat{\tilde{a}}^{\dagger}_{c}) \\
&+ \Sigma_{\mathbf{k}}\hbar\omega_{\mathbf{k}}\hat{\tilde{f}}^{\dagger}_{\mathbf{k}}\hat{\tilde{f}}_{\mathbf{k}} + \Sigma_{\mathbf{k}}\left[\hbar V^{s}_{\mathbf{k}}\hat{\tilde{f}}^{\dagger}_{\mathbf{k}}\hat{\tilde{a}}_{s} + \hbar V^{c}_{\mathbf{k}}\hat{\tilde{f}}^{\dagger}_{\mathbf{k}}\hat{\tilde{a}}_{c} + \text{h.c.}\right] \\
&+ \hbar V(\hat{\tilde{a}}_{s} - \hat{\tilde{a}}^{\dagger}_{s}),
\end{aligned} \tag{2.21}$$

with $\hat{\tilde{a}}_{s} = \hat{a}_{s}e^{-i\omega t}$. In the frame rotating with the pump-laser's frequency the energies of the modes are now with respect to the detuning between the modes' natural resonant energies and the drive's: e.g., $\hbar\omega_{s}\hat{a}^{\dagger}_{s}\hat{a}_{s} \rightarrow \hbar\Delta_{s}\hat{\tilde{a}}^{\dagger}_{s}\hat{\tilde{a}}_{s}$, with the scattering emitter's modal detuning defined as $\Delta_{s} = \omega_{s} - \omega$.

The Heisenberg Equation of Motion and the Heisenberg-Langevin Formalism

The Heisenberg-Langevin approach is particularly suitable for the calculations of two-time correlation functions of the system's operators [63]. For instance, the spectral distribution function of the single-mode cavity is given by $S(\omega) = 1/\pi \mathbf{Re} \int_0^\infty \mathrm{d}\tau \langle \hat{a}_c^\dagger(t)\hat{a}_c(t+\tau)\rangle e^{-i\omega\tau}$ and the second-order correlation function of two-photon absorption by the single-mode cavity is given by $G^{(2)}(t, t+\tau) = \langle \hat{a}_c^\dagger(t)\hat{a}_c^\dagger(t+\tau)\hat{a}_c(t+\tau)\hat{a}_c(t)\rangle$. First, the Heisenberg equation of motion for the system's operators is

$$\begin{aligned}
\dot{\hat{\tilde{a}}}_c &= \frac{i}{\hbar}[\hat{\mathcal{H}}_{\text{eff}}, \hat{\tilde{a}}_c] \\
&= -i\Delta_c \hat{\tilde{a}}_c - iU\hat{\tilde{a}}_c^\dagger \hat{\tilde{a}}_c \hat{\tilde{a}}_c - ig\hat{\tilde{a}}_s - i\Sigma_{\mathbf{k}} V_{\mathbf{k}}^{c*} \hat{\tilde{f}}_{\mathbf{k}} \\
\dot{\hat{\tilde{a}}}_s &= -i\Delta_s \hat{\tilde{a}}_s - ig\hat{\tilde{a}}_s - i\Sigma_{\mathbf{k}} V_{\mathbf{k}}^{s*} \hat{\tilde{f}}_{\mathbf{k}} + iV \\
\dot{\hat{\tilde{f}}}_{\mathbf{k}} &= -i\omega_{\mathbf{k}} \hat{\tilde{f}}_{\mathbf{k}} - iV_{\mathbf{k}}^s \hat{\tilde{a}}_s - iV_{\mathbf{k}}^c \hat{\tilde{a}}_c.
\end{aligned} \tag{2.22}$$

To solve the system's dynamics we employ the Heisenberg-Langevin approach. The dynamics of the reservoir operators $\hat{f}_{\mathbf{k}}(t)$ can be formally integrated and with its solution we can express the system's dynamics in terms of only the degrees of freedom of the emitter-cavity operators $\hat{\tilde{a}}_s(t), \hat{\tilde{a}}_c(t)$. Then converting to the slowly varying operators $\hat{A}_s(t) = \hat{\tilde{a}}_s(t)e^{i\Delta_s t}$ and $\hat{A}_c(t) = \hat{\tilde{a}}_c(t)e^{i\Delta_s t}$ yields the modified equations of

motion:

$$\begin{aligned}
\dot{\hat{A}}_s(t) &= -ig\hat{A}_c(t) + iVe^{i\Delta_s t} \\
&\quad - \Sigma_{\mathbf{k}}[iV_{\mathbf{k}}^{s*}\hat{\tilde{f}}_{\mathbf{k}}(0)e^{-i(\omega_{\mathbf{k}}-\omega_s)t} \\
&\quad + |V_{\mathbf{k}}^{s}|^2 \int \mathrm{d}t' \hat{A}_s(t')e^{-i(\omega_{\mathbf{k}}-\omega_s)(t-t')} \\
&\quad + V_{\mathbf{k}}^{s*}V_{\mathbf{k}}^{c} \int \mathrm{d}t' \hat{A}_c(t')e^{-i\Delta_{\mathbf{k}}(t-t')-i\Delta_c t'+\Delta_s t}] \\
\dot{\hat{A}}_c(t) &= -i\left[(\omega_c-\omega_s) + U\hat{\tilde{a}}_c^{\dagger}\hat{\tilde{a}}_c\right]\hat{A}_c(t) - ig\hat{A}_s(t) \\
&\quad - \Sigma_{\mathbf{k}}[iV_{\mathbf{k}}^{c*}\hat{\tilde{f}}_{\mathbf{k}}(0)e^{-i(\omega_{\mathbf{k}}-\omega_c)t} \\
&\quad + |V_{\mathbf{k}}^{c}|^2 \int \mathrm{d}t' \hat{A}_c(t')e^{-i(\omega_{\mathbf{k}}-\omega_c)(t-t')} \\
&\quad + V_{\mathbf{k}}^{c*}V_{\mathbf{k}}^{s} \int \mathrm{d}t' \hat{A}_s(t')e^{-i\Delta_{\mathbf{k}}(t-t')-i\Delta_s t'+\Delta_c t}].
\end{aligned} \tag{2.23}$$

The final terms in both equations of motion correspond to multiple scattering events that are negligible since the modes do not interact through the reservoir [66]; this approximation is also valid with a discrete mode that barely interact with the reservoir. The remaining integral-terms can be handled using Weisskopf-Wigner approximation [63] so that

$$\begin{aligned}
\dot{\hat{A}}_c(t) &= -\frac{\gamma_c}{2}\hat{A}_c(t) - i\left[(\omega_c-\omega_s) + (U/2)\hat{\tilde{a}}_c^{\dagger}\hat{\tilde{a}}_c\right]\hat{A}_c(t) - ig\hat{A}_s(t) + \hat{F}_c(t) \\
\dot{\hat{A}}_s(t) &= -\frac{\gamma_s}{2}\hat{A}_s(t) - ig\hat{A}_c(t) + iVe^{i\Delta_s t} + \hat{F}_s(t)
\end{aligned} \tag{2.24}$$

with the dissipative terms defined as [63, 66]

$$\begin{aligned}
\gamma_c &= 2\pi|V_{\omega_c/c}^{c}|^2\mathcal{D}(\omega_c) \\
\gamma_s &= 2\pi|V_{\omega_s/c}^{s}|^2\mathcal{D}(\omega_s) \\
&= 4\omega_s^3|\mathbf{d}_s|^2/3\hbar c^3.
\end{aligned} \tag{2.25}$$

The free space density of state is $\mathcal{D}(\omega) = V\omega^2/\pi^2c^3$ [63], and $\mathbf{d}_s$ is the dipole moment of the scattering emitter [66], and the continuum modes from the environment are

associated with the so called noise operators

$$\begin{aligned}\hat{F}_c(t) &= -i\Sigma_{\mathbf{k}} V_{\mathbf{k}}^{c*} \hat{\tilde{f}}_{\mathbf{k}}(0) e^{-i(\omega_{\mathbf{k}}-\omega_c)t} \\ \hat{F}_s(t) &= -i\Sigma_{\mathbf{k}} V_{\mathbf{k}}^{s*} \hat{\tilde{f}}_{\mathbf{k}}(0) e^{-i(\omega_{\mathbf{k}}-\omega_s)t}.\end{aligned} \tag{2.26}$$

These noise operators are crucial in preserving the canonical commutation relation between the creation and annihilation operators. For instance, given the solution for the cavity's dynamics

$$\begin{aligned}\hat{A}_c(t) = \hat{A}_c(0) e^{-\frac{\gamma_c}{2}t} \\ - i \int \mathrm{d}t' \left[g\hat{A}_s(t') e^{-i(\omega_s-\omega_c)t'} + \hat{F}_c(t') \right] e^{-\frac{\gamma_c}{2}(t-t')},\end{aligned} \tag{2.27}$$

then for the dissipative mode of a cavity that is non-interacting with the scattering emitter, one finds that

$$\begin{aligned}[\hat{A}_c(t), \hat{A}_c^\dagger(t)] = e^{-\gamma_c t} \\ + ie^{-\gamma_c t} \int \mathrm{d}t' e^{-\frac{\gamma_c}{2}t'} \left[\hat{A}_c(0)\hat{F}_c^\dagger(t') - \hat{F}_c(t')\hat{A}_c^\dagger(0) \right] \\ + \int \mathrm{d}t' \int \mathrm{d}t'' e^{-\frac{\gamma_c}{2}(t-t')} e^{-\frac{\gamma_c}{2}(t-t'')} \hat{F}_c(t')\hat{F}_c^\dagger(t'')\end{aligned} \tag{2.28}$$

Note that $\hat{A}_c(0)$ and $\hat{F}_c(t')$ are statistically independent so that

$$[\hat{A}_c(t), \hat{A}_c^\dagger(t)] = e^{-\gamma_c t} + \int \mathrm{d}t' \int \mathrm{d}t'' e^{-\frac{\gamma_c}{2}(t-t')} e^{-\frac{\gamma_c}{2}(t-t'')} \hat{F}_c(t')\hat{F}_c^\dagger(t''). \tag{2.29}$$

The above equation shows that the noise operators with the appropriate properties preserve the commutation relation at all times. This is the so called fluctuation-dissipation theorem, i.e., dissipation is always accompanied by fluctuations of systems. Assuming the reservoir is in thermal equilibrium, it can be shown that $\left\langle \hat{F}_c(t')\hat{F}_c^\dagger(t'') \right\rangle = \gamma_c(n_{\mathrm{th}}+1)\delta(t'-t'')$, with the average thermal boson number $n_{\mathrm{th}} = (\exp(\hbar\omega_c/k_B T))^{-1}$[63]. For proof of concept, let us assume an initially evacuated reservoir state so that $n_{\mathrm{th}} = 0$; then it follows that $\left\langle [\hat{A}_c(t), \hat{A}_c^\dagger(t)] \right\rangle = 1$.

BIBLIOGRAPHY

[1] John David Jackson. *Classical electrodynamics*. John Wiley & Sons, 2012.

[2] Michael A Nielsen and Isaac L Chuang. *Quantum computation and quantum information*. Cambridge university press, Cambridge, 2001.

[3] A Femius Koenderink, Andrea Alù, and Albert Polman. Nanophotonics: Shrinking light-based technology. *Science*, 348(6234):516–521, 2015.

[4] Päivi Törmä and William L Barnes. Strong coupling between surface plasmon polaritons and emitters: a review. *Reports on Progress in Physics*, 78(1):013901, 2014.

[5] Darrick E Chang, Anders Søndberg Sørensen, PR Hemmer, and MD Lukin. Strong coupling of single emitters to surface plasmons. *Physical Review B*, 76(3):035420, 2007.

[6] E. M. Purcell. Spontaneous emission probabilities at radio frequencies. *Phys. Rev.*, 69:674, Jun 1946.

[7] Serge Haroche and J-M Raimond. *Exploring the quantum: atoms, cavities, and photons*. Oxford university press, 2006.

[8] Marc R. Bourgeois, Feng Pan, C Praise Anyanwu, Austin G. Nixon, Beutler Elliot K., Jennifer A. Dionne, Randall H. Goldsmith, and David J. Masiello. Spectroscopy in nanoscopic cavities: Models and recent experiments. *Annual review of physical chemistry*, 75, 2024.

[9] Kevin M Birnbaum, Andreea Boca, Russell Miller, Allen D Boozer, Tracy E Northup, and H Jeff Kimble. Photon blockade in an optical cavity with one trapped atom. *Nature*, 436(7047):87–90, 2005.

[10] Darrick E Chang, Vladan Vuletić, and Mikhail D Lukin. Quantum nonlinear optics—photon by photon. *Nature Photonics*, 8(9):685–694, 2014.

[11] Matthew D Eisaman, Jingyun Fan, Alan Migdall, and Sergey V Polyakov. Invited review article: Single-photon sources and detectors. *Review of scientific instruments*, 82(7):071101, 2011.

[12] Andrew J Shields. Semiconductor quantum light sources. *Nature photonics*, 1(4):215–223, 2007.

[13] Stefan Strauf, Nick G Stoltz, Matthew T Rakher, Larry A Coldren, Pierre M Petroff, and Dirk Bouwmeester. High-frequency single-photon source with polarization control. *Nature photonics*, 1(12):704–708, 2007.

[14] Markus Hennrich, Thomas Legero, Axel Kuhn, and Gerhard Rempe. Photon statistics of a non-stationary periodically driven single-photon source. *New Journal of Physics*, 6(1):86, 2004.

[15] Tatjana Wilk, Simon C Webster, Axel Kuhn, and Gerhard Rempe. Single-atom single-photon quantum interface. *Science*, 317(5837):488–490, 2007.

[16] Nicolas Gisin, Grégoire Ribordy, Wolfgang Tittel, and Hugo Zbinden. Quantum cryptography. *Reviews of modern physics*, 74(1):145, 2002.

[17] Charles H Bennett and Gilles Brassard. A quantum information science and technology roadmap. *Part*, 2:12, 2004.

[18] Charles H Bennett. Quantum cryptography using any two nonorthogonal states. *Physical review letters*, 68(21):3121, 1992.

[19] Kevin C Smith. *Theoretical Models of Hybrid Light-Matter Systems and Their Applications*. University of Washington, 2021.

[20] E. Lassettre, M. Krasnow, and S. Silverman. Inelastic scattering of electrons by helium. *J. Chem. Phys.*, 40:1242–1248, Dec 1964.

[21] U. Fano. Effects of configuration interaction on intensities and phase shifts. *Phys. Rev.*, 124:1866–1878, Dec 1961.

[22] Niket Thakkar, Morgan T Rea, Kevin C Smith, Kevin D Heylman, Steven C Quillin, Kassandra A Knapper, Erik H Horak, David J Masiello, and Randall H Goldsmith. Sculpting Fano resonances to control photonic–plasmonic hybridization. *Nano Lett.*, 17(11):6927–6934, 2017.

[23] Feng Pan, Kevin C Smith, Hoang L Nguyen, Kassandra A Knapper, David J Masiello, and Randall H Goldsmith. Elucidating energy pathways through simultaneous measurement of absorption and transmission in a coupled plasmonic-photonic cavity. *Nano Lett.*, 20(1):50–58, 2019.

[24] Feng Pan, Kristoffer Karlsson, Austin G Nixon, Levi T Hogan, Jonathan M Ward, Kevin C Smith, David J Masiello, Sile Nic Chormaic, and Randall H Goldsmith. Active control of plasmonic–photonic interactions in a microbubble cavity. *J. Phys. Chem. C*, 126(48):20470–20479, 2022.

[25] Kevin D Heylman, Niket Thakkar, Erik H Horak, Steven C Quillin, Charles Cherqui, Kassandra A Knapper, David J Masiello, and Randall H Goldsmith. Optical microresonators as single-particle absorption spectrometers. *Nat. Photon.*, 10(12):788–795, 2016.

[26] Hugo M Doeleman, Ewold Verhagen, and A Femius Koenderink. Antenna–cavity hybrids: matching polar opposites for Purcell enhancements at any linewidth. *ACS Photonics*, 3(10):1943–1951, 2016.

[27] Kevin C Smith, Agust Olafsson, Xuan Hu, Steven C Quillin, Juan Carlos Idrobo, Robyn Collette, Philip D Rack, Jon P Camden, and David J Masiello. Direct observation of infrared plasmonic Fano antiresonances by a nanoscale electron probe. *Phys. Rev. Lett.*, 123(17):177401, 2019.

[28] Martin Frimmer, Toon Coenen, and A. Femius Koenderink. Signature of a Fano resonance in a plasmonic metamolecule's local density of optical states. *Phys. Rev. Lett.*, 108:077404, Feb 2012.

[29] Sean M. Collins, Olivia Nicoletti, David Rossouw, Tomas Ostasevicius, and Paul A. Midgley. Excitation dependent Fano-like interference effects in plasmonic silver nanorods. *Phys. Rev. B*, 90:155419, Oct 2014.

[30] Nicholas W Bigelow, Alex Vaschillo, Jon P Camden, and David J Masiello. Signatures of Fano interferences in the electron energy loss spectroscopy and cathodoluminescence of symmetry-broken nanorod dimers. *ACS Nano*, 7(5):4511–4519, 2013.

[31] C Praise Anyanwu, Grace Pakeltis, Philip D Rack, and David J Masiello. Nanoscale characterization of individual three-dimensional split ring resonator systems. *ACS Applied Optical Materials*, 1(2):607–614, 2023.

[32] Claude Cohen-Tannoudji, Jacques Dupont-Roc, and Gilbert Grynberg. Lagrangian and hamiltonian approach to electrodynamics. the standard lagrangian and the coulomb gauge. In *Photons and atoms-introduction to quantum electrodynamics*, chapter 2, pages 79–126. Wiley, New York, 1989.

[33] Marlan O. Scully and M. Suhail Zubairy. Atom-field interaction - semiclassical theory. In *Quantum Optics*, chapter 5, pages 145–160. Cambridge University Press, Cambridge, 1997.

[34] Kevin C Smith. The electromagnetic lagrangian: a bottom-up approach. In *Theoretical Models of Hybrid Light-Matter Systems and Their Applications*, chapter 1, pages 9–20. University of Washington, 2021.

[35] Frederick W Byron and Robert W Fuller. Application to classical mechanics. In *Mathematics of classical and quantum physics*, volume 1, chapter 4. Addison-Wesley, 1969.

[36] Kevin C Smith. Theoretical formalism for coupled dielectric cavities. In *Theoretical Models of Hybrid Light-Matter Systems and Their Applications*, chapter 8, pages 138–153. University of Washington, 2021.

[37] Eugen Merzbacher. Photons and the electromagnetic field. In *Quantum mechanics*, chapter 23, pages 569–591. John Wiley & Sons, New York, 1998.

[38] Marina Radulaski, Kevin A. Fischer, and Jelena Vučković. Chapter three - nonclassical light generation from III—V and group-IV solid-state cavity quantum systems. In Ennio Arimondo, Chun C. Lin, and Susanne F. Yelin, editors, *Advances In Atomic, Molecular, and Optical Physics*, volume 66, pages 111–179. Academic Press, 2017.

[39] Barak Dayan, A S Parkins, Takao Aoki, E P Ostby, K J Vahala, and H Jeff Kimble. A photon turnstile dynamically regulated by one atom. *Science*, 319(5866):1062–1065, 2008.

[40] Kevin Hennessy, Antonio Badolato, Martin Winger, D Gerace, Mete Atatüre, S Gulde, S Fält, Evelyn L Hu, and A Imamoğlu. Quantum nature of a strongly coupled single quantum dot–cavity system. *Nature*, 445(7130):896–899, 2007.

[41] Andrei Faraon, Ilya Fushman, Dirk Englund, Nick Stoltz, Pierre Petroff, and Jelena Vučković. Coherent generation of non-classical light on a chip via photon-induced tunnelling and blockade. *Nat. Phys.*, 4(11):859–863, 2008.

[42] Thomas Volz, Andreas Reinhard, Martin Winger, Antonio Badolato, Kevin J Hennessy, Evelyn L Hu, and Ataç Imamoğlu. Ultrafast all-optical switching by single photons. *Nat. Photonics*, 6(9):605–609, 2012.

[43] H. Flayac and V. Savona. Unconventional photon blockade. *Phys. Rev. Appl.*, 96:053810, Nov 2017.

[44] H. J. Snijders, J. A. Frey, J. Norman, V. Flayac, H.and Savona, A. C. Gossard, J. E. Bowers, M. P. van Exter, D. Bouwmeester, and W. Löffler. Observation of the unconventional photon blockade. *Phys. Rev. Lett.*, 121:043601, Jul 2018.

[45] Ataç Imamoğlu, H. Schmidt, G. Woods, and M. Deutsch. Strongly interacting photons in a nonlinear cavity. *Phys. Rev. Lett.*, 79:1467–1470, Aug 1997.

[46] Motoaki Bamba, Atac Imamoğlu, Iacopo Carusotto, and Cristiano Ciuti. Origin of strong photon antibunching in weakly nonlinear photonic molecules. *Phys. Rev. Appl.*, 83:021802, Feb 2011.

[47] H. J. Carmichael, R. J. Brecha, and P. R. Rice. Quantum interference and collapse of the wavefunction in cavity qed. *Opt. Commun.*, 82(1):73–79, 1991.

[48] Arka Majumdar, Michal Bajcsy, Armand Rundquist, and Jelena Vučković. Loss-enabled sub-Poissonian light generation in a bimodal nanocavity. *Phys. Rev. Lett.*, 108(18):183601, 2012.

[49] Xiaodong Yang, Atsushi Ishikawa, Xiaobo Yin, and Xiang Zhang. Hybrid photonic- plasmonic crystal nanocavities. *ACS nano*, 5(4):2831–2838, 2011.

[50] Pai Peng, Yong-Chun Liu, Da Xu, Qi-Tao Cao, Guowei Lu, Qihuang Gong, Yun-Feng Xiao, et al. Enhancing coherent light-matter interactions through microcavity-engineered plasmonic resonances. *Physical review letters*, 119(23):233901, 2017.

[51] Burak Gurlek, Vahid Sandoghdar, and Diego Martín-Cano. Manipulation of quenching in nanoantenna–emitter systems enabled by external detuned cavities: a path to enhance strong-coupling. *ACS Photonics*, 5(2):456–461, 2018.

[52] Michael Barth, Stefan Schietinger, Sabine Fischer, Jan Becker, Nils Nusse, Thomas Aichele, Bernd Lochel, Carsten Sonnichsen, and Oliver Benson. Nanoassembled plasmonic-photonic hybrid cavity for tailored light-matter coupling. *Nano letters*, 10(3):891–895, 2010.

[53] Ye Luo, Maysamreza Chamanzar, Aniello Apuzzo, Rafael Salas-Montiel, Kim Ngoc Nguyen, Sylvain Blaize, and Ali Adibi. On-chip hybrid photonic–plasmonic light concentrator for nanofocusing in an integrated silicon photonics platform. *Nano letters*, 15(2):849–856, 2015.

[54] Shanying Cui, Xingyu Zhang, Tsung-li Liu, Jonathan Lee, David Bracher, Kenichi Ohno, David Awschalom, and Evelyn L Hu. Hybrid plasmonic photonic crystal cavity for enhancing emission from near-surface nitrogen vacancy centers in diamond. *ACS Photonics*, 2(4):465–469, 2015.

[55] Anael Ben-Asher, Antonio I. Fernández-Domínguez, and Johannes Feist. Non-Hermitian anharmonicity induces single-photon emission. *Phys. Rev. Lett.*, 130:243601, Jun 2023.

[56] A. Ridolfo, O. Di Stefano, N. Fina, R. Saija, and S. Savasta. Quantum plasmonics with quantum dot-metal nanoparticle molecules: Influence of the Fano effect on photon statistics. *Phys. Rev. Lett.*, 105:263601, Dec 2010.

[57] A. P. Foster, D. Hallett, I. V. Iorsh, S. J. Sheldon, M. R. Godsland, B. Royall, E. Clarke, I. A. Shelykh, A. M. Fox, M. S. Skolnick, I. E. Itskevich, and L. R. Wilson. Tunable photon statistics exploiting the Fano effect in a waveguide. *Phys. Rev. Lett.*, 122:173603, May 2019.

[58] Claude Cohen-Tannoudji, Jacques Dupont-Roc, and Gilbert Grynberg. C—observables and states of the quantized free field. In *Photons and atoms-introduction to quantum electrodynamics*, chapter 3, pages 183–189. Wiley, New York, 1989.

[59] Rodney Loudon. Photon bunching and antibunching. *Physics Bulletin*, 27(1):21, 1976.

[60] J Robert Johansson, Paul D Nation, and Franco Nori. Qutip: An open-source python framework for the dynamics of open quantum systems. *Computer Physics Communications*, 183(8):1760–1772, 2012.

[61] Marlan O. Scully and M. Suhail Zubairy. Quantum theory of radiation. In *Quantum Optics*, chapter 5, pages 20–34. Cambridge University Press, Cambridge, 1997.

[62] Alessandro Zavatta, Silvia Viciani, and Marco Bellini. Quantum-to-classical transition with single-photon-added coherent states of light. *science*, 306(5696):660–662, 2004.

[63] Marlan O. Scully and M. Suhail Zubairy. Quantum theory of damping—heisenberg-langevin approach. In *Quantum Optics*, chapter 9, pages 271–288. Cambridge University Press, Cambridge, 1997.

[64] Lev Samuel Bishop. Circuit qed. In *Circuit quantum electrodynamics*, chapter 2. Yale University, 2010.

[65] Max Wagner. General introduction. In *Unitary Transformations in Solid State Physics*, volume 15 of *Modern Problems in Condensed Matter Sciences*, chapter 1, pages 3–6. North-Holland Physics Publishing, 1986.

[66] Niket Thakkar, Charles Cherqui, and David J Masiello. Quantum beats from entangled localized surface plasmons. *ACS Photonics*, 2(1):157–164, 2015.

Chapter 3

SPECTROSCOPY IN NANOSCOPIC CAVITIES – MODELS AND RECENT EXPERIMENTS

3.1 Abstract

The ability of nanophotonic cavities to confine and store light to nanoscale dimensions has important implications for enhancing molecular, excitonic, phononic, and plasmonic optical responses. Spectroscopic signatures of processes that are ordinarily exceedingly weak such as pure absorption and Raman scattering have been brought to the single-particle limit of detection, while new emergent polaritonic states of optical matter have been realized through coupling material and photonic cavity degrees of freedom across a wide range of experimentally accessible interaction strengths. In this review, we discuss both optical and electron beam spectroscopies of cavity-coupled material systems in weak, strong, and ultrastrong coupling regimes, providing a theoretical basis for understanding the physics inherent to each, while highlighting recent experimental advances and exciting future directions.

3.2 Introduction

Environmental boundaries can strongly influence otherwise unremarkable free space wave behavior leading to unexpected and even exceptional wave phenomena. Acoustic whispering galleries in domed architectural structures [1], efficient radio-frequency surface wave propagation near the Earth's surface [2], optical cloaking in metamaterials [3, 4], and even corralling [5] and scarring [6] of quantum matter waves represent

just a few examples spanning acoustic, electromagnetic, and quantum realms.

Reported originally in 1966, Drexhage experimentally examined the important situation of a molecular dye (a europium dibenzoylmethane complex) positioned in the vicinity of a gold interface, acting as a mirror boundary for the molecule's fluorescent emission [7, 8]. When excited, the dye's radiation was reflected from the gold mirror, subsequently interfering against its own non-reflected emission, and resulting in observed modifications to the dye's free-space angular radiation profile and lifetime. Intuitive arguments based on path length differences between the non-reflected and reflected emission components were later quantitatively shored up in the theoretical work of Kuhn [9] and summarized in Chance, Prock, and Silbey's famous review [10], where the dye's lifetime and resonance frequency modifications were made explicit through use of a damped-driven oscillator model incorporating the reflected field set up by the specific boundary conditions of the gold mirror.

EMLDOSThe electromagnetic local density of states counts the number of electromagnetic states per unit volume per unit frequency.

Today we understand Drexhage's experiments, like Purcell's earlier description of the enhancement of spontaneous emission of nuclear magnetic moment transitions coupled to a resonant electrical circuit [11], to be fundamentally governed by the increase in the electromagnetic local density of states (EMLDOS), ρ, induced by the environment over that occurring in free space $\rho_0 = \omega^2/\pi^2 c^3$. (Gaussian units are used throughout, and dimensions of all important quantities are provided in the Supplemental Material.) Essentially all radiative processes in which emitters interact with modified electromagnetic environments can also be explained by modification of ρ/ρ_0. Surface-enhanced Raman scattering (SERS), surface-enhanced fluorescence, and scanning near-field optical microscopy represent three notable examples that take advantage of the remarkable ability of surface plasmon resonances, occurring in metallic nanocavities [12, 13], to modify the EMLDOS through their efficient coupling of free-space radiation to the near-field. In addition to metallic cavities, a diverse

range of dielectric microcavities [14], including whispering gallery mode microresonators (WGM) [15], (e.g., microtoroid, microsphere, and microbubble platforms), Fabry-Pérot interferometers [16], and photonic crystals [17, 18, 19], may be viewed as receptacles for light with high quality (Q) factors, capable of trapping and storing electromagnetic waves for exceedingly long times ($\sim$ 100 ns), thereby providing substantial EMLDOS modification capabilities. This review will examine recent experiments in which nanophotonic cavities are utilized to detect and spectroscopically characterize a broad range of molecular, solid state, and nanophotonic systems.

Prominent in each of these examples is the central role and influence of the environment upon the system. Such processes operate in a regime of *weak coupling*, whereby the rate of energy lost to the environment exceeds the rate of energy transferred between system components. In either case the environment serves as a perturbatively connected reservoir, but the original basis characterizing the system remains the physically relevant basis of description. As a result, spectroscopic features are qualitatively reminiscent of the system in empty space.

In the opposite regime lie physical systems that are so well isolated that environmental coupling can be completely ignored and only coherent energy exchange between different system components is of importance. In this so-called *strong coupling regime*, spectroscopic signatures of the system no longer resemble those of its original uncoupled states and the appropriate representation is that of mixed or normal modes such as the familiar in-phase and out-of-phase oscillations of a pair of coupled oscillators. Such strongly coupled systems can occur in many different ways, blended in either matter-matter, matter-light, or light-light combinations, and realized, e.g., in coupled plasmonic nanostructures composed of noble metal nanoparticles, solid-state exciton polaritons formed through the hybridization of 2D transition metal dichalcogenides and nanophotonic cavities, or photonic molecules constructed in exquisitely engineered assemblies of optical resonators, respectively. In some cases, experimental knobs exist to actively tune the degree of mode mixing, while in exceptional situations

there exists so much control that strongly coupled systems can even be driven into the weak coupling regime and back again such as in tip-enhanced photoluminescence (TEPL) measurements.

In this review, we focus on spectroscopic observations of weakly- and strongly-coupled plasmonic, excitonic, molecular, and nanophotonic systems reported in the recent literature (Figure 3.1). Spectroscopic observables of relevance herein include both near- (TEPL and nanoscale Fourier transform infrared (nano-FTIR)) and far-field (absorption, SERS) optical measurements as well as those based upon the inelastic scattering of focused electron beams such as electron energy loss (EEL), electron energy gain (EEG), and cathodoluminescence (CL) spectroscopies performed in an electron microscope. Specifically, we do not discuss molecular vibrational polariton chemistry, and only briefly describe spectroscopic observations of systems characterized by ultrastrong coupling, where the intrasystem coupling rate approaches that of the natural frequencies of the individual system components themselves.

Broadly, this review is divided into two main sections, weak and strong coupling, and emphasis is placed on the introduction of simple theoretical models that (i) capture the most salient characteristics encoded within experimental observables, (ii) provide insights on how nanophotonic cavities work to modify emission rates, and (iii) serve as a basis for more sophisticated treatments and future research directions. It is our hope that beginning graduate students and advanced researchers who are interested in learning a new field will find this review useful as a first step into the recent literature and in understanding the basic concepts upon which it depends.

3.3 Weakly Coupled Systems

The rate at which energy is lost from a physical system to its environment can be due to a myriad of different radiative and nonradiative mechanisms and pathways. The *weak coupling regime* is distinguished by the situation in which the rate of system-environmental coupling (γ) exceeds that of intrasystem coupling (g). In this regime

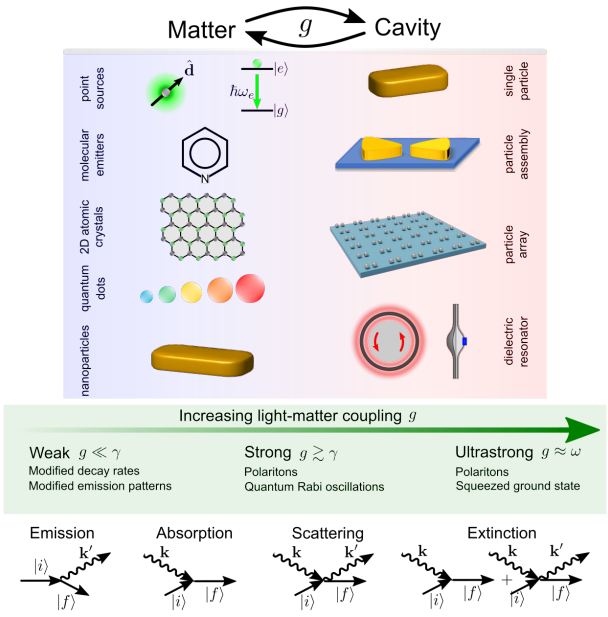

Figure 3.1: Overview of coupled light-matter degrees of freedom involving atomic, molecular, excitonic, plasmonic, and phononic material components interacting with individual, composite, and structured nanophotonic cavity environments. The degree of light-matter coupling (g) relative to loss (γ) dictates the observed physical characteristics of each system. Displayed at the bottom are diagrammatic representations of familiar light-matter interaction processes which may be probed using both far-field and near-field optical and electron beam sources. The sinusoidal arrows represent photons of wavevector $\mathbf{k}$ and $\mathbf{k}'$, while the straight arrows represent initial and final material states labeled by $|i\rangle$ and $|f\rangle$, respectively.

different system components merely dress each other as energy flows from one component to another, only to be immediately outcoupled to the envionment and forever lost. From a theoretical perspective, perturbation theory serves as an effective calculation tool. However, gone are the familiar Hermitian Hamiltonians and their unitary time evolution: description of such open systems requires Hamiltonians that are fundamentally non-Hermitian in character [20, 21].

Numerous important spectroscopic phenomena in micro and nanoscopic cavities are well characterized as occurring in the weak-coupling regime. Examples include: (i) the Purcell effect whereby the rate of spontaneous emission of a quantum emitter to the radiation field can be influenced by its coupling to a mode of an optical or plasmonic cavity in/on which it is located [22, 23, 24, 25, 26, 27]; (ii) the plasmonic Fano effect in which a spectrally narrow plasmonic mode is weakly coupled to and receives energy from another that is significantly lossier [28, 29, 30, 31, 32, 33, 34] leading to pronounced asymmetric resonance lineshapes or "cut-outs" in the composite system spectrum. Such antiresonance phenomena were originally characterized by Fano in his theoretical analysis of the autoionization spectrum of He vapor [35] measured by Lassettre and Silverman [36, 37] via EEL spectroscopy; and (iii) surface-enhanced Raman scattering where the exceedingly small cross section for inelastic light scattering by a molecular system is increased due to coupling of the incident laser and scattered molecular fields to the strong antenna-like resonances of a nearby plasmonic nanostructure [38, 39, 40, 41, 42].

Many other notable examples of cavity-modified spectroscopic phenomena exist in the literature, but here we focus primarily on the Fano, Purcell, and SERS effects. Specific discussion of these effects appears below in Sections 2.1, 2.4, and 2.6. Generic to such phenomena are the following set of Newton equations, which may be derived either classically or quantum mechanically, representing a weakly coupled emitter-

cavity system [31]

$$\begin{aligned} m\ddot{q}_e + m\gamma_e^{\mathrm{nr}}\dot{q}_e + m\omega_e^2 q_e - g_{pq}(\mathbf{s})\sqrt{\frac{m}{V}}\dot{q}_c &= -eE_0 e^{-i\omega t} + \frac{2e^2}{3c^3}\dddot{q}_e \\ \frac{1}{V}\ddot{q}_c + \frac{1}{V}\gamma_c^{\mathrm{tot}}(\omega)\dot{q}_c + \frac{1}{V}\omega_c^2 q_c + g_{pq}(\mathbf{s})\sqrt{\frac{m}{V}}\dot{q}_e &= 0 \end{aligned} \tag{3.1}$$

with coupling strength $g_{pq}(\mathbf{s}) = -e\sqrt{4\pi/mV}\mathbf{f}(\mathbf{s})\cdot\hat{\mathbf{q}}_e$. Here, q_e ($\mathbf{q}_e = \hat{\mathbf{q}}_e q_e$) represents the emitter's dynamical coordinate with effective mass m, nonradiative decay rate γ_e^{nr}, and natural frequency ω_e, and q_c represents the cavity's dynamical coordinate of mode volume V, spatial mode profile $\mathbf{f}(\mathbf{x})$, total (nonradiative + radiative) decay rate $\gamma_c^{\mathrm{tot}}(\omega)$, and natural frequency ω_c. Treatment of lossy cavities necessitates a more nuanced description where the mode functions $\mathbf{f}(\mathbf{x})$ become quasinormal modes with associated complex-valued eigenfrequencies [43, 44, 45, 46, 47, 48, 49]. The emitter, located at the position $\mathbf{s}$ within the cavity field $\mathbf{E}(\mathbf{x},t) = -(\sqrt{4\pi}/V)\mathbf{f}(\mathbf{x})\dot{q}_c(t)$, is coupled to a harmonic driving field E_0 and to the free radiation field via the radiation reaction force $F_{\mathrm{rad}} = (2e^2/3c^3)\dddot{q}_e = -m\gamma_e^{\mathrm{rad}}(\omega)\dot{q}_e$ with radiative decay rate $\gamma_e^{\mathrm{rad}}(\omega) = 2e^2\omega^2/3mc^3 = (2\pi^2e^2/3m)\rho_0$ [50] expressed in terms of the free space EMLDOS, where $-e$ is the elementary charge and c is the speed of light in vacuum.

For multimode cavities, the mode functions $\mathbf{f}_\ell(\mathbf{x})$ and their associated dynamical coordinates $q_\ell^c(t)$ define the cavity vector potential (in the generalized Coulomb gauge $\nabla\cdot[\varepsilon(\mathbf{x})\mathbf{A}(\mathbf{x})] = 0$) as $\mathbf{A}(\mathbf{x},t) = \sum_\ell(\sqrt{4\pi}c/V_\ell)\mathbf{f}_\ell(\mathbf{x})q_\ell^c(t)$, where the individual spatial mode functions satisfy the vector Helmholtz equation $\nabla\times\big(\nabla\times\mathbf{f}_\ell(\mathbf{x})\big) = \varepsilon(\mathbf{x})(\omega_\ell^2/c^2)\mathbf{f}_\ell(\mathbf{x})$ on the domain of the cavity described by the piecewise dielectric function $\varepsilon(\mathbf{x})$ with eigenfrequencies ω_ℓ, mode amplitudes $q_\ell^c(t)$, and mode volumes $V_\ell = \int\varepsilon(\mathbf{x})|\mathbf{f}_\ell(\mathbf{x})|^2 d^3x/\max[\varepsilon(\mathbf{x})|\mathbf{f}_\ell(\mathbf{x})|^2]$. In such cases the cavity electric field generalizes accordingly as $\mathbf{E}(\mathbf{x},t) = -\sum_\ell(\sqrt{4\pi}/V_\ell)\mathbf{f}_\ell(\mathbf{x})\dot{q}_\ell^c(t)$, as does the light-matter coupling $g_{pq}(\mathbf{s}) = -e\sum_\ell\sqrt{4\pi/mV_\ell}\mathbf{f}_\ell(\mathbf{s})\cdot\hat{\mathbf{q}}_e$.

In the simplified case of a single cavity mode coupled weakly to an emitter driven in steady state, the emitter oscillates with the frequency of the driving field $E_0(t) =$

$\mathrm{Re}\{E_0(\omega)e^{-i\omega t}\}$, such that $q_e(t) = \mathrm{Re}\{q_e(\omega)e^{-i\omega t}\}$, with oscillator amplitude

$$\begin{aligned} q_e(\omega) &= \frac{-eE_0/m}{\underbrace{\omega_e^2 - \mathrm{Re}\frac{g^2\omega^2}{\omega_c^2 - i\omega\gamma_c^{\mathrm{tot}} - \omega^2}}_{\tilde{\omega}_e^2} - i\Big[\underbrace{\omega\gamma_e^{\mathrm{tot}} + \mathrm{Im}\frac{g^2\omega^2}{\omega_c^2 - i\omega\gamma_c^{\mathrm{tot}} - \omega^2}}_{\omega\tilde{\gamma}_e}\Big] - \omega^2} \\ &= \underbrace{\frac{-eE_0/m}{\omega_e^2 - i\omega\gamma_e^{\mathrm{tot}} - \omega^2}}_{q_e^0(\omega)} \cdot \frac{\omega_c^2 - i\omega\gamma_c^{\mathrm{tot}} - \omega^2}{\underbrace{\omega_c^2 - \frac{g^2\omega^2(\omega_e^2 - \omega^2)}{(\omega_e^2 - \omega^2)^2 + (\omega\gamma_e^{\mathrm{tot}})^2}}_{\tilde{\omega}_c^2} - i\omega\Big[\underbrace{\gamma_c^{\mathrm{tot}} + \frac{g^2\omega^2\gamma_e^{\mathrm{tot}}}{(\omega_e^2 - \omega^2)^2 + (\omega\gamma_e^{\mathrm{tot}})^2}}_{\tilde{\gamma}_c}\Big] - \omega^2}, \end{aligned} \tag{3.2}$$

where $\gamma_e^{\mathrm{tot}}(\omega) = \gamma_e^{\mathrm{nr}} + \gamma_e^{\mathrm{rad}}(\omega)$ is the total decay rate of the emitter. The first form of the emitter's oscillator amplitude shows how its natural resonance frequency $\tilde{\omega}_e(\omega)$ and decay rate $\tilde{\gamma}_e(\omega)$ are modified due to coupling with a cavity. In the weak coupling regime both $\tilde{\omega}_e(\omega) \approx \tilde{\omega}_e(\omega_e)$ and $\tilde{\gamma}_e(\omega) \approx \tilde{\gamma}_e(\omega_e)$ are well approximated by their values at the free-space emitter frequency ω_e. The second form shows how the emitter's oscillator amplitude can be interpreted as the amplitude of the isolated emitter $q_e^0(\omega)$ multiplied by a factor that depends upon the cavity, which will become useful in the description of Fano antiresonances.

Central to the observation of such weakly coupled light-matter systems are the cross sections for absorption and scattering. Recall that the cross section is given by the ratio of the time-averaged power absorbed or emitted (or scattered) by the emitter relative to the time-averaged incident flux of optical energy, i.e., $P/\langle S\rangle$, where $\langle S\rangle = cE_0^2/8\pi$ [50]. With the emitter's oscillatory amplitude defined, the time averaged power for absorption and scattering becomes

$$\begin{aligned} P_{\mathrm{abs}}(\omega) &= \frac{\omega}{2\pi}\int_0^{2\pi/\omega} \mathrm{Re}\Big\{-m\gamma_e^{\mathrm{nr}}\dot{q}_e(t)\Big\}\cdot\mathrm{Re}\Big\{\dot{q}_e(t)\Big\}\,dt \\ P_{\mathrm{scat}}(\omega) &= \frac{\omega}{2\pi}\int_0^{2\pi/\omega} \mathrm{Re}\Big\{-m\gamma_e^{\mathrm{rad}}(\omega)\dot{q}_e(t)\Big\}\cdot\mathrm{Re}\Big\{\dot{q}_e(t)\Big\}\,dt, \end{aligned} \tag{3.3}$$

where $2\pi/\omega$ is the period of oscillation. These equations show that the power absorbed or scattered stem from the work performed by the dissipative forces $F_{\mathrm{nr}} = -m\gamma_e^{\mathrm{nr}}\dot{q}_e$

and $F_{\rm rad} = -m\gamma_e^{\rm rad}(\omega)\dot{q}_e$ upon the oscillator. It follows that the absorption and scattering cross sections can be expressed as

$$\begin{aligned}\sigma_{\rm abs}(\omega) &= \frac{4\pi\omega^2}{c}\frac{m}{E_0^2}\gamma_e^{\rm nr}|q_e(\omega)|^2 \\ \sigma_{\rm scat}(\omega) &= \frac{4\pi\omega^2}{c}\frac{m}{E_0^2}\gamma_e^{\rm rad}(\omega)|q_e(\omega)|^2.\end{aligned} \tag{3.4}$$

Recognizing that the cavity-dressed emitter's induced dipole moment is defined as $d(\omega) = -eq_e(\omega) = \alpha(\omega)E_0$, implicitly defines the dressed polarizability as

$$\alpha(\omega) = \frac{e^2/m}{\tilde{\omega}_e^2 - i\omega\tilde{\gamma}_e - \omega^2} \tag{3.5}$$

which reduces back to the familiar free-space emitter polarizability $\alpha_0(\omega) = (e^2/m)/(\omega_e^2 - i\omega\gamma_e^{\rm tot} - \omega$ in the limit $g \to 0$. In this limit, the above cross sections attain their familiar forms [31]

$$\begin{aligned}\sigma_{\rm abs}(\omega) &= \frac{4\pi\omega}{c}\frac{\gamma_e^{\rm nr}}{\gamma_e^{\rm tot}}{\rm Im}\,\alpha_0(\omega) = \frac{4\pi\omega}{c}\big(\omega\gamma_e^{\rm nr}\big)\frac{e^2/m}{(\omega_e^2-\omega^2)^2 + (\omega\gamma_e^{\rm tot})^2} \\ \sigma_{\rm scat}(\omega) &= \frac{4\pi\omega}{c}\frac{\gamma_e^{\rm rad}(\omega)}{\gamma_e^{\rm tot}}{\rm Im}\,\alpha_0(\omega) = \frac{8\pi}{3}\Big(\frac{\omega}{c}\Big)^4\Big|\frac{e^2/m}{\omega_e^2 - i\omega\gamma_e^{\rm tot} - \omega^2}\Big|^2,\end{aligned} \tag{3.6}$$

and the sum defines the extinction (total) cross section $\sigma_{\rm ext}(\omega) = \sigma_{\rm abs}(\omega) + \sigma_{\rm scat}(\omega) = (4\pi\omega/c){\rm Im}\,\alpha_0(\omega)$. The absorption cross section is a measure of the amount of incident electromagnetic energy that is dissipated into heat, while the scattering cross section characterizes the amount of incident electromagnetic energy returned back into the radiative far field.

3.3.1 Fano Resonance

Relevant to a set of experiments measuring the absorption spectra of individual nano-objects independently from scattering, extinction, and emission, is the Fano effect, which was originally observed in the autoionization spectrum of He vapor by Silverman and Lassettre [36] in 1959. Fano understood the pronounced asymmetric antiresonance lineshapes measured in the spectrum as being due to the interaction of

two electronic configurations of He [35]—the discrete $2s2p$ double excitation, which is above the first ionization threshold, and the autoionization continuum. In the years that have followed such asymmetric lineshapes (now called Fano antiresonances, Fano resonances, or Fano interferences) have been observed in many different physical systems characterized under both optical [29, 31, 51, 52, 53] and electron beam [30, 54, 34, 28, 55] probes whenever discrete and continuum channels weakly interact. In such cases the spectrum of the interacting system taken in ratio to the spectrum of the continuum channel can be arranged as $\sigma_{\rm int}(\omega)/\sigma_{\rm cont}(\omega) = |(\mathcal{Q}+\epsilon)/(\epsilon+i)|^2$, where the Fano asymmetry parameter $\mathcal{Q}$ is a frequency-independent number in the vicinity of the antiresonance that can be positive, negative, or zero and completely characterizes the asymmetry of the lineshape, while ϵ is a reduced frequency taken with respect to the frequency of the discrete mode.

Through appropriate choice of parameters, the pair of coupled oscillator equations in Eq. (3.1) can be used to model the absorption spectra of individual emissive nano-objects coupled, e.g., to a nanophotonic resonator cavity, where Fano resonances are observed whenever the nano-object's linewidth is large in comparison to that of the nanophotonic resonator modes to which it is weakly coupled. With the emitter's total decay rate being large relative to that of the cavity, i.e., $\gamma_e^{\rm tot} \gg \gamma_c^{\rm tot}$ and the emitter cavity coupling rate g being less than $\gamma_e^{\rm tot}$, the absorption spectrum of the composite emitter-cavity system becomes

$$\begin{aligned}
\sigma_{\rm abs}(\omega) &= \frac{4\pi\omega^2}{c}\frac{m}{E_0^2}\gamma_e^{\rm nr}|q_e(\omega)|^2 \\
&= \underbrace{\frac{4\pi\omega^2}{c}\frac{m}{E_0^2}\gamma_e^{\rm nr}|q_e^0(\omega)|^2}_{\sigma_{\rm abs}^0} \cdot \left|\frac{(\tilde{\omega}_c^2+i\omega\gamma_c-\omega_c^2)/(\omega\tilde{\gamma}_c)+(\omega^2-\tilde{\omega}_c^2)/(\omega\tilde{\gamma}_c)}{(\omega^2-\tilde{\omega}_c^2)/(\omega\tilde{\gamma}_c)+i}\right|^2 \\
&= \sigma_{\rm abs}^0(\omega)\cdot\left|\frac{\mathcal{Q}+\epsilon}{\epsilon+i}\right|^2,
\end{aligned} \tag{3.7}$$

where the factor modifying the absorption spectrum $\sigma_{\rm abs}^0(\omega)$ of the isolated free-space emitter accounts for the fact that the emitter is weakly coupled to a high-Q cav-

ity in addition to the radiation continuum. It is this factor that produces a sharp asymmetric lineshape, centered about ω_c or $\epsilon(\omega) = -\mathcal{Q}$, which appears as a "cut-out" (or antiresonance) in the Lorentzian absorption spectrum $\sigma^0_{\text{abs}}(\omega)$ of the emitter. Implicitly defined within Eq. (3.7) are the equations $\epsilon(\omega) = (\omega^2 - \tilde{\omega}_c^2)/\omega\tilde{\gamma}_c$ and $\mathcal{Q}(\omega) = (\tilde{\omega}_c^2 + i\omega\gamma_c - \omega_c^2)/\omega\tilde{\gamma}_c$. In the limit of a lossless cavity, $\mathcal{Q} \to (\tilde{\omega}_c^2 - \omega_c^2)/\omega\tilde{\gamma}_c$, making explicit the dependence of the Fano lineshape upon detuning. While the latter is a function of frequency, we emphasize that Fano resonances are described only when $\mathcal{Q}$ is constant in the vicinity of the cavity resonance at ω_c. Accurate spectroscopic determination of $\mathcal{Q}$ must be treated with care [29, 31, 51, 52] as, e.g., interfering optical pathways occurring in scattering observables may spuriously enhance/suppress spectral asymmetries, making pure absorption measurements ideal for quantification of $\mathcal{Q}$. Figure 3.2(a), (b) show examples of Fano antiresonance lineshapes associated with $\mathcal{Q} < 0$, $\mathcal{Q} = 0$, and $\mathcal{Q} > 0$, measured via single-particle absorption spectroscopy.

3.3.2 Absorption

Absorption measurements of individual nano-objects (nanoparticles or molecules) have been widely reported since the first demonstration of single-molecule absorption at cryogenic temperatures in 1989 [56] and subsequently at room temperature in 2010 [57, 58]. Since absorption and scattering cross sections have different dependencies upon target size (absorption and scattering depend linearly and quadratically upon volume, respectively), the absorption spectrum of a small nano-object (in comparison to the wavelength) can be approximated by extinction and obtained by measuring its reflected and/or transmitted power as its scattering cross section is negligible. However, for a larger nano-objects that appreciably scatter, measuring absorption independent of scattering in the far field is challenging.

An indirect measurement based on the photothermal effect leverages photothermally-induced changes in a nano-object's local refractive index due to optical excitation [59, 52, 60, 61, 62, 63] to provide an avenue to separate absorption from scattering

for nano-objects that are large enough to scatter. One class of spectroscopies that takes advantage of such photothermal absorption utilizes optical microresonators as near-field thermometers to measure the absorption of single nanoparticles [52, 29, 31, 51, 64, 65, 66, 67] and polymers [68, 69]. Using this approach, the absorption spectra of individual gold nanoparticles coupled to a microcavity were systematically investigated [52, 29, 31, 51].

In 2016, Heylman et al. employed ultrahigh-quality-factor (Q) whispering-gallery-mode (WGM) toroidal microcavities as single-particle absorption spectrometers to examine single gold nanorods coupled to toroidal microcavities [52]. The measured absorption spectra (Figure 3.2a) were imprinted with distinctive spectral features as a result of the weak coupling between the nanoparticle's lossy dipolar localized surface plasmon (LSP) and the spectrally narrow photonic modes of the microresonator. This lead to cavity-modified resonances on top of a broad LSP absorption envelope. Due to the weakly coupled broad LSP mode and quasidiscrete WGM modes, Fano antiresonance signatures with linewidths of a few μeV were observed within the absorption spectrum of each individual gold nanorod (Figure 3.2a). These Fano signatures manifested as distinctly asymmetric lineshapes with constructive and destructive interference peaks and dips as the LSP-WGM detuning was varied. Subsequently, Thakkar et al. realized a thermal annealing method to control LSP-WGM detunings and consequently sculpt the asymmetry profile of the Fano lineshapes [29], where it was found that the small but finite damping of the resonator's WGM modes was important in the description of the Fano lineshape evolution (Figure 3.2b). The thermal annealing strategy employed was found to be a facile route to tune the degree of LSP-WGM hybridization and was ultimately used to obtain an optimized Purcell factor of 10^4.

Another way to tune plasmonic-photonic interactions is to directly control LSP-WGM coupling. Pan et al. implemented a WGM microfluidic platform, allowing one to control mode overlap by changing the dielectric environment [51]. Specifically, additional WGMs were made accessible to the LSP mode by flowing solvents within

the microbubble resonator, thereby creating glass-liquid interfacial modes with better mode overlap (Figure 3.2c). Huang et al. utilized a direct absorption measurement approach in a different plasmonic-photonic system where absorption dominates over extinction. A large absorption enhancement was observed and was continuously tunable across a large spectral range ($600-1000$ nm), as opposed to the weak absorption measured in uncoupled gold nanostars [70]. The Lorentzian peak lineshape was preserved across the uncoupled LSP's absorption range, unlike in LSP-WGM coupled systems. This absorption enhancement was enabled by photonic crystal guided mode resonances, where the angle-dependent spectral tunability for absorption enhancement follows the photonic crystal guided mode resonance dispersion (Figure 3.2d).

3.3.3 Reflection, Transmission, and Electron Probes

Plasmonic-photonic coupled systems can also be interrogated through tapered optical fiber transmission [71, 31] or (free-space or fiber) reflection measurements [72, 73, 74, 75]. In a coupled LSP-WGM system, Ruesink et al. observed a blue shift in the measured transmission resonance through a tapered optical fiber as the pitch size in an array of nanoantennas decreased [71]. Such strong resonance shifts perturbed by the nanoantennas, which exceeded the effects exerted by the nanoantenna's polarizability, were attributed to a nontrivial phase relationship between the WGM cavity and LSP radiation (Figure 3.3a). In a similar system, the authors measured specular reflection from the array of nanoantennas coupled to a WGM cavity through a high-NA objective while changing the incident angle [73]. The resonance lineshapes in the reflection spectra were found to vary drastically as the in-plane k-vector increased. These measurements suggest that nanoantenna polarizability can be controlled through backaction via a single cavity mode for the entire nanoantennna array (Figure 3.3b). Recently the authors showed the ability to obtain fiber reflection, transmission, and free-space scattering simultaneously (Figure 3.3c) by driving the coupled system with a narrow-band tunable laser through a tapered optical fiber

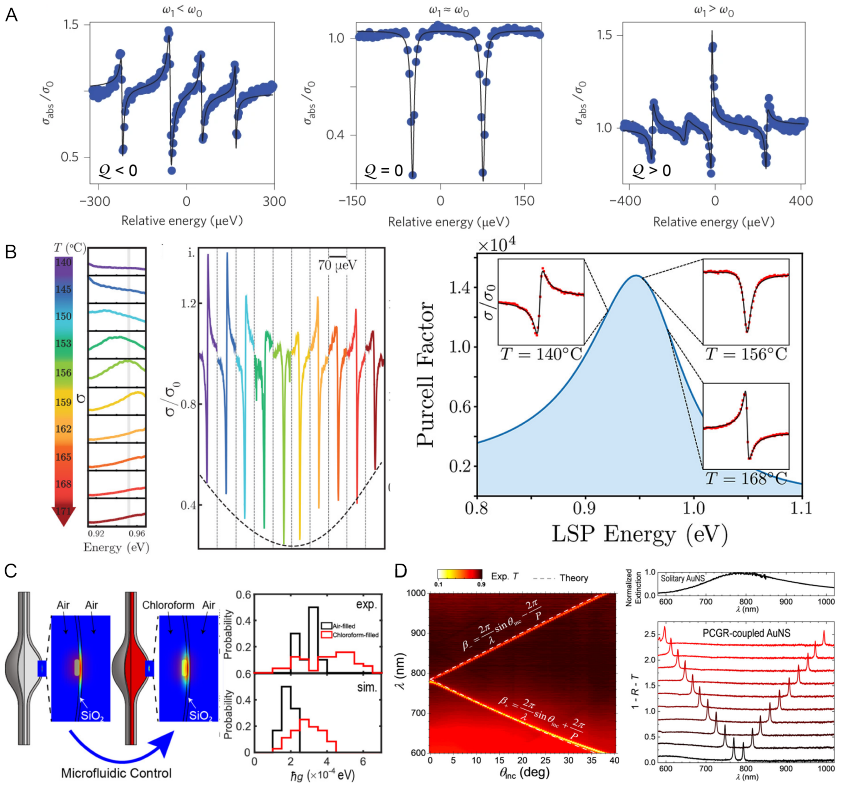

Figure 3.2: Absorption measurements of plasmonic-photonic coupled systems. (a) Fano lineshapes as a function of LSP-WGM detuning. (b) Detuning LSP resonance from a single WGM via thermal annealing. (c) Active control of plasmonic-photonic coupling in a microfluidic cavity. (d) Absorption amplification across an extended spectral range through varying incident angle of excitation. Panel (a) adapted with permission from Reference [52]; Copyright 2016 Nature. Panels (b), (c), and (d) adapted with permission from References [29], [51], and [70] respectively; Copyright 2017, 2019, 2022 American Chemical Society.

[74, 75]. Single plasmonic nanoparticles were deterministically positioned on WGM microcavities through electron-beam lithography. A perturbed cavity mode with a broader lineshape than that for the unperturbed cavity mode suggested LSP-WGM hybridization, which was further confirmed by scattering images. Pan et al. demonstrated simultaneous measurement of absorption and transmission through a single tapered optical fiber to elucidate energy pathways in a weakly coupled LSP-WGM system [31] (Figure 3.3d). Through a combination of experimental measurement and theoretical modeling, key system parameters were found to span across 9 orders of magnitude, including LSP and WGM nonradiative and radiative dissipation rates and their mutual coupling strength.

Beyond these optical measurements, there are several recent demonstrations [30, 76] where electrons were used to probe weakly coupled systems using an electron microscope. Smith et al. combined EEL spectroscopy and theoretical modeling to reveal infrared plasmonic Fano antiresonances in a gold disk-rod dimer system (Figure 3.3e) due to the coupling between quasidiscrete Fabry-Pérot modes in the gold rod and the quasicontinuum LSP mode in the gold disk [30]. In a nanocube-microsphere coupled system (Figure 3.3f), EEL spectroscopy and CL were used to examine the broad LSP resonance in a silver nanocube modulated by discrete WGMs [76]. Interestingly, the excitation of WGMs with transverse-magnetic and/or transverse-electric polarization were controlled by changing the electron probe position on the nanocube.

3.3.4 Purcell Enhancement

Since Purcell's original report in 1946 of the ability to modify spontaneous emission rates beyond their vacuum values [11], numerous physical realizations of cavity-modified emissive processes have appeared in the literature [77]. In the context of an emitter coupled weakly to a nanophotonic cavity, the coupled equations of motion (Eq. 3.1) again suffice to describe the cavity-induced modifications to the emitter's radiative decay.

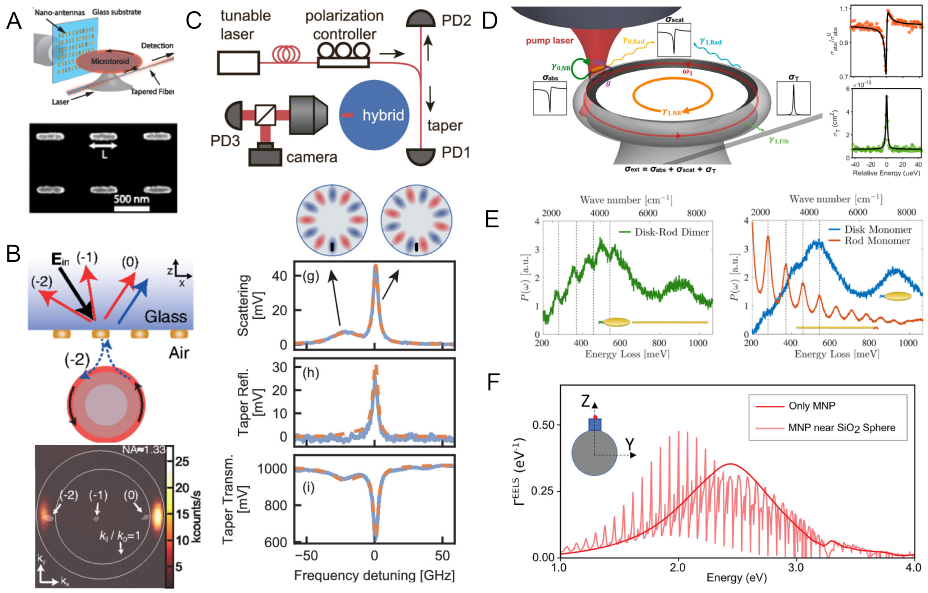

Figure 3.3: Reflection, transmission, and electron probes. (a) Transmission measurement of a WGM microcavity coupled to an array of gold nanoparticles through a tapered optical fiber. (b) Addressing the LSP-WGM coupled system through back-focal-plane reflection imaging. (c) Measuring cooperative effects between a lithographically positioned plasmonic nanoparticle and a WGM microcavity through tapered optical fiber reflection and transmission, and free-space scattering measurements. (d) Simultaneous measurement of absorption and two-sided transmission of a plasmonic-photonic coupled cavity. (e) EEL spectroscopy of a disk-rod dimer consisting of gold nanodisk and microrod (left) and their components (right). (f) EEL spectroscopy of a silver nanocube coupled to a WGM glass microsphere. Reprinted Panels (a), (b) and (e) with permission from [71], [73] and [30]; Copyright (2015), (2018) and (2019) respectively, by the American Physical Society. Panel (c) adapted from [75]; Copyright (2019) Springer Nature. Panels (d) and (f) reprinted with permission from [31] and [76]; Copyright (2019) and (2021) respectively, American Chemical Society.

In the absence of a cavity, the power scattered by an isolated emitter (into free space) recovers the well known Larmor result [50], i.e.,

$$P^0_{\text{scat}} = \frac{\omega_e}{2\pi}\int_0^{2\pi/\omega_e} \text{Re}\Big\{ -m\gamma_e^{\text{rad}}(\omega)\dot{q}_e^0(t)\Big\}\cdot \text{Re}\Big\{\dot{q}_e^0(t)\Big\}\,dt = \frac{\pi^2 e^2\omega_e^2}{3}\rho_0|q_e^0|^2 \tag{3.8}$$

for a dipole oscillator oscillating at frequency ω_e, where $\rho_0 = \omega_e^2/\pi^2c^3$ is the free-space EMLDOS. When positioned in a cavity, determination of the modifications to the emitter's dynamics requires calculation of the power scattered by the emitter into the cavity via

$$\begin{aligned} P_{\text{cav}} &= \frac{\omega_e}{2\pi}\int_0^{2\pi/\omega_e} \text{Re}\Big\{g_{pq}(\mathbf{s})\sqrt{\frac{m}{V}}\dot{q}_c(t)\Big\}\cdot \text{Re}\Big\{\dot{q}_e^0(t)\Big\}\,dt \\ &= \frac{2\pi e^2}{V}\frac{\omega_e^4\gamma_c|\mathbf{f}(\mathbf{s})\cdot\hat{\mathbf{q}}_e|^2}{(\omega_c^2-\omega_e^2)^2+(\omega_e\gamma_c)^2}|q_e^0|^2 \\ &= \frac{2\pi^3 e^2c^3}{V}\frac{\omega_e^2\gamma_c|\mathbf{f}(\mathbf{s})\cdot\hat{\mathbf{q}}_e|^2}{(\omega_c^2-\omega_e^2)^2+(\omega_e\gamma_c)^2}\rho_0|q_e^0|^2, \end{aligned} \tag{3.9}$$

where both the emitter and cavity modes oscillate in time as $e^{-i\omega_e t}$, so that the ratio

$$F_P = \frac{P_{\text{cav}}}{P^0_{\text{scat}}} = \frac{6\pi c^3}{V}\frac{\gamma_c|\mathbf{f}(\mathbf{s})\cdot\hat{\mathbf{q}}_e|^2}{(\omega_c^2-\omega_e^2)^2+(\omega_e\gamma_c)^2} \tag{3.10}$$

defines the Purcell enhancement factor. If the detuning $(\omega_c-\omega_e)$ is large relative to the cavity decay rate (γ_c) then emission is inhibited. Oppositely, if the cavity is tuned into resonance with the emitter $(\omega_c=\omega_e)$ then Purcell enhancement is maximized when the emitter's transition dipole moment is aligned with the cavity field and located at its maximum so that $|\mathbf{f}(\mathbf{s})\cdot\hat{\mathbf{q}}_e|^2 = 1$. In this case

$$F_P = \frac{6\pi c^3}{\omega_e^3}\frac{Q}{V} = \frac{3\lambda_e^3}{4\pi}\frac{Q}{V}, \tag{3.11}$$

Quality factorA dimensionless quantity that describes a cavity's temporal decay rate and therefore its ability to localize light in time. expressed in terms of the cavity quality factor $Q = \omega_c/\gamma_c$ by rewriting the emitter's resonance frequency as the wavelength $\lambda_e = 2\pi c/\omega_e$. Eq. (3.11) can also be written as the ratio

$$F_P = \frac{2Q/\pi\omega_e V}{\omega_e^2/3\pi^2c^3} = \frac{2Q/\pi\omega_e V}{\rho_0/3}, \tag{3.12}$$

where the quantity in the numerator can be thought of as the cavity-enhanced density of electromagnetic states $\rho = 2Q/\pi\omega_e V$, providing a new interpretation of the physical origin of the Purcell enhancement factor.

3.3.5 Plasmonic-Photonic Coupled Systems for Emission Control

Beyond the tailored light-matter interactions described previously, plasmonic-photonic hybrid cavities have also shown great promise in emission control [53, 75] due to their significantly modified EMLDOS as a coupled system. In 2016, Doeleman et al. theoretically demonstrated that such plasmonic-photonic cavities can achieve stronger emission enhancements (Figure 3.4a) than the cavity or antenna alone [53]. They subsequently showed Fano-lineshape engineering of the EMLDOS in a coupled cavity where single quantum dots (QDs) were precisely placed in the system's plasmonic hot spot [75]. When the nanoantenna LSP was on-resonance with WGMs, the nanoantenna EMLDOS was suppressed. However, when the LSP-WGM resonances were off-resonant, for instance, when the LSP was blue-detuned from the WGMs, the nanoantenna and WGM cavity cooperatively enhanced the EMLDOS and therefore boosted the system's fluorescence emission. It was also found that the plasmonic-photonic modes directly reshaped the emission spectra of individual QDs into Fano lineshapes ranging from pure suppression to nearly Lorentzian enhancement (Figure 3.4b). Figure 3.4 panels (c) and (d) display examples of inelastic surface-enhanced Raman scattering achieved using hybrid plasmonic-photonic cavity architectures, which are discussed more fully in the Supplementary Material.

3.3.6 Surface-Enhanced Raman Scattering

Raman scattering is a second order, instantaneous two-photon inelastic scattering process, whereby molecular analytes annihilate an incoming photon at frequency ω and emit an outgoing photon at frequency ω'. Processes involving emitted photons with energy less than (greater than) that of the incoming photon are referred to as

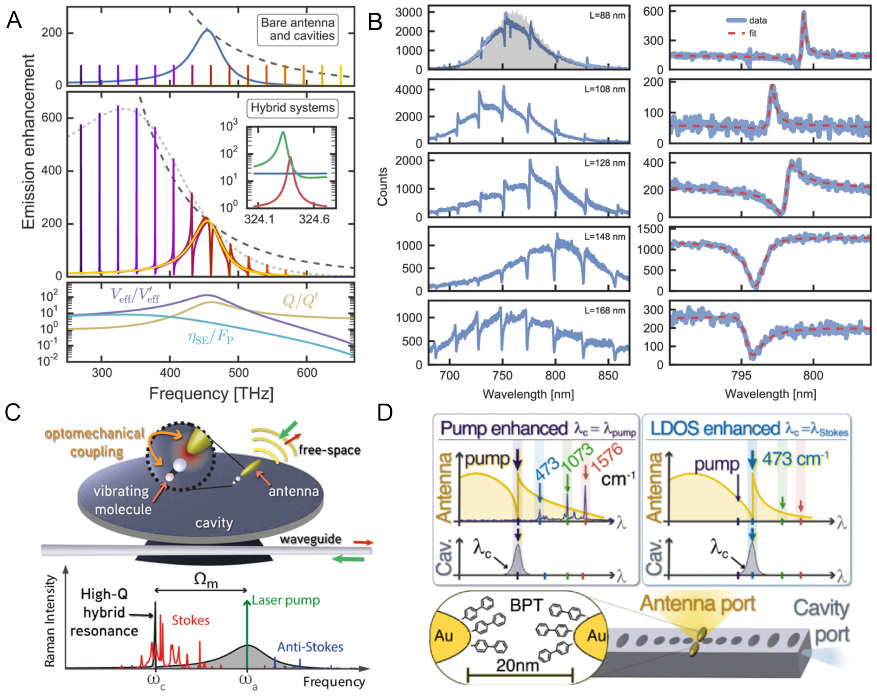

Figure 3.4: Plasmonic-photonic coupled systems. (a) Antenna-cavity hybrid systems enhancing emission. (b) The evolution of emission enhancement in single QDs as a function of antenna-cavity detuning by changing antenna's length. (c) Raman scattering enhanced by a antenna-cavity hybrid system. (d) A gold dimer decorated with BPT molecules coupled to a SiN photonic crystal nanobeam cavity. Panels (a), (b), and (c) adapted with permission from [53], [75] and [78]; Copyright (2016), (2020) and (2021) American Chemical Society. Panel (d) reprinted with permission from [79]; Copyright (2023) by the American Physical Society.

Stokes (anti-Stokes) scattering (Figure 3.5a,b, and energy differences $\hbar\omega_R = |\hbar\omega - \hbar\omega'|$ must be equal to that between initial and final internal (often vibrational) molecular states. Although the molecular vibrational spectra accessed by Raman scattering encode detailed molecular structure information, Raman signals are generally quite low, e.g., the total Raman scattering cross section for pyridine is $\sigma \sim 10^{-30}$ cm^2. However, enormous enhancement in measured Raman scattering of analytes in the presence of metal substrates with nanoscale features was observed in 1974 [82] and independently in 1977 [40, 83] with the proper interpretation based on excitation of

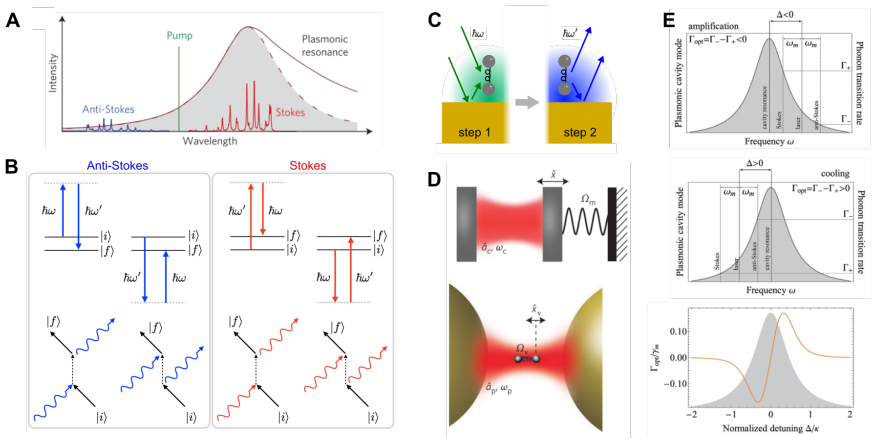

Figure 3.5: Surface-enhanced Raman scattering. (a) Example SERS spectrum. (b) Feynman diagrams for Stokes and anti-Stokes scattering along with their respective level scheme depictions. (c) Two-step phenomenological description of SERS. (d) Optomechanical model of SERS. (e) The cavity-laser drive detuning Δ dictates whether amplification ($\Gamma_{\text{opt}} < 0$) or cooling ($\Gamma_{\text{opt}} > 0$) of molecular vibrations occurs within the optomechanical model. Panels (a) and (d) adapted from [80]; Copyright (2016) Springer Nature. Panel (e) reprinted with permission from [81]; Copyright (2017) Royal Society of Chemistry.

resonant surface modes beginning shortly thereafter [84]. Today, surface-enhanced Raman scattering enhancement factors, variably defined [85], but generally a ratio of scattered powers in the presence/absence of a nanophotonic cavity, of 10^{8-12} are routinely achievable with carefully designed nanocavity systems, in some cases allowing vibrational spectra of individual molecules to be recorded with single-molecule SERS [41, 42]. While imperfect, the overall enhancement factor (EF) underlying SERS is conventionally decomposed into electromagnetic enahncement (EME) and chemical enhancement (CE) contributions with (total EF) = (EME) $\times$ (CE). CE mechanisms involve chemical modification of molecular vibrational characteristics via interaction with the cavity, e.g., due to charge transfer, necessitating a detailed microscopic quantum mechanical description [86]. This Review blackfocuses on the EME mechanism, which arises from the modification of the EMLDOS at the positions of the analyte

molecules in the presence of a nanocavity, and is generally the dominant source of SERS enhancement. An expanded discussion of current perspectives on SERS is provided in Ref. [86].

While many descriptions of SERS have been presented at varying levels of theoretical sophistication, from classical coupled dipole treatments [87], to quantum-mechanical electronic structure methods [88, 89], to many-body theories of coupled molecule-plasmon systems [90], perhaps the simplest descriptions are those provided by phenomenological models. Although truly an instantaneous second-order scattering process, one such phenomenological description of Raman scattering involves a two-step sequence consisting of induced dipole and re-emission steps as depicted in Figure 3.5c [85]. The presence of a nanophotonic cavity influences each of these steps via its modifications to the EMLDOS. During step one, a Purcell-enhanced Raman dipole moment $\mathbf{d}_R(\omega') = \bar{\boldsymbol{\alpha}}_R \cdot \mathbf{E}(\omega)$ is induced that oscillates at frequency ω'. The Raman polarizability $\bar{\boldsymbol{\alpha}}_R = (\mathbf{Q}_R - \mathbf{Q}_R^0) \cdot \left[\frac{\partial}{\partial \mathbf{Q}_R} \bar{\boldsymbol{\alpha}}(\omega)\right]\big|_{\mathbf{Q}_R = \mathbf{Q}_R^0}$ is defined through the Taylor expansion of the static polarizability $\bar{\boldsymbol{\alpha}}$, with the vibrational normal mode coordinate $\mathbf{Q}_R$ oscillating around its equilibrium position $\mathbf{Q}_R^0$ at the vibrational frequency ω_R, establishing the relationship $\omega' = \omega \pm \omega_R$.

Treating the Raman dipole and nanocavity as interacting classical dipoles at positions $\mathbf{x}_d$ and $\mathbf{x}_p$, respectively, with $\mathbf{E}_0(\mathbf{x}_d) \approx \mathbf{E}_0(\mathbf{x}_p) \equiv \mathbf{E}_0$,

$$\mathbf{d}_R = \bar{\boldsymbol{\alpha}}_R \cdot (\mathbf{E}_0 + \bar{\mathbf{G}}_{dp} \cdot \bar{\boldsymbol{\alpha}}_p \cdot \mathbf{E}_0) = \bar{\boldsymbol{\alpha}}_R \cdot \left[\bar{\mathbf{I}} + \bar{\mathbf{M}}_{\mathrm{loc}}(\omega)\right] \cdot \mathbf{E}_0, \tag{3.13}$$

where black$\bar{\mathbf{M}}_{\mathrm{loc}}(\omega) = \bar{\mathbf{G}}_{dp}(\mathbf{x}_d, \mathbf{x}_p, \omega) \cdot \bar{\boldsymbol{\alpha}}_p$ is the local field enhancement tensor at frequency ω determined by the EMLDOS, which enhances (or suppresses) the local field $\mathbf{E}(\mathbf{x}_d) = \bar{\mathbf{G}}_{dp}(\mathbf{x}_d, \mathbf{x}_p, \omega) \cdot \mathbf{p}$ at $\mathbf{x}_d$, and $\mathbf{p}$ is the dipole moment of the laser-driven cavity. Purcell-enhanced emission occurs similarly during the second step, which can be accounted for by considering the total radiated power from the combined Raman-dipole-nanocavity system when sourced by the Raman dipole oscillating at the shifted frequency ω'. Under these conditions, the total dipole moment $\boldsymbol{\mu}_{\mathrm{tot}} = \mathbf{d}_R + \mathbf{p}$ is found

to be

$$\boldsymbol{\mu}_{\text{tot}} = \left[\bar{\mathbf{I}} + \bar{\mathbf{M}}_{\text{loc}}(\omega')\right] \cdot \bar{\boldsymbol{\alpha}}_R \cdot \left[\bar{\mathbf{I}} + \bar{\mathbf{M}}_{\text{loc}}(\omega)\right] \cdot \mathbf{E}_0. \tag{3.14}$$

Comparing the total power scattered in the presence $P_{\text{tot}}^{\text{cav}}$ and absence P_{tot}^{0} of the cavity using the Larmor power expression in Eq. 3.8, it is observed that (i) $P_{\text{tot}}^{\text{cav}} \propto |\mathbf{E}_0|^2$, i.e., the scattered power depends linearly on the incident field intensity, and (ii) the enhancement factor

$$\frac{P_{\text{tot}}^{\text{cav}}}{P_{\text{tot}}^{0}} \sim \frac{|\mathbf{E}(\omega')|^2}{|\mathbf{E}_0(\omega')|^2} \cdot \frac{|\mathbf{E}(\omega)|^2}{|\mathbf{E}_0(\omega)|^2} \sim \frac{|\mathbf{E}(\omega)|^4}{|\mathbf{E}_0(\omega)|^4}, \tag{3.15}$$

recovering the well-established local field enhancement factor with its fourth power dependence upon the local field relative to the applied field when the frequency shift of the emitted light is neglected. It is worth noting that if the Raman and cavity dipoles are allowed to interact self-consistently [87, 90], then the enhancement factor is found to be $P_{\text{tot}}^{\text{cav}}/P_{\text{tot}}^{0} = (1+M_{\text{loc}})^2/(1-M_{\text{loc}}^2)^2$, within a one-dimensional model for simplicity. This result differs from that of the two-step model only by the presence of the denominator, which is responsible for the classical image dipole effect that renormalizes the cavity and molecular frequencies and lifetimes.

Despite the successes of these single molecule phenomenological models, they fail to provide simple descriptions of other important aspects of SERS, such as nonlinear Stokes and anti-Stokes emission under strong driving and correlations amongst molecular vibrations. Beginning in 2015, molecular optomechanical models of SERS were introduced, allowing for dynamic interaction between two parametrically coupled, non-resonant harmonic molecular vibrational and cavity oscillators within the framework of cavity quantum electrodynamics [80, 91]. In analogy with the two-step model introduced earlier, the interaction Hamiltonian is taken to be

$$\begin{aligned}
\hat{H}_{\text{int}} &= -\hat{\mathbf{E}}(\mathbf{x}_d) \cdot \hat{\mathbf{d}}_R \\
&= -\hat{\mathbf{E}}(\mathbf{x}_d) \cdot \frac{1}{2}\left\{ (\hat{\mathbf{Q}}_R - \hat{\mathbf{Q}}_R^0) \cdot \left[\frac{\partial}{\partial \mathbf{Q}_R} \bar{\boldsymbol{\alpha}}(\omega)\right]\Big|_{\mathbf{Q}_R = \mathbf{Q}_R^0} \cdot \hat{\mathbf{E}}(\mathbf{x}_d) \right\} \\
&\approx -g_R\big(\hat{b} + \hat{b}^\dagger\big)\hat{a}^\dagger \hat{a},
\end{aligned} \tag{3.16}$$

where the rotating wave approximation (RWA) has been invoked and the last line involves the introduction of the quantized vibrational coordinate and cavity electric field operators $\hat{\mathbf{Q}}_R - \hat{\mathbf{Q}}_R^0 = \sqrt{\hbar/2m\omega_e}\big(\hat{b}e^{i\phi} + \hat{b}^\dagger e^{-i\phi}\big)$ and $\hat{\mathbf{E}}(\mathbf{x}) = i\sqrt{2\pi\hbar\omega_c/V}\big(\mathbf{f}(\mathbf{x})\hat{a} - \mathbf{f}^*(\mathbf{x})\hat{a}^\dagger\big)$ expressed in terms of the bosonic molecular vibration $\hat{b}$ ($\hat{b}^\dagger$) and cavity $\hat{a}$ ($\hat{a}^\dagger$) lowering (raising) operators, respectively. Together with the additional assumptions that $\mathbf{x}_d$ is positioned at an antinode of the cavity field and is aligned with the local field polarization, the optomechanical coupling is $g_R = \big[\frac{\partial}{\partial \mathbf{Q}_R}\bar{\boldsymbol{\alpha}}(\omega)\big]\big|_{\mathbf{Q}_R=\mathbf{Q}_R^0}\sqrt{\hbar/2m\omega_e}(2\pi\hbar\omega_c/V)$ when $\phi = \pi$ is chosen. In the presence of a coherent continuous-wave laser drive at frequency ω_d, the Hamiltonian in the frame rotating at the drive frequency becomes

$$\hat{H} = \hbar\Delta\hat{a}^\dagger\hat{a} + \hbar\omega_e\hat{b}^\dagger\hat{b} - g_R\big(\hat{b} + \hat{b}^\dagger\big)\hat{a}^\dagger\hat{a} + i\hbar\Omega(\hat{a}^\dagger - \hat{a}), \tag{3.17}$$

in terms of the cavity-drive detuning $\Delta = \omega_c - \omega_d$ where Ω characterizes the strength of driving by the (classical) applied field $E_0(t) = E_0 e^{-i\omega_d t}$. Rotating Wave ApproximationNeglect of the rapidly oscillating interaction picture light-matter coupling terms proportional to $e^{\pm i(\omega_c+\omega_e)t}$. See Section 3.4.1 for additional details.

The molecular optomechanical Hamiltonian is formally equivalent to the well-studied cavity optomechanical Hamiltonian describing a coherently driven Fabry-Pérot cavity with one mirror mounted on a spring (Figure 3.5d) [92]. The dynamics of the open coupled mode system in the presence of incoherent cavity and molecular vibration decay at rates κ and γ_m, respectively, have been investigated using the Langevin [80] as well as master equation [91, 81] approaches. Despite some differences in the expressions for steady-state phonon occupancies, both approaches show that dynamical backaction introduces additional pathways for phonon creation and annihilation characterized by rates Γ_+ and Γ_-, respectively, which can lead to stimulated phonon amplification and cooling. For example, the cavity-mediated phonon creation and annihilation rates from the master equation approach are

$$\Gamma_\pm = \frac{g_0^2|\alpha|^2\kappa}{(\Delta \pm \omega_m)^2 + (\kappa/2)^2}, \tag{3.18}$$

where α is the coherent state amplitude of the driven cavity mode. The steady-state phonon population at temperature T is

$$n_{\mathrm{ss}} = \frac{\gamma_m}{\gamma_m + \Gamma_{\mathrm{opt}}} n_{\mathrm{th}} + \frac{\Gamma_+}{\gamma_m + \Gamma_{\mathrm{opt}}}, \tag{3.19}$$

where $\Gamma_{\mathrm{opt}} = \Gamma_- - \Gamma_+$, and $n_{\mathrm{th}} = [\exp(\hbar\omega_m/k_B T) - 1]^{-1}$ is the thermal phonon occupancy. Inspection of Eq. 3.18 shows that when the laser detuning is such that $\Delta < 0$ ($\Delta > 0$), $\Gamma_{\mathrm{opt}} < 0$ ($\Gamma_{\mathrm{opt}} > 0$) leading to phonon amplification (cooling) as depicted in Figure 3.5e. Vibrational pumping, therefore, arises naturally within the optomechanical model, and leads to the prediction of nonlinear scaling of anti-Stokes SERS with increasing continuous-wave laser excitation, which has been observed in single-molecule SERS measurements within low-temperature picocavities [93]. The model also predicts that with still stronger blue-detuned driving (typically beyond what has been experimentally achievable with cw lasers before the onset of sample damage), $\Gamma_{\mathrm{opt}} = -\gamma_m$, which causes the phonon population in Eq. (3.19) to diverge and the onset of phonon lasing, which is known as parametric instability. Figure 3.6 presents examples from the recent literature that report signatures of collective phenomena in SERS predicted by the optomechanical model [94, 95, 96], which are more fully discussed in the Supplemental Material.

3.4 Strongly Coupled Systems

Just as strong contact of an environment with a physical system is a defining feature of weak coupling, environmental isolation is the hallmark of physical systems in the *strong coupling regime.* Here, the rate of energy transfer (g) between system components is so large relative to environmental loss (γ) of any form that outcoupling to the environment can be largely neglected. Strongly coupled systems are characterized by repeated and coherent intrasystem energy transfer and are thus described accurately by Hermitian Hamiltonians and unitary time evolution. In the absence of external forces, normal modes (or super modes or molecular orbitals depending upon

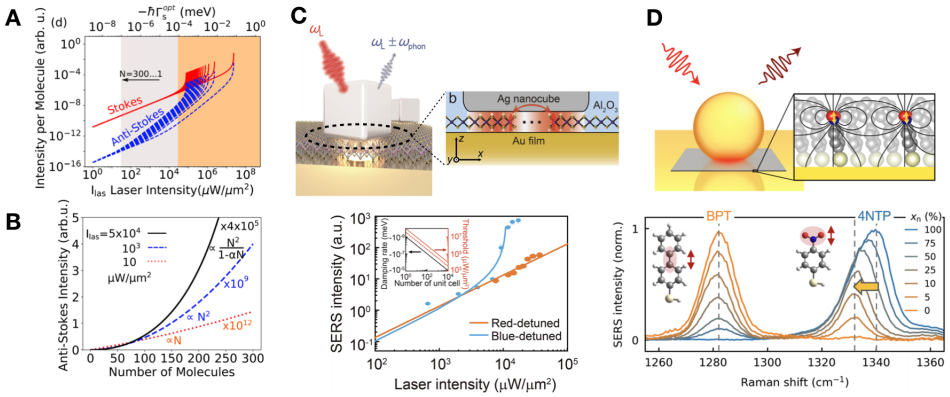

Figure 3.6: Collective optomechanical effects in SERS. (a) Calculated Stokes and anti-Stokes emission intensities as a function of laser intensity and the number of identical molecules N coupled to the cavity under blue-detuned cw laser drive. (b) Anti-Stokes scattering intensity as a function of N exhibiting quadratic dependence in the vibrational pumping regime (shaded gray in panel (a)). (c) Measured super-linear Stokes scattered power dependence from monolayer MoS_2 placed within the gap regions of nanocube-on-mirror structures under blue-detuned drive. (d) Intermolecular vibrational coupling between polar bonds analyte molecules (4NTP) embedded within self-assembled monolayers composed of inert spacer molecules (BPT) leads to a measurable frequency shift detectable in SERS. Panels (a), (b), (c) and (d) reprinted with permission from [94], [94], [95] and [96]; Copyright (2020), (2020), (2022) and (2022), respectively, American Chemical Society.

the parlance of the particular research community) arise as the natural, independent (i.e., noninteracting) basis in which all driven states of the system including spectra can be decomposed.

Normal modes can vary considerably in their character ranging from weakly mixed forms that closely resemble the uncoupled system components to maximally mixed, even-weighted superpositions of the original uncoupled system components. In the case of two coordinate-coordinate (q_1q_2) coupled oscillators with Hamiltonian [97]

$$H = \frac{p_1^2}{2m_1} + \frac{1}{2}m_1\omega_1^2 q_1^2 + \frac{p_1^2}{2m_1} + \frac{1}{2}m_2\omega_2^2 q_2^2 - g_{qq}(\mathbf{s})q_1q_2, \tag{3.20}$$

the general forms of its normal mode coordinates and frequencies are

$$\begin{aligned} q_- &= q_1\left(\frac{m_1}{m_2}\right)^{1/4}\cos\theta + q_2\left(\frac{m_2}{m_1}\right)^{1/4}\sin\theta \\ q_+ &= -q_1\left(\frac{m_1}{m_2}\right)^{1/4}\sin\theta + q_2\left(\frac{m_2}{m_1}\right)^{1/4}\cos\theta \end{aligned} \tag{3.21}$$

$$\begin{aligned} \omega_- &= \sqrt{\omega_1^2\cos^2\theta + \omega_2^2\sin^2\theta - \frac{2g_{qq}}{\sqrt{m_1m_2}}\sin\theta\cos\theta} \\ \omega_+ &= \sqrt{\omega_1^2\sin^2\theta + \omega_2^2\cos^2\theta + \frac{2g_{qq}}{\sqrt{m_1m_2}}\sin\theta\cos\theta} \end{aligned} \tag{3.22}$$

written in terms of the angle $\theta = (1/2)\tan^{-1} 2g_{qq}/\sqrt{m_1m_2}(\omega_2^2 - \omega_1^2)$ dictating the degree of mode mixing experienced between the coupled coordinates q_1 and q_2. At zero detuning, the energetic splitting between the normal modes is $\hbar\sqrt{2g/\sqrt{m_1m_2}}$. Such equations might, e.g., describe two coupled plasmonic nanoparticles with dipolar coordinates $\mathbf{d}_1 = -e\hat{\mathbf{q}}_1 q_1$ and $\mathbf{d}_2 = -e\hat{\mathbf{q}}_2 q_2$, and coupling strength $g_{qq}(\mathbf{s}) = e^2\hat{\mathbf{q}}_1 \cdot \mathbf{G}(\mathbf{s}) \cdot \hat{\mathbf{q}}_2$ derived from the interaction energy $H_{\text{int}} = -\mathbf{E}_1(\mathbf{s}) \cdot \mathbf{d}_2 = -\mathbf{d}_1 \cdot \mathbf{E}_2(-\mathbf{s}) = -\mathbf{d}_1 \cdot \mathbf{G}(\mathbf{s}) \cdot \mathbf{d}_2 = -g_{qq}(\mathbf{s})q_1q_2$, where

$$\mathbf{G}(\mathbf{s}) = \Big[(3\hat{\mathbf{s}}\hat{\mathbf{s}} - 1)\Big(\frac{1}{s^3} - \frac{ik}{s^2}\Big) - (\hat{\mathbf{s}}\hat{\mathbf{s}} - 1)\frac{k^2}{s}\Big]e^{iks} \tag{3.23}$$

is the free-space dipole relay tensor [50] with $k = \omega/c$ relaying the electric field $\mathbf{E}(\mathbf{s}) = \mathbf{G}(\mathbf{s}) \cdot \mathbf{d}$ produced by one dipole to the other located at the position $\mathbf{s} = \hat{\mathbf{s}}s$

away. The effective mass m_i of each plasmonic dipole mode ($i = 1, 2$) [98, 99] can be derived from the Clausius-Mossotti polarizability together with a Drude model of the nanoparticle's bulk free carrier response. This dipolar coupling scheme as well as other more sophisticated couplings can all be derived from the exact minimal coupling formalism [100].

Other strongly coupled light-matter and light-light systems are governed by similar Hamiltonians with a few replacements. For massless light modes, such as the optical eigenmodes of nanophotonic cavities, the effective mass m is replaced by the inverse mode volume V. Additionally, the form of the interaction energy changes to coordinate-momentum ($q_1 p_2$) coupling for interacting light-matter [29, 31, 51, 52] systems and to doubly coupled coordinate-coordinate ($q_1 q_2$) and momentum-momentum ($p_1 p_2$) couplings for interacting light-light [101, 102] systems.

PolaritonsThe emergent collective excitations of strongly coupled light-matter degrees of freedom. Interacting light-matter Hamiltonians arise, e.g., in the description of high quality (Q) nanophotonic cavity coupled atomic, molecular, excitonic, or plasmonic degrees of freedom blended into new hybrid states called *polaritons*. In general, polaritons are the collective excitations that emerge in the hybridization of optical and material degrees of freedom and can be engineered to vary in their degree of mode mixing in analogy to Eq. (3.21) by exerting control over parameters such as detuning and coupling strength. Given the light-matter interaction energy $H_{\text{int}} = -\mathbf{E}(\mathbf{s}) \cdot \mathbf{d}$ with cavity electric field $\mathbf{E} = -\dot{\mathbf{A}}/c$ and cavity magnetic field $\mathbf{B} = \nabla \times \mathbf{A}$, the light-matter Hamiltonian becomes [31]

$$\begin{aligned} H &= \int \frac{\mathbf{E}^2 + \mathbf{B}^2}{8\pi} d^3x + \frac{p_e^2}{2m} + \frac{1}{2} m\omega_e^2 q_e^2 - \mathbf{E}(\mathbf{s}) \cdot \mathbf{d} \\ &= \frac{V p_c^2}{2} + \frac{1}{2V} \omega_c^2 q_c^2 + \frac{p_e^2}{2m} + \frac{1}{2} m\omega_e^2 q_e^2 - \sqrt{mV}\, g_{pq}(\mathbf{s}) p_c q_e \end{aligned} \tag{3.24}$$

in the case of one nanophotonic cavity mode $\mathbf{A}(\mathbf{x}, t) = (\sqrt{4\pi}c/V)\mathbf{f}(\mathbf{x})q_c(t)$ of frequency ω_c, volume V, spatial mode profile $\mathbf{f}(\mathbf{x})$, and dynamical coordinates (p_c, q_c) strongly coupled to one material emitter oscillator of frequency ω_e, effective mass

m, and dynamical coordinates (p_e, q_e) with strength $g_{pq}(\mathbf{s}) = -e\sqrt{4\pi/mV}\mathbf{f}(\mathbf{s}) \cdot \hat{\mathbf{q}}_e$. Note that the Newton equations in Eq. (3.1) describing a weakly coupled emitter-cavity system are also derivable from Eq. (3.24), but must be supplemented with phenomenological velocity-dependent frictional forces to account for the effects of radiative and nonradiative damping. It is also interesting to note that the inverse cavity mode volume V inherits the analogous role of an effective mass, but of the nanophotonic cavity. In the strong coupling regime where environmetnal losses can be neglected, the above Hamiltonian (Eq. (3.24)), when quantized in the canonical manner such that $[\hat{q}_c, \hat{p}_c] = i\hbar$ and $[\hat{q}_e, \hat{p}_e] = i\hbar$ [100], serves as the starting point for a hierarchy of quantum optical Hamiltonians including the celebrated Jaynes-Cummings and Tavis-Cummings models described below.

3.4.1 Jaynes-Cummings Model

The Jaynes-Cummings (JC) model [103] describes the interaction between a two-level system (TLS) and a single optical cavity mode. It derives from quantization of the light-matter Hamiltonian in Eq. (3.24) together with replacement of the bosonic description of the matter with that of a TLS representing the ground $|g\rangle$ and excited state $|e\rangle$ of an emitter. By defining the dipole and electric field operators as $\hat{\mathbf{d}} = \hat{\mathbf{d}}^{(+)} + \hat{\mathbf{d}}^{(-)}$ and $\hat{\mathbf{E}} = \hat{\mathbf{E}}^{(+)} + \hat{\mathbf{E}}^{(-)}$, where $\hat{\mathbf{d}}^{(+)} = |e\rangle\langle e|\hat{\mathbf{d}}|g\rangle\langle g| = |e\rangle\mathbf{d}_{eg}\langle g|$, $\hat{\mathbf{E}}^{(+)}(\mathbf{x}) = i\sqrt{2\pi\hbar\omega_c/V}\mathbf{f}(\mathbf{x})\hat{a}e^{-i\phi}$, and $\hat{\mathbf{d}}^{(-)} = [\hat{\mathbf{d}}^{(+)}]^\dagger$ and $\hat{\mathbf{E}}^{(-)} = [\hat{\mathbf{E}}^{(+)}]^\dagger$, the light-matter Hamiltonian becomes

$$\begin{aligned}\hat{H} &= \hbar\omega_c\hat{a}^\dagger\hat{a} + \hbar\omega_e\hat{\sigma}_+\hat{\sigma}_- - \hat{\mathbf{E}}(\mathbf{s}) \cdot \hat{\mathbf{d}} \\ &= \hbar\omega_c\hat{a}^\dagger\hat{a} + \hbar\omega_e\hat{\sigma}_+\hat{\sigma}_- + \underbrace{\Big[- \hat{\mathbf{E}}^{(+)}(\mathbf{s}) \cdot \hat{\mathbf{d}}^{(+)} - \hat{\mathbf{E}}^{(-)}(\mathbf{s}) \cdot \hat{\mathbf{d}}^{(-)} \Big]}_{\hat{H}_{\text{int}}^{(\text{res})}} + \underbrace{\Big[- \hat{\mathbf{E}}^{(+)}(\mathbf{s}) \cdot \hat{\mathbf{d}}^{(-)} - \hat{\mathbf{E}}^{(-)}(\mathbf{s}) \cdot \hat{\mathbf{d}}^{(+)} \Big]}_{\hat{H}_{\text{int}}^{(\text{antires})}}\end{aligned} \tag{3.25}$$

in terms of the TLS excitation and de-excitation operators $\hat{\sigma}_+ = |e\rangle\langle g|$ and $\hat{\sigma}_- = |g\rangle\langle e|$. Expressed in the interaction picture, the antiresonant and resonant interactions

$$\begin{aligned}
\hat{H}_{\text{int}}^{(\text{res})}(t) &= -\hat{\mathbf{E}}^{(+)}(\mathbf{s}) \cdot \mathbf{d}_{eg}\hat{\sigma}_+ - \hat{\mathbf{E}}^{(-)}(\mathbf{s}) \cdot \mathbf{d}_{ge}\hat{\sigma}_- \\
&= -i\hbar \underbrace{\left[\sqrt{\frac{2\pi\hbar\omega_c}{V}}\frac{\mathbf{f}(\mathbf{s}) \cdot \mathbf{d}_{eg}}{\hbar}\right]}_{g} e^{-i(\omega_c-\omega_e)t}\hat{a}e^{-i\phi}\hat{\sigma}_+ + \text{H.c.} \\
\hat{H}_{\text{int}}^{(\text{antires})}(t) &= -\hat{\mathbf{E}}^{(+)}(\mathbf{s}) \cdot \mathbf{d}_{ge}\hat{\sigma}_- - \hat{\mathbf{E}}^{(-)}(\mathbf{s}) \cdot \mathbf{d}_{eg}\hat{\sigma}_+ \\
&= -i\hbar \underbrace{\left[\sqrt{\frac{2\pi\hbar\omega_c}{V}}\frac{\mathbf{f}(\mathbf{s}) \cdot \mathbf{d}_{ge}}{\hbar}\right]}_{\bar{g}} e^{-i(\omega_c+\omega_e)t}\hat{a}e^{-i\phi}\hat{\sigma}_- + \text{H.c.}
\end{aligned} \tag{3.26}$$

are characterized by phase factors $e^{-i(\omega_c-\omega_e)t}$ and $e^{-i(\omega_c+\omega_e)t}$ with the former (energy conserving) phase oscillating slowly while the latter (non-energy conserving) phase oscillates rapidly when the cavity-emitter detuning $\delta = \omega_c - \omega_e$ is small (using the convention that $\omega_g = 0$). Under the RWA the latter is neglected completely, resulting in the JC Hamiltonian

$$\hat{H}_{\text{JC}} = \hbar\omega_c\hat{a}^\dagger\hat{a} + \hbar\omega_e\hat{\sigma}_+\hat{\sigma}_- + \hbar g\hat{a}\hat{\sigma}_+ + \hbar g^*\hat{a}^\dagger\hat{\sigma}_- \tag{3.27}$$

in the Schrödinger picture, after choosing the arbitrary phase angle $\phi = -\pi/2$. Due to the TLS's limited state space of ground ($|g\rangle$) and excited ($|e\rangle$), only $|g, n\rangle$ and $|e, n-1\rangle$ states become coupled through $\hat{H}_{\text{int}}^{(\text{res})}$ and the Fock state representation of the JC Hamiltonian decomposes into 2×2 subspaces with n total excitations

$$\hat{H}_{\text{JC},n} = (n+1)\hbar\omega_c \begin{bmatrix} 1 & 0 \\ 0 & 1 \end{bmatrix} + \hbar \begin{bmatrix} 0 & g^*\sqrt{n} \\ g\sqrt{n} & -\delta \end{bmatrix}, \tag{3.28}$$

expressed in terms of the cavity-emitter detuning δ. The energy levels and eigenstates within the nth manifold are

$$E_{n\pm} = n\hbar\omega_c - \frac{\hbar\delta}{2} \pm \frac{\hbar}{2}\sqrt{\delta^2 + 4|g|^2 n}, \tag{3.29}$$

$$\begin{aligned}
|+, n\rangle &= \cos\theta_n|e, n-1\rangle + \sin\theta_n|g, n\rangle \\
|-, n\rangle &= -\sin\theta_n|e, n-1\rangle + \cos\theta_n|g, n\rangle
\end{aligned} \tag{3.30}$$

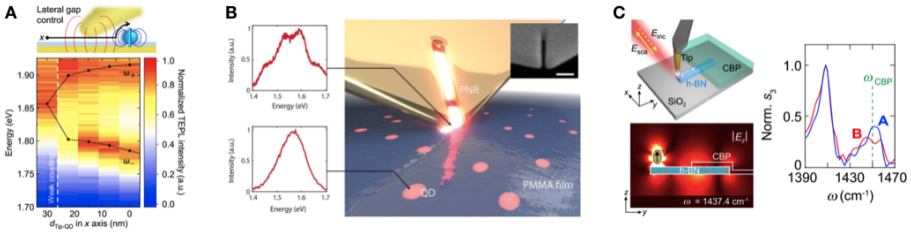

Figure 3.7: Probing strongly-coupled systems with tip-enhanced measurements. (a) Reversible and dynamical interrogation of single CdSe/ZnS QDs in the strong coupling regime using TEPL spectroscopy. (b) Deterministic room temperature strong coupling of individual colloidal QDs to a plasmonic notch resonator at the tip of a scanning probe measured using TEPL. (c) Nano-FTIR scheme, calculated spatial map of the model system response field, and measured amplitude spectra of the bare (blue) and molecule-covered (red) nanobeam. Upper and lower polaritons were observed in the amplitude spectra $S_3(\omega)$ of the combined system at frequencies above and below the uncoupled molecular vibration frequency ω_{CBP}. Panels (a) and (b) are adapted with permission from [104] and [105]; Copyright (2019) and (2018), respectively, Science. Panel (c) reprinted with permission from [106]; Copyright (2022) Springer Nature.

with coupling angle $\theta_n = (1/2)\tan^{-1} 2\sqrt{n}|g|/(\omega_e - \omega_c)$ and splitting $E_{n+} - E_{n-} = \sqrt{n}\hbar\Omega$ at zero detuning defining the Rabi frequency $\Omega = 2|g| = 2\sqrt{2\pi\hbar\omega_c/V}|\mathbf{f}(\mathbf{s}) \cdot \mathbf{d}_{eg}|/\hbar = 2|\mathbf{E}^{(+)}(\mathbf{s}) \cdot \mathbf{d}_{eg}|/\hbar$. See the Supplemental Material for an expanded discussion of the JC model, as well as its generalization to N identical TLSs (the Tavis-Cummings model) and the inclusion of losses.

3.4.2 Characterizing Strongly Coupled Systems – Near-Field Probes

Many characteristics of strongly coupled systems have been studied with a broad range of molecular and solid state emitters coupled to a variety of nanophotonic cavities [107, 108, 109]. In particular, far-field optical spectroscopies have repeatedly verified the utility of Eq. 3.29 (and its non-Hermitian analog) in describing the evolution of upper and lower polariton energies as system parameters are varied to tune the uncoupled mode energies, as well as the $\sqrt{N}$ dependence of the Rabi splitting on

the number of emitters coupled to the cavity (Supplemental Material). An appreciation was also developed regarding the role played by the measurement observables in the determination of system parameters. For example, it was shown that Rabi splittings inferred from scattering measurements can be over-estimated, and that it is, therefore, preferable to employ absorption or photoluminescence measurements to determine Rabi splitting energies [110, 111]. Albeit in the weak coupling regime, Refs. [31, 30] independently came to the same conclusion in the quantification of Fano antiresonances in both optical and electron beam spectroscopies. Recent examples of TEPL measurements employing movable metallic tips to controllably and dynamically interrogate strong coupling to emitters are presented in Figure 3.7, with additional discussion provided in the Supplemental Material.

3.4.3 Free Electron Probes

In addition to the optical spectroscopies discussed thus far, free-electron-based measurements in scanning transmission electron microscopes (STEMs) have also demonstrated unique access into the properties of nanophotonic structures and their detailed optical responses. Specifically, EEL spectroscopy, where the excitation spectrum of an interrogated sample is encoded in the difference in kinetic energy of a probing free electron before and after interaction, has been used for over a decade to spatially and spectrally map excitations of plasmonic [117, 99] as well as nanophotonic [118, 76] systems. Due to recent progress in monochromation and aberration correction technologies, 10 meV energy resolution is achievable in modern STEMs, opening the door to performing high-resolution spectroscopy of visible to far-infrared frequency excitations with spatial resolution (1 nm) far below the optical diffraction limit [118, 119, 120]. The Supplemental Material contains an expanded discussion of recent studies leveraging EEL spectroscopy and related techniques to probe strongly coupled nanophotonic systems, which are highlighted in Figure 3.8.

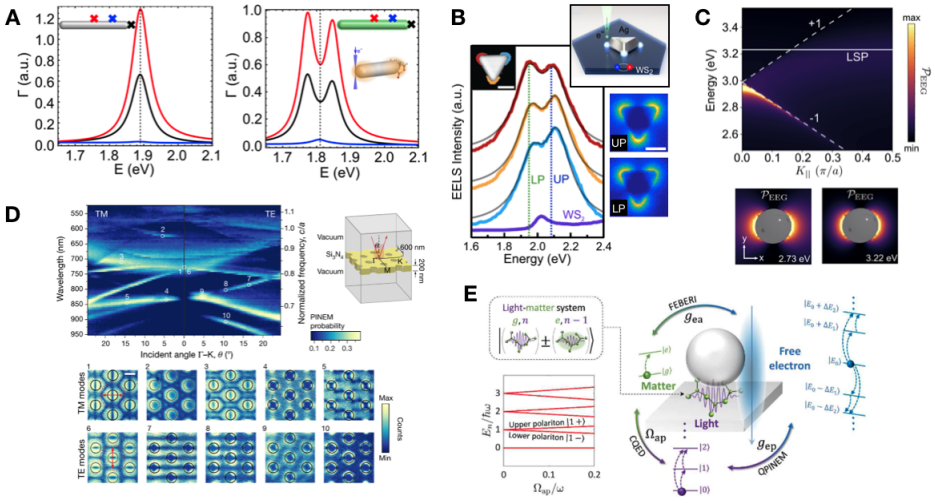

Figure 3.8: Probing strong coupling with free electrons. (a) Calculated EEL spectra of a bare Ag rod (left) and an Ag rod coated by an emitter medium shell (right) for various electron beam positions marked by color-coded crosses. (b) Experimental spectral and spatial mapping of upper and lower polaritons using EEL spectroscopy for an Ag nanoprism coupled to WS_2 excitons at room temperature. (c) Calculated EEG spectra of a one-dimensional plasmonic array structure as a function of the incident CW laser in-plane momentum $K_{\parallel}$, which encodes the array energy-momentum dispersion $E(k_{\parallel})$. Spatially-resolved spectrum image calculations are presented at the upper and lower polariton energies for the same array structure embedded within a homogeneous slab of emitters. (d) Experimental measurement of Bloch mode $E(\mathbf{k}_{\parallel})$ dispersion in a photonic crystal (top) using free electrons. Images below show direct spectral mapping of Bloch modes in real space. (e) Coherent free electron probing of laser-stimulated light-matter targets in the strong coupling regime. Panels (a) and (b) are adapted with permission from [112] and [113]; Copyright (2018) and (2019), respectively, American Chemical Society. Panel (c) reprinted with permission from [114]; Copyright (2022) by the American Physical Society. Panel (d) reprinted with permission from [115]; Copyright (2020) Springer Nature. Panel (e) reprinted with permission from [116]; Copyright (2023) Science.

3.4.4 Ultrastrong Coupling Regime

Distinctly new behavior arises when the light-matter coupling rate (g) and bare excitation frequency (ω_e) become comparable. In such situations, the system is said to be in the *ultrastrong coupling* (USC) regime [125, 126], and JC description of the interaction between a single cavity mode of frequency ω_c and a single TLS of excitation frequency ω_e must be replaced by the quantum Rabi (QR) model Hamiltonian

$$\hat{H}_{\mathrm{QRM}} = \hbar\omega_c\hat{a}^\dagger\hat{a} + \hbar\omega_e\hat{\sigma}_+\hat{\sigma}_- + \underbrace{\hbar g\hat{a}\hat{\sigma}_+ + \hbar g^*\hat{a}^\dagger\hat{\sigma}_-}_{\text{resonant}} + \underbrace{\hbar\bar{g}\hat{a}\hat{\sigma}_- + \hbar\bar{g}^*\hat{a}^\dagger\hat{\sigma}_+}_{\text{antiresonant}}. \tag{3.31}$$

This Hamiltonian derives directly from Eqs. 3.25 and 3.26, differing from the JC Hamiltonian only in that the anti-resonant terms neglected within the RWA are retained within the QR model. As displayed in Figure 3.9(a), the RWA underlying the evaluation of the JC model eigenvalues (red) fails to accurately replicate the QR model eigenvalues (black) in the USC regime [121, 122]. The Supplemental Material contains an expanded discussion of USC, including the modification of the ground state composition and recent studies involving nanophotonic systems (Figure 3.9).

3.5 Summary and Future Outlook

Over half a century since the influential experiments of Purcell and Drexhage, researchers today have achieved exquisite ability to tailor the interactions between light and matter through precision engineering of nanophotonic cavities capable of confining light to the nanoscopic dimensions of molecular, excitonic, phononic, and plasmonic excitations. Through weak coupling to nanophotonic cavities, exceedingly fragile optical processes have been enhanced to the point where the spectra of individual quantum objects can be resolved and investigated at room temperature with new levels of control, heralding separate renaissances in multiple fields of spectroscopy. In other contexts, entirely new states of emergent polaritonic matter have been coaxed into existence and manipulated, sometimes actively, to realize novel strongly-coupled

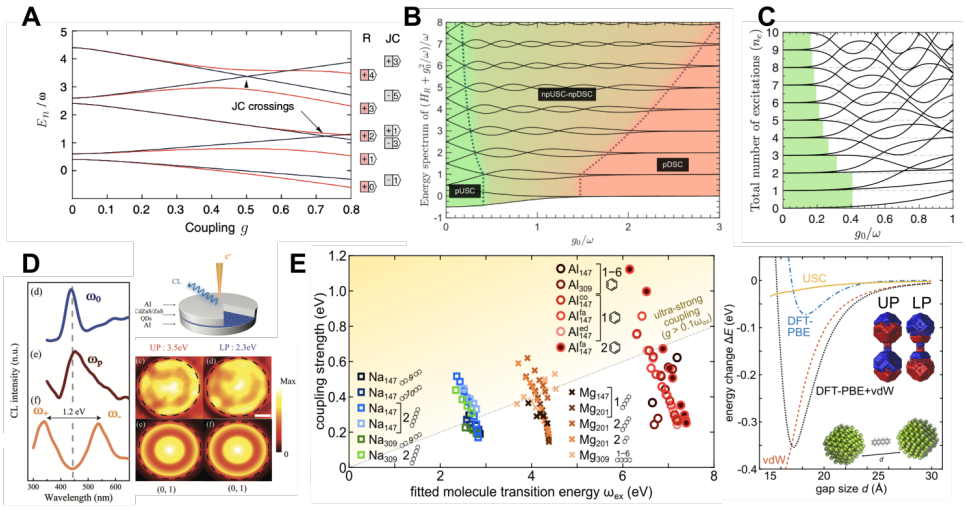

Figure 3.9: Ultrastrong coupling. (a) Comparison of JC model (black) and QR model (red) eigenenergies as a function of coupling strength. (b) QR model eigenenergies in the USC regime, which is subdivided into perturbative USC (green), nonperturbative USC to nonperturbative deep strong coupling (tan), and perturbative deep strong coupling (red). (c) Total number of excitations in each QR eigenstate as a function of coupling strength within the pUSC and npUSC regimes. (d) Measured CL spectra of metal-insulator-metal cavities filled with CdZnS/ZnS QD, which exhibit Rabi splittings indicative of USC. (e) TDDFT calculations indicate that certain types of single organic molecules coupled to plasmonic dimers can reach the USC regime. The plot on the right depicts the calculated ground state energy shift arising from virtual photon excitations. Reprinted Panels (a), (b) and (c) with permission from [121], [122] and [122]; Copyright (2011), (2016) and (2016) respectively, by the American Physical Society. Panel (e) adapted with permission from [123]; Copyright (2022) American Chemical Society. Panel (d) adapted with permission from [124]; Copyright (2020) Royal Society of Chemistry.

optical phenomena that serve as playgrounds for exploration of quantum many-body physics.

In both weak and strong coupling regimes, not only have far-field optical measurements been employed to characterize nanoscale material responses, but so too have more sophisticated near-field optical and electron beam probes capable of simultaneously recording spectra and correlated images with spatial resolution below the diffraction limit of light. Owing to their ability of measuring nanoscale optical processes at their native energy, length, momentum, time, and polarization scales, such near-field spectroscopies—or *nanospectroscopies*—represent some of the most information-rich observables available today and, looking forward, we anticipate numerous future directions of inquiry that will benefit from the new limits of resolution that they offer.

Alongside the nanospectroscopic measurements highlighted in this review comes the companion need for detailed theoretical modeling of the specific experimental observables being measured, as the observed spectra (and microscope images) often do not directly map to those of the isolated material excitation as is commonly assumed in many other molecular spectroscopies. This difference is due to the significance of interactions and losses shared between nanoscale material excitations and their local optical cavity environments as well as the convolution of experimental signals by the specific response functions of the probes themselves. Said differently, the Hamiltonian eigenspectrum of the isolated material response is often a poor representation of the observed spectrum and significant theoretical work is required to connect the two.

With these advances in cavity and emitter synthesis/fabrication, near- and far-field materials characterization, and theory, now is an exciting time for spectroscopists investigating the optical properties individual, few, and ensembles of emitters coupled to nanophotonic cavity environments. Going forward, the future holds great promise for detailed exploration of cavity-enhanced optical processes at the nanoscale across varying interaction strengths and their associated physical regimes, opening new vis-

tas in basic scientific research and the downstream technological applications that it enables.

BIBLIOGRAPHY

[1] Lord Rayleigh. The problem of the whispering gallery. *The London, Edinburgh, and Dublin Philosophical Magazine and Journal of Science*, 20(120):1001–1004, 1910.

[2] W. Howard Wise. Asymptotic dipole radiation formulas. *The Bell System Technical Journal*, 8(4):662–671, 1929.

[3] R. A. Shelby, D. R. Smith, and S. Schultz. Experimental verification of a negative index of refraction. *Science*, 292(5514):77–79, 2001.

[4] J. B. Pendry, D. Schurig, and D. R. Smith. Controlling electromagnetic fields. *Science*, 312(5781):1780–1782, 2006.

[5] M.F. Crommie, C.P. Lutz, D.M. Eigler, and E.J. Heller. Quantum corrals. *Physica D*, 83(1):98–108, 1995.

[6] Eric J. Heller. Bound-state eigenfunctions of classically chaotic hamiltonian systems: Scars of periodic orbits. *Phys. Rev. Lett.*, 53:1515–1518, Oct 1984.

[7] K. H. Drexhage. *Habilitationsschrift.* habilitation, Marburg, 1966.

[8] K.H. Drexhage. Influence of a dielectric interface on fluorescence decay time. *J. Lumin.*, 1-2:693–701, 1970.

[9] Hans Kuhn. Classical aspects of energy transfer in molecular systems. *J. Chem. Phys.*, 53(1):101–108, 09 2003.

[10] R. R. Chance, A. Prock, and R. Silbey. *Molecular Fluorescence and Energy Transfer Near Interfaces*, pages 1–65. John Wiley & Sons, Ltd, 1978.

[11] E. M. Purcell. Spontaneous emission probabilities at radio frequencies. *Phys. Rev.*, 69:674, Jun 1946.

[12] Rufus H Ritchie. Plasma losses by fast electrons in thin films. *Physical Review*, 106(5):874, 1957.

[13] David Bohm and David Pines. A collective description of electron interactions: III. Coulomb interactions in a degenerate electron gas. *Physical Review*, 92(3):609, 1953.

[14] Kerry J. Vahala. Optical microcavities. *Nature*, 424(6950):839–846, Aug 2003.

[15] Pan Wang, Yipei Wang, Zongyin Yang, Xin Guo, Xing Lin, Xiao-Chong Yu, Yun-Feng Xiao, Wei Fang, Lei Zhang, Guowei Lu, et al. Single-band 2-nm-line-width plasmon resonance in a strongly coupled Au nanorod. *Nano Letters*, 15(11):7581–7586, 2015.

[16] Yueying Wu, Zhongwei Hu, Xiang-Tian Kong, Juan Carlos Idrobo, Austin G Nixon, Philip D Rack, David J Masiello, and Jon P Camden. Infrared plasmonics: STEM-EELS characterization of Fabry-Pérot resonance damping in gold nanowires. *Physical Review B*, 101(8):085409, 2020.

[17] Paul E Barclay, Charles Santori, Kai-Mei Fu, Raymond G Beausoleil, and Oskar Painter. Coherent interference effects in a nano-assembled diamond nv center cavity-qed system. *Optics Express*, 17(10):8081–8197, 2009.

[18] Dominik Rattenbacher, Alexey Shkarin, Jan Renger, Tobias Utikal, Stephan Götzinger, and Vahid Sandoghdar. Coherent coupling of single molecules to on-chip ring resonators. *New Journal of Physics*, 21(6):062002, 2019.

[19] Scott A Diddams, Kerry Vahala, and Thomas Udem. Optical frequency combs: Coherently uniting the electromagnetic spectrum. *Science*, 369(6501):eaay3676, 2020.

[20] Abraham Nitzan. *Chemical Dynamics in Condensed Phases*. Oxford Univ. Press, 2006.

[21] Cristian L Cortes, Matthew Otten, and Stephen K Gray. Non-Hermitian approach for quantum plasmonics. *J. Chem. Phys.*, 152(8):084105, 2020.

[22] Lukas Novotny and Bert Hecht. *Principles of Nano-Optics Second Edition*. Cambridge Univ. Press, 2012.

[23] Pascal Anger, Palash Bharadwaj, and Lukas Novotny. Enhancement and quenching of single-molecule fluorescence. *Phys. Rev. Lett.*, 96(11):113002, 2006.

[24] Keiko Munechika, Yeechi Chen, Andreas F. Tillack, Abhishek P. Kulkarni, Ilan Jen-La Plante, Andrea M. Munro, and David. S. Ginger. Quantum dot/plasmonic nanoparticle metachromophores with quantum yields that vary with excitation wavelength. *Nano Lett.*, 11(7):2725–2730, 2011.

[25] Mohamed ElKabbash, Ermanno Miele, Ahmad K. Fumani, Michael S. Wolf, Angelo Bozzola, Elisha Haber, Tigran V. Shahbazyan, Jesse Berezovsky, Francesco De Angelis, and Giuseppe Strangi. Cooperative energy transfer controls the spontaneous emission rate beyond field enhancement limits. *Phys. Rev. Lett.*, 122:203901, May 2019.

[26] Tigran V. Shahbazyan. Local density of states for nanoplasmonics. *Phys. Rev. Lett.*, 117:207401, Nov 2016.

[27] Tigran V Shahbazyan. Spontaneous decay of a quantum emitter near a plasmonic nanostructure. *Phys. Rev. B*, 98(11):115401, 2018.

[28] Nicholas W Bigelow, Alex Vaschillo, Jon P Camden, and David J Masiello. Signatures of Fano interferences in the electron energy loss spectroscopy and cathodoluminescence of symmetry-broken nanorod dimers. *ACS Nano*, 7(5):4511–4519, 2013.

[29] Niket Thakkar, Morgan T Rea, Kevin C Smith, Kevin D Heylman, Steven C Quillin, Kassandra A Knapper, Erik H Horak, David J Masiello, and Randall H Goldsmith. Sculpting Fano resonances to control photonic–plasmonic hybridization. *Nano Lett.*, 17(11):6927–6934, 2017.

[30] Kevin C Smith, Agust Olafsson, Xuan Hu, Steven C Quillin, Juan Carlos Idrobo, Robyn Collette, Philip D Rack, Jon P Camden, and David J Masiello. Direct observation of infrared plasmonic Fano antiresonances by a nanoscale electron probe. *Phys. Rev. Lett.*, 123(17):177401, 2019.

[31] Feng Pan, Kevin C Smith, Hoang L Nguyen, Kassandra A Knapper, David J Masiello, and Randall H Goldsmith. Elucidating energy pathways through simultaneous measurement of absorption and transmission in a coupled plasmonic-photonic cavity. *Nano Lett.*, 20(1):50–58, 2019.

[32] Boris Luk'Yanchuk, Nikolay I Zheludev, Stefan A Maier, Naomi J Halas, Peter Nordlander, Harald Giessen, and Chong Tow Chong. The Fano resonance in plasmonic nanostructures and metamaterials. *Nat. Mater.*, 9(9):707–715, 2010.

[33] Sassan N. Sheikholeslami, Aitzol García-Etxarri, and Jennifer A. Dionne. Controlling the interplay of electric and magnetic modes via Fano-like plasmon resonances. *Nano Lett.*, 11(9):3927–3934, 2011.

[34] Sean M. Collins, Olivia Nicoletti, David Rossouw, Tomas Ostasevicius, and Paul A. Midgley. Excitation dependent Fano-like interference effects in plasmonic silver nanorods. *Phys. Rev. B*, 90:155419, Oct 2014.

[35] U. Fano. Effects of configuration interaction on intensities and phase shifts. *Phys. Rev.*, 124:1866–1878, Dec 1961.

[36] E. Lassettre, M. Krasnow, and S. Silverman. Inelastic scattering of electrons by helium. *J. Chem. Phys.*, 40:1242–1248, Dec 1964.

[37] E. N. Lassettre. Collision cross-section studies on molecular gases and the dissociation of oxygen and water. *Radiat. Res. Suppl.*, 1:530–546, Dec 1959.

[38] Jon A. Dieringer, Kristin L. Wustholz, David J. Masiello, Jon P. Camden, Samuel L. Kleinman, George C. Schatz, and Richard P. Van Duyne. Surface-enhanced Raman excitation spectroscopy of a single rhodamine 6G molecule. *J. Am. Chem. Soc.*, 131(2):849–854, 2009.

[39] Jon P. Camden, Jon A. Dieringer, Yingmin Wang, David J. Masiello, Lawrence D. Marks, George C. Schatz, and Richard P. Van Duyne. Probing the structure of single-molecule surface-enhanced Raman scattering hot spots. *J. Am. Chem. Soc.*, 130(38):12616–12617, 2008.

[40] David L Jeanmaire and Richard P Van Duyne. Surface Raman spectroelectrochemistry: Part i. heterocyclic, aromatic, and aliphatic amines adsorbed on the anodized silver electrode. *J. Electroanal. Chem.*, 84(1):1–20, 1977.

[41] Shuming Nie and Steven R Emory. Probing single molecules and single nanoparticles by surface-enhanced Raman scattering. *Science*, 275(5303):1102–1106, 1997.

[42] Katrin Kneipp, Yang Wang, Harald Kneipp, Lev T Perelman, Irving Itzkan, Ramachandra R Dasari, and Michael S Feld. Single molecule detection using surface-enhanced Raman scattering (SERS). *Phys. Rev. Lett.*, 78(9):1667, 1997.

[43] P. T. Leung, S. Y. Liu, and K. Young. Completeness and orthogonality of quasinormal modes in leaky optical cavities. *Phys. Rev. A*, 49:3057–3067, Apr 1994.

[44] Jean-Michel Gérard. *Solid-State Cavity-Quantum Electrodynamics with Self-Assembled Quantum Dots*, pages 269–314. Springer Berlin Heidelberg, Berlin, Heidelberg, 2003.

[45] C. Sauvan, J. P. Hugonin, I. S. Maksymov, and P. Lalanne. Theory of the spontaneous optical emission of nanosize photonic and plasmon resonators. *Phys. Rev. Lett.*, 110:237401, Jun 2013.

[46] Philip TrÃžst Kristensen and Stephen Hughes. Modes and mode volumes of leaky optical cavities and plasmonic nanoresonators. *ACS Photonics*, 1(1):2–10, 2014.

[47] Juanjuan Ren, Sebastian Franke, and Stephen Hughes. Quasinormal modes, local density of states, and classical Purcell factors for coupled loss-gain resonators. *Phys. Rev. X*, 11:041020, Oct 2021.

[48] Christophe Sauvan, Tong Wu, Rachid Zarouf, Egor A. Muljarov, and Philippe Lalanne. Normalization, orthogonality, and completeness of quasinormal modes of open systems: the case of electromagnetism [Invited]. *Opt. Express*, 30(5):6846–6885, Feb 2022.

[49] A. F. Koenderink. On the use of Purcell factors for plasmon antennas. *Opt. Lett.*, 35(24):4208–4210, Dec 2010.

[50] John D. Jackson. *Classical Electrodynamics Third Edition*. John Wiley & Sons, Inc., 1999.

[51] Feng Pan, Kristoffer Karlsson, Austin G Nixon, Levi T Hogan, Jonathan M Ward, Kevin C Smith, David J Masiello, Sile Nic Chormaic, and Randall H Goldsmith. Active control of plasmonic–photonic interactions in a microbubble cavity. *J. Phys. Chem. C*, 126(48):20470–20479, 2022.

[52] Kevin D Heylman, Niket Thakkar, Erik H Horak, Steven C Quillin, Charles Cherqui, Kassandra A Knapper, David J Masiello, and Randall H Goldsmith. Optical microresonators as single-particle absorption spectrometers. *Nat. Photon.*, 10(12):788–795, 2016.

[53] Hugo M Doeleman, Ewold Verhagen, and A Femius Koenderink. Antenna–cavity hybrids: matching polar opposites for Purcell enhancements at any linewidth. *ACS Photonics*, 3(10):1943–1951, 2016.

[54] Martin Frimmer, Toon Coenen, and A. Femius Koenderink. Signature of a Fano resonance in a plasmonic metamolecule's local density of optical states. *Phys. Rev. Lett.*, 108:077404, Feb 2012.

[55] Arthur Losquin and Mathieu Kociak. Link between cathodoluminescence and electron energy loss spectroscopy and the radiative and full electromagnetic local density of states. *ACS Photonics*, 2(11):1619–1627, 2015.

[56] W. E. Moerner and L. Kador. Optical detection and spectroscopy of single molecules in a solid. *Phys. Rev. Lett.*, 62:2535–2538, May 1989.

[57] A. Gaiduk, M. Yorulmaz, P. V. Ruijgrok, and M. Orrit. Room-temperature detection of a single molecules absorption by photothermal contrast. *Science*, 330(6002):353–356, 2010.

[58] Philipp Kukura, Michele Celebrano, Alois Renn, and Vahid Sandoghdar. Single-molecule sensitivity in optical absorption at room temperature. *The Journal of Physical Chemistry Letters*, 1(23):3323–3327, 2010.

[59] L. Cognet, S. Berciaud, D. Lasne, and B. Lounis. Photothermal methods for single nonluminescent nano-objects. *Anal. Chem.*, 80(7):2288–2294, 2008.

[60] Mustafa Yorulmaz, Sara Nizzero, Anneli Hoggard, Lin-Yung Wang, Yi-Yu Cai, Man-Nung Su, Wei-Shun Chang, and Stephan Link. Single-particle absorption spectroscopy by photothermal contrast. *Nano Lett.*, 15(5):3041–3047, 2015.

[61] Mustafa Yorulmaz, Anneli Hoggard, Hangqi Zhao, Fangfang Wen, Wei-Shun Chang, Naomi J. Halas, Peter Nordlander, and Stephan Link. Absorption spectroscopy of an individual Fano cluster. *Nano Lett.*, 16(10):6497–6503, 2016.

[62] Anneli Joplin, Wei-Shun Chang, and Stephan Link. Imaging and spectroscopy of single metal nanostructure absorption. *Langmuir*, 34(13):3775–3786, 2018.

[63] Claire A. West, Stephen A. Lee, Jesse Shooter, Emily K. Searles, Harrison J. Goldwyn, Katherine A. Willets, Stephan Link, and David J. Masiello. Nonlinear effects in single-particle photothermal imaging. *J. Chem. Phys.*, 158(2), 01 2023. 024202.

[64] Kevin D. Heylman, Kassandra A. Knapper, and Randall H. Goldsmith. Photothermal microscopy of nonluminescent single particles enabled by optical microresonators. *J. Phys. Chem. Lett.*, 5(11):1917–1923, 2014.

[65] Kassandra A. Knapper, Kevin D. Heylman, Erik H. Horak, and Randall H. Goldsmith. Chip-scale fabrication of high-Q all-glass toroidal microresonators for single-particle label-free imaging. *Adv. Mater.*, 28(15):2945–2950, 2016.

[66] Kassandra A. Knapper, Feng Pan, Morgan T. Rea, Erik H. Horak, Jeremy D. Rogers, and Randall H. Goldsmith. Single-particle photothermal imaging via inverted excitation through high-Q all-glass toroidal microresonators. *Opt. Express*, 26(19):25020–25030, Sep 2018.

[67] Levi T. Hogan, Erik H. Horak, Jonathan M. Ward, Kassandra A. Knapper, Síle Nic Chormaic, and Randall H. Goldsmith. Toward real-time monitoring and control of single nanoparticle properties with a microbubble resonator spectrometer. *ACS Nano*, 13(11):12743–12757, 2019.

[68] Erik H. Horak, Morgan T. Rea, Kevin D. Heylman, David Gelbwaser-Klimovsky, Semion K. Saikin, Blaise J. Thompson, Daniel D. Kohler, Kassandra A. Knapper, Wei Wei, Feng Pan, Padma Gopalan, John C. Wright, Alán Aspuru-Guzik, and Randall H. Goldsmith. Exploring electronic structure and order in polymers via single-particle microresonator spectroscopy. *Nano Lett.*, 18(3):1600–1607, 2018.

[69] Morgan T. Rea, Feng Pan, Erik H. Horak, Kassandra A. Knapper, Hoang L. Nguyen, Cecilia H. Vollbrecht, and Randall H. Goldsmith. Investigating the mechanism of post-treatment on PEDOT/PSS via single-particle absorption spectroscopy. *J. Phys. Chem. C*, 123(51):30781–30790, 2019.

[70] Qinglan Huang and Brian T Cunningham. Microcavity-mediated spectrally tunable amplification of absorption in plasmonic nanoantennas. *Nano Lett.*, 19(8):5297–5303, 2019.

[71] Freek Ruesink, Hugo M Doeleman, Ruud Hendrikx, A Femius Koenderink, and Ewold Verhagen. Perturbing open cavities: anomalous resonance frequency shifts in a hybrid cavity-nanoantenna system. *Phys. Rev. Lett.*, 115(20):203904, 2015.

[72] Jui-Nung Liu, Qinglan Huang, Keng-Ku Liu, Srikanth Singamaneni, and Brian T Cunningham. Nanoantenna–microcavity hybrids with highly cooperative plasmonic–photonic coupling. *Nano Lett.*, 17(12):7569–7577, 2017.

[73] Freek Ruesink, Hugo M Doeleman, Ewold Verhagen, and A Femius Koenderink. Controlling nanoantenna polarizability through backaction via a single cavity mode. *Phys. Rev. Lett.*, 120(20):206101, 2018.

[74] Kévin G Cognée, Hugo M Doeleman, Philippe Lalanne, and AF Koenderink. Cooperative interactions between nano-antennas in a high-Q cavity for unidirectional light sources. *Light Sci. Appl*, 8(1):115, 2019.

[75] Hugo M Doeleman, Christian D Dieleman, Christiaan Mennes, Bruno Ehrler, and A Femius Koenderink. Observation of cooperative Purcell enhancements in antenna–cavity hybrids. *ACS Nano*, 14(9):12027–12036, 2020.

[76] Yves Auad, Cyrille Hamon, Marcel Tencé, Hugo Lourenço-Martins, Vahagn Mkhitaryan, Odile Stéphan, F Javier Garcia de Abajo, Luiz HG Tizei, and Mathieu Kociak. Unveiling the coupling of single metallic nanoparticles to whispering-gallery microcavities. *Nano Lett.*, 22(1):319–327, 2021.

[77] Matthew Pelton. Modified spontaneous emission in nanophotonic structures. *Nat. Photonics*, 9(7):427, 2015.

[78] Ilan Shlesinger, Kévin G Cognée, Ewold Verhagen, and A Femius Koenderink. Integrated molecular optomechanics with hybrid dielectric–metallic resonators. *ACS Photonics*, 8(12):3506–3516, 2021.

[79] Ilan Shlesinger, Isabelle M Palstra, and A Femius Koenderink. Integrated sideband-resolved SERS with a dimer on a nanobeam hybrid. *Phys. Rev. Lett.*, 130(1):016901, 2023.

[80] Philippe Roelli, Christophe Galland, Nicolas Piro, and Tobias J Kippenberg. Molecular cavity optomechanics as a theory of plasmon-enhanced Raman scattering. *Nat. Nanotechnol.*, 11(2):164–169, 2016.

[81] Mikołaj K Schmidt, Ruben Esteban, Felix Benz, Jeremy J Baumberg, and Javier Aizpurua. Linking classical and molecular optomechanics descriptions of SERS. *Faraday Discuss.*, 205:31–65, 2017.

[82] Martin Fleischmann, Patrick J Hendra, and A James McQuillan. Raman spectra of pyridine adsorbed at a silver electrode. *Chem. Phys. Lett.*, 26(2):163–166, 1974.

[83] M Grant Albrecht and J Alan Creighton. Anomalously intense Raman spectra of pyridine at a silver electrode. *J. Am. Chem. Soc.*, 99(15):5215–5217, 1977.

[84] M Moskovits. Surface roughness and the enhanced intensity of Raman scattering by molecules adsorbed on metals. *J. Chem. Phys.*, 69(9):4159–4161, 1978.

[85] Eric Le Ru and Pablo Etchegoin. *Principles of Surface-Enhanced Raman Spectroscopy: and related plasmonic effects*. Elsevier, 2008.

[86] Judith Langer, Dorleta Jimenez de Aberasturi, Javier Aizpurua, Ramon A Alvarez-Puebla, Baptiste Auguié, Jeremy J Baumberg, Guillermo C Bazan, Steven EJ Bell, Anja Boisen, Alexandre G Brolo, et al. Present and future of surface-enhanced Raman scattering. *ACS Nano*, 14(1):28–117, 2019.

[87] Joel Gersten and Abraham Nitzan. Electromagnetic theory of enhanced Raman scattering by molecules adsorbed on rough surfaces. *J. Chem. Phys.*, 73(7):3023–3037, 1980.

[88] Zhao, Lasse Jensen, and George C. Schatz. Pyridine-Ag_{20} cluster: A model system for studying surface-enhanced Raman scattering. *J. Am. Chem. Soc.*, 128(9):2911–2919, Mar 2006.

[89] Lasse Jensen, Christine M Aikens, and George C Schatz. Electronic structure methods for studying surface-enhanced Raman scattering. *Chem. Soc. Rev.*, 37(5):1061–1073, 2008.

[90] David J Masiello and George C Schatz. Many-body theory of surface-enhanced Raman scattering. *Phys. Rev. A*, 78(4):042505, 2008.

[91] Mikolaj K Schmidt, Ruben Esteban, Alejandro González-Tudela, Geza Giedke, and Javier Aizpurua. Quantum mechanical description of Raman scattering from molecules in plasmonic cavities. *ACS Nano*, 10(6):6291–6298, 2016.

[92] Markus Aspelmeyer, Tobias J Kippenberg, and Florian Marquardt. Cavity optomechanics. *Rev. Mod. Phys.*, 86(4):1391, 2014.

[93] Felix Benz, Mikolaj K Schmidt, Alexander Dreismann, Rohit Chikkaraddy, Yao Zhang, Angela Demetriadou, Cloudy Carnegie, Hamid Ohadi, Bart De Nijs, Ruben Esteban, Javier Aizpurua, and Jeremy J. Baumberg. Single-molecule optomechanics in "picocavities". *Science*, 354(6313):726–729, 2016.

[94] Yuan Zhang, Javier Aizpurua, and Ruben Esteban. Optomechanical collective effects in surface-enhanced Raman scattering from many molecules. *ACS Photonics*, 7(7):1676–1688, 2020.

[95] Yuhao Xu, Huatian Hu, Wen Chen, Pengfei Suo, Yuan Zhang, Shunping Zhang, and Hongxing Xu. Phononic cavity optomechanics of atomically thin crystal in plasmonic nanocavity. *ACS Nano*, 16(8):12711–12719, 2022.

[96] Niclas S Mueller, Rakesh Arul, Lukas A Jakob, Matthew Oliver Blunt, Tamas Földes, Edina Rosta, and Jeremy J Baumberg. Collective mid-infrared vibrations in surface-enhanced Raman scattering. *Nano Lett.*, 22(17):7254–7260, 2022.

[97] Steven C Quillin, Charles Cherqui, Nicholas P Montoni, Guoliang Li, Jon P Camden, and David J Masiello. Imaging plasmon hybridization in metal nanoparticle aggregates with electron energy-loss spectroscopy. *J. Phys. Chem. C*, 120(37):20852–20859, 2016.

[98] Charles Cherqui, Nicholas W Bigelow, Alex Vaschillo, Harrison Goldwyn, and David J Masiello. Combined tight-binding and numerical electrodynamics understanding of the STEM/EELS magneto-optical responses of aromatic plasmon-supporting metal oligomers. *ACS Photonics*, 1(10):1013–1024, 2014.

[99] Charles Cherqui, Niket Thakkar, Guoliang Li, Jon P Camden, and David J Masiello. Characterizing localized surface plasmons using electron energy-loss spectroscopy. *Annu. Rev. Phys. Chem.*, 67:331–357, 2016.

[100] Claude Cohen-Tannoudji, Jacques Dupont-Roc, and Gilbert Grynberg. *Photons and atoms–Introduction to quantum electrodynamics*. Wiley, 1997.

[101] Kevin C. Smith, Yueyang Chen, Arka Majumdar, and David J. Masiello. Active tuning of hybridized modes in a heterogeneous photonic molecule. *Phys. Rev. Appl.*, 13:044041, Apr 2020.

[102] C. Praise Anyanwu, Grace Pakeltis, Philip D. Rack, and David J. Masiello. Nanoscale characterization of individual three-dimensional split ring resonator systems. *ACS Appl. Opt. Mater.*, 1(2):607–614, 2023.

[103] E. T. Jaynes and F. W. Cummings. Comparison of quantum and semiclassical radiation theories with application to the beam maser. *Proc. IEEE*, 51(1):89–109, 1963.

[104] Kyoung-Duck Park, Molly A May, Haixu Leng, Jiarong Wang, Jaron A Kropp, Theodosia Gougousi, Matthew Pelton, and Markus B Raschke. Tip-enhanced strong coupling spectroscopy, imaging, and control of a single quantum emitter. *Sci. Adv.*, 5(7):eaav5931, 2019.

[105] Heiko Groß, Joachim M Hamm, Tommaso Tufarelli, Ortwin Hess, and Bert Hecht. Near-field strong coupling of single quantum dots. *Sci. Adv.*, 4(3):eaar4906, 2018.

[106] Irene Dolado, Carlos Maciel-Escudero, Elizaveta Nikulina, Evgenii Modin, Francesco Calavalle, Shu Chen, Andrei Bylinkin, Francisco Javier Alfaro-Mozaz, Jiahan Li, James H Edgar, et al. Remote near-field spectroscopy of vibrational strong coupling between organic molecules and phononic nanoresonators. *Nat. Commun.*, 13(1):6850, 2022.

[107] Bill Barnes, Francisco García Vidal, and Javier Aizpurua. Special issue on "strong coupling of molecules to cavities". *ACS Photonics*, 5(1):1–1, 2018.

[108] Matthias Hensen, Tal Heilpern, Stephen K. Gray, and Walter Pfeiffer. Strong coupling and entanglement of quantum emitters embedded in a nanoantenna-enhanced plasmonic cavity. *ACS Photonics*, 5(1):240–248, 2018.

[109] Francisco J Garcia-Vidal, Cristiano Ciuti, and Thomas W Ebbesen. Manipulating matter by strong coupling to vacuum fields. *Science*, 373(6551), 2021.

[110] Martin Wersäll, Jorge Cuadra, Tomasz J Antosiewicz, Sinan Balci, and Timur Shegai. Observation of mode splitting in photoluminescence of individual plasmonic nanoparticles strongly coupled to molecular excitons. *Nano Lett.*, 17(1):551–558, 2017.

[111] Haixu Leng, Brian Szychowski, Marie-Christine Daniel, and Matthew Pelton. Strong coupling and induced transparency at room temperature with single quantum dots and gap plasmons. *Nat. Commun.*, 9(1):4012, 2018.

[112] Andrea Konečná, Tomáš Neuman, Javier Aizpurua, and Rainer Hillenbrand. Surface-enhanced molecular electron energy loss spectroscopy. *ACS Nano*, 12(5):4775–4786, 2018.

[113] Andrew B Yankovich, Battulga Munkhbat, Denis G Baranov, Jorge Cuadra, Erik Olsén, Hugo Lourenço-Martins, Luiz HG Tizei, Mathieu Kociak, Eva Olsson, and Timur Shegai. Visualizing spatial variations of plasmon-exciton polaritons at the nanoscale using electron microscopy. *Nano Lett.*, 19(11):8171–8181, 2019.

[114] Marc R Bourgeois, Elliot K Beutler, Siamak Khorasani, Nicole Panek, and David J Masiello. Nanometer-scale spatial and spectral mapping of exciton polaritons in structured plasmonic cavities. *Phys. Rev. Lett.*, 128(19):197401, 2022.

[115] Kangpeng Wang, Raphael Dahan, Michael Shentcis, Yaron Kauffmann, Adi Ben Hayun, Ori Reinhardt, Shai Tsesses, and Ido Kaminer. Coherent interaction between free electrons and a photonic cavity. *Nature*, 582(7810):50–54, 2020.

[116] Aviv Karnieli, Shai Tsesses, Renwen Yu, Nicholas Rivera, Zhexin Zhao, Ady Arie, Shanhui Fan, and Ido Kaminer. Quantum sensing of strongly coupled light-matter systems using free electrons. *Sci. Adv.*, 9(1):eadd2349, 2023.

[117] Jaysen Nelayah, Mathieu Kociak, Odile Stéphan, F J García de Abajo, Marcel Tencé, Luc Henrard, Dario Taverna, Isabel Pastoriza-Santos, Luis M Liz-Marzán, and Christian Colliex. Mapping surface plasmons on a single metallic nanoparticle. *Nat. Phys.*, 3(5):348–353, 2007.

[118] Albert Polman, Mathieu Kociak, and F Javier García de Abajo. Electron-beam spectroscopy for nanophotonics. *Nat. Mater.*, 18(11):1158–1171, 2019.

[119] Jordan A Hachtel, Jingsong Huang, Ilja Popovs, Santa Jansone-Popova, Jong K Keum, Jacek Jakowski, Tracy C Lovejoy, Niklas Dellby, Ondrej L Krivanek, and Juan Carlos Idrobo. Identification of site-specific isotopic labels by vibrational spectroscopy in the electron microscope. *Science*, 363(6426):525–528, 2019.

[120] F Javier García de Abajo and Valerio Di Giulio. Optical excitations with electron beams: Challenges and opportunities. *ACS Photonics*, 8(4):945–974, April 2021.

[121] D. Braak. Integrability of the Rabi model. *Phys. Rev. Lett.*, 107:100401, Aug 2011.

[122] Daniel Z. Rossatto, Celso J. Villas-Bôas, Mikel Sanz, and Enrique Solano. Spectral classification of coupling regimes in the quantum Rabi model. *Phys. Rev. A*, 96:013849, Jul 2017.

[123] Mikael Kuisma, Benjamin Rousseaux, Krzysztof M Czajkowski, Tuomas P Rossi, Timur Shegai, Paul Erhart, and Tomasz J Antosiewicz. Ultrastrong coupling of a single molecule to a plasmonic nanocavity: A first-principles study. *ACS Photonics*, 9(3):1065–1077, March 2022.

[124] Li Li, Lei Wang, Chenglin Du, Zhongyuan Guan, Yinxiao Xiang, Wei Wu, Mengxin Ren, Xinzheng Zhang, Aiwei Tang, Wei Cai, et al. Ultrastrong coupling of CdZnS/ZnS quantum dots to bonding breathing plasmons of aluminum metal–insulator–metal nanocavities in near-ultraviolet spectrum. *Nanoscale*, 12(5):3112–3120, 2020.

[125] P. Forn-Díaz, L. Lamata, E. Rico, J. Kono, and E. Solano. Ultrastrong coupling regimes of light-matter interaction. *Rev. Mod. Phys.*, 91:025005, Jun 2019.

[126] Anton Frisk Kockum, Adam Miranowicz, Simone De Liberato, Salvatore Savasta, and Franco Nori. Ultrastrong coupling between light and matter. *Nat. Rev. Phys.*, 1(1):19–40, 2019.

Chapter 4

NANOSCALE CHARACTERIZATION OF INDIVIDUAL THREE-DIMENSIONAL SPLIT RING RESONATOR SYSTEMS

4.1 Abstract

In this article we investigate the hybridization of three-dimensional plasmonic split ring resonator (SRR) pairs using focused electron beam nanospectroscopy and model their combined electric and magnetic responses using electromagnetic theory and numerical calculations. Specifically, we fabricate 3D SRR dimers with varying in-plane rotations and out-of-plane tilts, and perform electron energy loss spectroscopy (EELS) measurements to elucidate the impact of their 3D electric and magnetic interactions upon the EEL spectrum of each individual SRR dimer. Based on the competition between the SRR's electric and magnetic interactions within our model, we find that varying the 3D tilt angle diminishes the magnetic coupling, but increases the overall mode mixing. Through further modeling of the experimental data, we determine the system's electric and magnetic coupling constants, as well as the overall effective coupling constant, a useful metric for characterizing the strength of light-matter interaction. We additionally explore the potential for geometric frustration in the magnetic mode ordering of a coupled SRR trimer using both EELS experiment and companion theoretical modeling. Taken together, the insight gained into the behavior of coupled 3D SRRs serves as a stepping stone to the rational design of 3D photonic metamaterials endowed with even richer optical functionality.

4.2 Introduction

Negative index of refraction (NIR) metamaterials have found significant importance in nanophotonics owing to their remarkable optical properties that are unable to be achieved in naturally occurring materials [1, 2, 3, 4, 5, 6, 7, 8]. Fundamental to the design of NIR metamaterials is the split ring resonator (SRR), which has been used in a variety of applications including perfect lenses [9, 10, 11, 12], biosensors [13, 14], antennas [15, 16], and absorbers and filters [17, 18]. When arranged in an array, individual SRRs act as "atoms" with the emergent optical properties of the metamaterial arising through their mutual coupling, thus providing impetus for detailed studies of the fundamental two-body interactions between pairs of SRR units. [19, 20]

While far-field optical characterization techniques are commonly used to investigate SRR-based metamaterials [21, 22], few studies have employed sub-diffraction-limited probes such as scanning transmission electron microscopy (STEM) electron energy loss spectroscopy (EELS) to measure SRR couplings at their own native length scale. [23] STEM-EELS provides nanometer-scale spatial information together with correlated spectroscopic responses capable, e.g., of revealing dark modes undetectable by far-field characterization tools. Clear distinction of the bright and dark modes is critical to quantify the strength and to elucidate the nature of light-matter interaction. In Ref. [24], von Cube et al. showed the progression from distinct optically bright and dark eigenmodes in small arrays (i.e., $2-4$ SRRs) to the formation of a quasi-continuum of modes in the interior, and edge modes at the boundaries of a large array. In another EELS study, Liang et al. [25] investigated individual Au SRR dimers, fabricated with either $0°$, $90°$, and $180°$ relative planar angle to elucidate the hybridization of their fundamental modes. These studies combined numerical simulations with experimental EELS measurements to elucidate the interplay between the SRR's electric and magnetic dipole moments in the hybridization of coupled SRRs

within a planar or two-dimensional geometry.

Moving beyond planar structures, little consideration has been given to 3D SRRs with electric and magnetic responses that can be oriented arbitrarily in three dimensional space, which would produce an even richer set of interactions and emergent responses. Ref. [26] has investigated "vertical" oriented SRRs using cathodoluminescene and EELS to study the fundamental magnetic dipole mode. However, due to challenges of fabricating 3D SRRs, it remains difficult to clearly distinguish the magnetic mode and elucidate its role in the hybridization of SRR pairs. To this end, the work presented in Ref. [27] achieves a breakthrough in fabricating plasmonic 3D SRR nanoresonators, using focused electron beam induced deposition (FEBID) to deposit nonplasmonic 3D scaffolds, which are subsequently isolated with a conformal SiO_2 layer and then coated with a gold layer to create functional 3D plasmonic nanostructures. Building from this work, here we investigate the effect of 3D out-of-plane tilting on the electric and magnetic dipole couplings in individual nanofabricated SRR dimers, and the downstream impacts in metamaterial design using monochromated aberration corrected STEM-EELS and companion theoretical modeling.

The STEM-EELS measurements presented in this study expose the effects of 3D geometry upon the interaction between individual SRRs. Theoretical analysis of the observed data accounts for the induced electric and magnetic dipoles on each SRR as well as their mutual near-field couplings in SRR dimers as probed by STEM electron beam. We then map the dynamics of the SRR surface current density onto effective oscillator equations of motion, with an effective coupling constant exhibiting both 2D and 3D angular dependence. This description is well suited for an analytic analysis of the EEL probability which shows that for a particular orientation, increasing the 3D tilt angle diminishes the magnetic coupling, but enhances the overall light-matter interaction strength. Based upon this model, we additionally examine the hybridization of individual 2D SRR trimers measured using EELS. Taken together, this study elucidates the geometric effects of 3D tilt on the SRR magnetic dipole moment and

its role in the hybridization of coupled 3D SRRs, thus serving as a stepping stone for nano-engineering NIR metamaterials composed of coupled 3D SRR units.

4.3 Results and Discussion

Fig. 4.1 and 4.2 display a series of Au SRR pairs with varying in-plane orientations and out-of-plane tilts, each SRR with 450 nm diameter, 270° arc length. To provide a baseline for the out-of-plane tilting in the three-dimensional study, first, the pair of SRRs are lithographically patterned on a SiN_x membrane, with a relative planar angle of 0°, 45°, 90°, 135°, or 180°, as shown on the top panel, Fig. 4.1b-f. Experimental EELS measurements are performed on each SRR pair, with the electron beam probe positioned at the colored dots, traveling into the plane of the page. Fig. 4.1a displays the corresponding color codded EEL spectra showing a single peak for the 90° orientation and a clear peak splitting into the bonding and antibonding dipolar modes for the 0°, 45°, 135°, and 180° planar orientations. The signatures of the bonding and antibonding modes are identified by the experimental EEL spectrum images, illustrated in Fig. 4.1g-o: The in-phase bonding modes are observed at the lower energy maps (Fig. 4.1g-h, j-k) with the zero EELS intensity signature in the gap; while the out-of-phase antibonding modes are observed at the higher energy maps (Fig. 4.1l-o) with the high EELS intensity signature in the gap.

The geometric effect on the spectrum of a coupled pair of SRRs, arbitrarily oriented in space, results from their doubly coupled electromagnetic interaction. In particular, the progression of the mode mixing in the STEM-EELS of Fig. 4.1 is a known characteristic behavior that stems from the interplay between electric and magnetic interactions of coupled planar SRRs [19, 28]. Describing the EEL spectra within a model that can be generalized to three dimensions requires knowledge of the potential energy of interaction between the SRR and the evanescent electric field of a STEM electron beam, as well as the interaction energy between coupled SRRs.

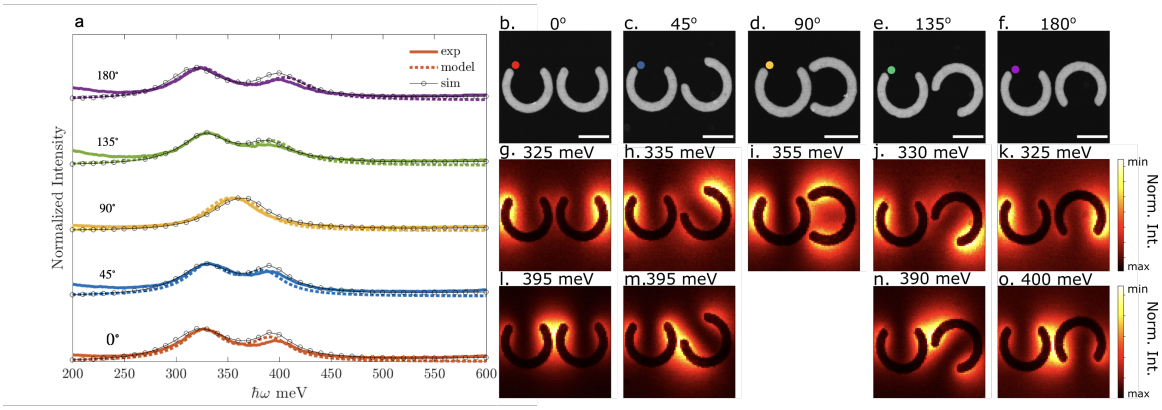

Figure 4.1: (a) Experimental (solid), simulation (circle), and model (dashed) EEL spectra taken at the SRR outer tip for planar rotational study. (b-f) HAADF images of each SRR dimer with a colored circle indicating where the spectra in panel a were acquired. Corresponding spectrum images show the lower-energy (g-k) and higher-energy (l-p) normal modes of the system. Scale bar = 300 nm.

Analysis of the electron-beam-driven SRR dimer

An electron beam oriented such as to point into the plane of the page of Fig. 4.1 drives current about the circular path of one of the pair of SRRs, with the following interaction potential energy,

$$\begin{aligned} U_{\text{el}} &= \oint \mathbf{F}_{\text{el}} \cdot \mathbf{ds}_1 \\ &\approx q_1 \mathbf{E}_{\text{el}} \cdot \hat{\mathbf{x}}_1, \end{aligned} \tag{4.1}$$

where q_1 is the total charge for the fundamental dipole mode. Thus the force from the evanescent electric field of the electron beam polarizes the driven SRR in the direction defined by the unit vector $\hat{\mathbf{x}}_1$ across the split of the ring; the polarized field induced on the SRR has a dominant dipolar electromagnetic response that prevails within the spectral window of the STEM-EELS analysis, and it is well separated from higher energy modes [27]. With its large distance to the second SRR, the influence of the electron beam upon the second SRR is neglected, with the beam positioned at each

of the bullets in the upper panels of Fig. 4.1b-f.

The induced current about the circular path of the driven SRR sets up a magnetic dipole moment whose field is normal to the SRR plane and orthogonal to the electric dipole field set across the split direction. It is through this electric field and induced magnetic flux density of these electric and induced magnetic dipoles that the two SRRs interact. The interaction can be expressed from Lorentz force, such that,

$$\begin{aligned} U_{12} &= \oint_{\partial s_2} \mathbf{F}_1 \cdot \mathbf{ds}_2 \\ &= q \oint_{\partial s_2} \left(\mathbf{E}_1 + \frac{\mathbf{v}_2}{c} \times \mathbf{B}_1 \right) \cdot \mathbf{ds}_2, \end{aligned} \tag{4.2}$$

where $\mathbf{E}_1$ and $\mathbf{B}_1$ are the electric field and the induced magnetic flux density, both from the first ring, acting on the closed circular, surface path ∂s_2 of the second ring. In this system the drift velocity $\mathbf{v}_2$ about the second ring is due to the current induced by the field $\mathbf{E}_1$. To clarify the interaction mechanism, we express the interaction potential as

$$\begin{aligned} U_{12} &= q \oint_{\partial s_2} \mathbf{E}_1 \cdot \mathbf{ds}_2 + \oint_{\partial s_2} \left(\frac{\mathbf{v}_2}{c} \times \mathbf{B}_1 \right) \cdot \mathbf{ds}_2 \\ &= q \oint_{\partial s_2} \mathbf{E}_1 \cdot \mathbf{ds}_2 - \oint_{\partial s_2} \mathbf{B}_1 \cdot \left(\frac{\mathbf{v}_2}{c} \times \mathbf{ds}_2 \right) \\ &\approx [\mathbf{E}_1 \cdot \mathbf{p}_2 - \mathbf{B}_1 \cdot \mathbf{m}_2], \end{aligned} \tag{4.3}$$

where $\mathbf{p}_2$ and $\mathbf{m}_2$ are the induced electric and magnetic dipole moments of the second SRR, with $\mathbf{p}_2$ in the direction across the split and $\mathbf{m}_2$ normal to the SRR plane. For the orientation in Fig. 4.1d, $\mathbf{E}_1$ and $\mathbf{p}_2$ are orthogonal so the first term vanishes and the interaction is purely magnetic, however small, resulting in a weak mode mixing and thus a negligible spectral splitting of the normal modes. However in Fig. 4.1a and 4.1b, $\mathbf{E}_1$ and $\mathbf{p}_2$ are either in phase or out-of-phase, resulting in a deconstructive or constructive interaction with the B-field, thus giving rise to mode mixing having varying normal mode splitting.

Theoretical description of the EEL spectra

The following paragraphs set out the derivation of an analytic expression for the observed STEM-EELS measurements in Fig. 4.1 and Fig. 4.2. It also resolves the in-plane ϕ and out-of-plane θ angular dependence of the interaction terms defined in Eqn. (3). These interaction terms relate to the coupling constant quantifying the strength of light-matter interaction between the coupled SRR pair. This coupling constant will quantify the geometric effect of 3D tilting on mode mixing in Fig. 4.2.

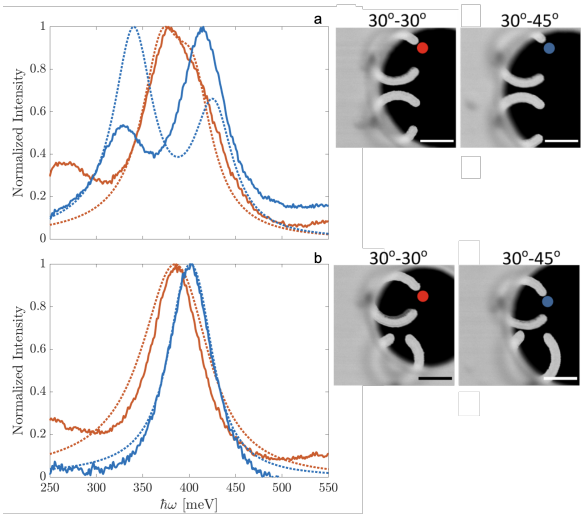

Figure 4.2: EEL spectra of individual coupled 3D SRR dimers. For each dimer, the SRRs are placed side-by-side. (a) Experimental (solid) and model (dashed) EEL spectra, with the electron probe placed at one of the SRR's outer tips. The electron probe is represented as a color-coded circle in the HAADF image, corresponding to each color-coded spectrum. For the blue curves, the 3D out-of-plane tilt (θ) angles are 30°-30°, respectively, for the electron probe driven-undriven SRRs in the dimer, while for the red curves the θ angles are 30°-45°, respectively. (b) The planar orientation for the SRR dimer is as such in Fig. 4.1d, and then the EEL spectra are acquired for same the 3D tilt orientations conducted in (a).

Fig. 4.2a shows a 3D tilt study of a coupled SRR dimer placed side-by-side. The setup is shown in the adjacent high angle annular dark field (HAADF) image: the top SRR tilts out-of-plane at 30° and the bottom SRR tilts at 30° (left panel) and

45° (right panel). Thus for the left and right panels, the relative tilt angles between the top and bottom SRRs are $\theta = 0°$ and $\theta = 15°$, respectively. The EEL spectra in panels a,b are measured with the electron beam placed at the colored circles at the outer tip of the top SRR. In both spectra, the hybridized modes result from the electric and induced magnetic dipole interactions.

In contrast, Fig. 4.2b shows a case where the bottom SRR has been rotated 90° in-plane to uncouple the electric field interaction between both SRRs. The result is a weakly coupled dimer, as shown in the negligible spectral splitting, due to a weak, purely magnetic interaction, and as the bottom SRR tilts out-of-plane at 45°, the magnetic interaction weakens further, and the spectra reduces to the uncoupled system identical to the SRR monomer.

To evaluate the electric and magnetic coupling constants and to analyze the role of the magnetic interaction in the STEM-EEL measurements of Fig. 1 and Fig. 2, we will need to derive the EEL probability [29, 30]

$$\Gamma_{\mathrm{EEL}}(\omega) = \frac{|\mathbf{E}_{\mathrm{el}}(\mathbf{R},\omega)\cdot\hat{\mathbf{x}}_1|^2}{\pi\hbar}\mathrm{Im}\,\alpha_1(\omega) \tag{4.4}$$

of an SRR dimer from a model containing both electric and magnetic interactions. In this expression $\mathbf{E}_{\mathrm{el}}$ is the evanescent field of the STEM electron and α_1 is the polarizability of the first SRR coupled to the second SRR via near-field electric and magnetic dipole interactions. It is defined as

$$\alpha_1\mathbf{E}_{\mathrm{el}}(\mathbf{R},\omega) = q_1(\omega)\hat{\mathbf{x}}_1 \tag{4.5}$$

in terms of the dynamical coordinate $q_1(\omega)$ representing the total charge on the driven SRR. The Lagrangian governing the dynamics of the coupled SRR dimer in the external field of the electron beam is given by

$$\begin{aligned} L &= T - U_{12} - U_{\mathrm{el}} \\ &= \sum_i A\dot{q}_i^2 - \sum_i Bq_i^2 - \frac{1}{2}\sum_{\substack{i,j \\ i\neq j}}\left[\mathbf{E}_i(q_j)\cdot\mathbf{p}_j - \mathbf{B}_i(q_j)\cdot\mathbf{m}_j\right] - \sum_{i=1}\mathbf{E}_{\mathrm{el}}(q_i)\cdot\mathbf{p}_i. \end{aligned} \tag{4.6}$$

The generalized coordinate is the time-dependent amplitude of the total charge $q(t)$ on each SRR. More so, assuming identical SRRs, then A and B are constants equal across all SRRs. The quantity A has dimensions of inductance ($\mathrm{s}^2{\cdot}\mathrm{cm}^{-1}$), which behaves as the inertial quantity analogous to the mass on a mechanical oscillator. And it follows that B has units of inverse capacitance (cm^{-1}), such that the resonance frequency of the SRR is given by $\sqrt{B/A}$. Then the simplified Lagrangian yields

$$L = A\left[\sum_i \dot{q}_i^2 - \omega_0^2 q_i^2 + \frac{1}{2}\sum_{\substack{ij \\ i\neq j}} \beta \dot{q}_i \dot{q}_j - g_E q_i q_j\right] - \sum_{i=1} (\mathbf{E}_{\mathrm{el}} \cdot \hat{\mathbf{x}}_i) q_i, \tag{4.7}$$

where β and g_E are geometric coupling constants of the near-field electric and magnetic interactions, respectively. In the absence of the drive field of the electron beam, Eq. (7) is similar to the well know Lagrangian of coupled SRRs [31, 20, 32, 33, 34]. However, Eq. (7) yields the steady state solution $q_1(\omega)$ of the electron beam driven, coupled SRR.

It follows that the Euler-Lagrange equations of motion produce an electric, position dependent coupling, as well as a magnetic, velocity dependent coupling. Following the procedure outlined in reference [35] (appendix A), a linear transformation of the Euler-Lagrange equations from Eq. (7) yields the following coupled effective oscillator equations of motion representing the coupled fundamental dipolar modes of an SRR pair, such that,

$$\ddot{q}_1(t) + \gamma_1 \dot{q}_1 + \Omega_0^2 q_1 + G q_2 = -\frac{\mathbf{E}_{\mathrm{el}} \cdot \hat{\mathbf{x}}_1}{2A} \tag{4.8}$$

$$\ddot{q}_2(t) + \gamma_2 \dot{q}_2 + \Omega_0^2 q_2 + G q_1 = 0, \tag{4.9}$$

where in an ad hoc fashion we have added a term that depends on the generalized velocity $\gamma_1 = \gamma_2 = \gamma_0$, for dissipative loss. Note that the dimer system bears new effective oscillator parameters, with defined effective resonance frequency and coupling

constant, i.e.,

$$\Omega_0^2 = \omega_0^2 - \frac{g_E \beta}{4} \tag{4.10}$$

$$G_{\text{eff}} = \Big|\frac{G}{\Omega_0}\Big|. \tag{4.11}$$

The coupling constant G expresses the angular dependence of the electric and magnetic near-field interaction such that

$$\begin{aligned} G &= [g_E(\phi) - \beta(\theta)\omega_0^2]/2 \\ &= [g_E(\phi) - g_B(\theta)]/2 \\ &= [|g_E|\cos\phi - |g_B|\cos\theta]/2. \end{aligned} \tag{4.12}$$

(Here the angles ϕ and θ correspond to the relative in-plane rotation and out-of-plane tilts, respectively, of the second SRR with respect to the first, as shown in Fig. 4.1 and 4.2.) Finally we express the dynamics of the total charge on the driven SRR dipole oscillator in the frequency domain as

$$q_1(\omega) = \frac{-\mathbf{E}_{\text{el}}(\mathbf{R},\omega)\cdot\hat{\mathbf{x}}_1}{2A}\frac{1}{\Omega_0^2 - \omega^2 - i\gamma_1\omega - \frac{G^2}{\Omega_0^2 - \omega^2 - i\gamma_2\omega}}. \tag{4.13}$$

Eq. (13) yields the solution to Eq. (5), the polarizability of the driven SRR. The self energy term in the denominator of Eq. (13) expresses the perturbation due to the near-field interaction with the second SRR. With these equations, the analytic expression of the EEL probability distribution function in Eq. (4) and the effective coupling constant in Eqs. (11-12) capture the behavior of the observed STEM-EELS measurements in Fig. 4.1 and 4.2.

To illustrate, first, in Fig. 4.1 (without tilting, $\theta = 0°$), the strength of the light-matter interaction G_{eff} approaches a minimum and maximum value for the planer orientations $\phi = 90°$ and $\phi = 180°$. This value corresponds to the normal mode spectral splitting of the coupled SRR pair. For instance, the weak interaction strength at $\phi = 90°$ is due to the purely magnetic interaction $\big[|g_E|\sin(\phi = 90) - |g_B|\cos(\theta = 0)|\big]/\Omega_0 = |g_B|/\Omega_0$. More so, Eq. (12) predicts that 3D tilting ($\theta \neq 0$)

has the effect of strengthening SRR couplings by decreasing the counteraction of the induced magnetic interaction on the strong electric interaction. As in Fig. 4.2a, the spectral splitting increases as the 3D tilt angle increases. This result justifies the claim that tilting out-of-plane diminishes the induced magnetic interaction, yet enhancing the overall light-matter interaction between coupled SRRs.

Furthermore, Fig. 4.2b explores the purely induced magnetic interaction in 3D. First, the initial frame of the SRR pair is as such in the orientation at $\phi = 90°$. Then the undriven, coupled SRR is tilted out-of-plane. In this case, the coupling strength reduces to the simple expression $|g_B|/\Omega_0 \cos\theta$. Thus tilting out-of-plane (where $\theta \to 90°$) results in a negligible near-field interaction, and the spectra reduces to the case of the uncoupled system identical to the SRR monomer, as observed in Fig. 4.2b and in the estimates of the fit parameters in Tables 4.1. In general, this 3D tilt study distinguishes the magnetic dipole, and characterizes its role in the hybridization scheme of coupled SRRs.

Model application: estimating the interaction strength of coupled SRRs

Table 4.1: 3D Parameter estimates

ϕ [deg]	θ [deg]	$\hbar\Omega_0$ [meV]	$\hbar\gamma_0$ [meV]	$\hbar\lvert G_{\text{eff}}\rvert$ [meV]	$\hbar\omega_0$ [meV]
0	0	389	52	33	410
0	15	387	51	85	$\sim$
90	0	390	78	20	$\sim$
90	15	404	48	15	$\sim$

As mentioned, Fig. 4.1 provides a baseline for the 3D study. Applying the EEL probability distribution function in Eq. (4) as a fit function to the data in Fig. 4.1 yields estimates for the system parameters (see Table II). First the fit of Eq. (4) to

the simulation data of the SRR monomer spectrum (according to the experimental system) yields estimates of the natural resonance frequency ω_0, and the inductance A. Then the fit to the simulation data of the SRR dimer spectrum at the initial orientation (Fig. 4.1b, $\phi = 0$) and the pure magnetic orientation (Fig. 4.1d, $\phi = 90$) yields estimates of the coupling constant magnitudes $|g_E|$ and $|g_H|$. With these parameters, calculations using Eqs. (10) and (12) yield the effective resonance frequency Ω_0, and coupling constant G. The values of Ω_0 and G calculated from the model serve as bounds for the fitting procedure to the experimental STEM-EELS measurements, from which the true values of Ω_0 and G are determined. We note that in the fitting procedure outlined, γ_0 is the only free parameter. Finally with the estimates of the system parameters, as shown in Table II, the model is overlain to the STEM-EELS spectra.

Table 4.2: Parameter estimates

A $[\mathrm{s}^2 \cdot \mathrm{cm}^{-1}]$	$\hbar\omega_0$ [meV]	$\hbar\lvert g_E\rvert$ [meV^2]	$\hbar\lvert g_H\rvert$ [meV^2]
1.885×10^{-31}	359	6.5×10^{-2}	9.0×10^{-3}

ϕ [deg]	$\hbar\Omega_0$ [meV]	$\hbar\gamma_0$ [meV]	$\hbar\lvert G_{\mathrm{eff}}\rvert$ [meV]
0	362	47	65
45	360	47	54
90	359	47	25
135	365	55	64
180	370	58	82

Applying the parameter estimates A, ω_0, $|g_E|$, and $|g_B|$ to Eqs. (10) and (12) for Ω_0 and G yields the normal mode energies $\Omega_\mp = \sqrt{\Omega_0(\phi,\theta)^2 \mp G(\phi,\theta)}$. Fig. 4.3a is the anti-crossing graph of the normal mode energies. These normal mode calculations are benchmarked with the fit estimates of Ω_0 and G from the numeric and experimental

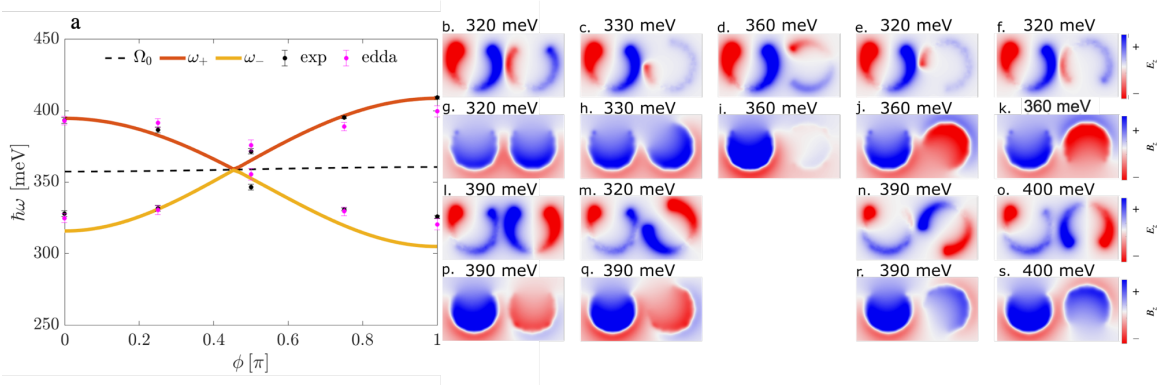

Figure 4.3: (a) Anti-crossing of the normal mode energies from the derived analytical expression $\Omega_{\mp} = \sqrt{\Omega_0(\phi,\theta)^2 \mp G(\phi,\theta)}$ (solid) and fit estimates of the experimental (black dots) and numerical *e*-DDA (magenta dots) normal mode energies for the planar rotational study in Fig. 1. The progression of the normal mode splitting is tuned by changing the coupling strength as a function of the in-plane ϕ orientation of the second SRR. Numerical *e*-DDA electric (b-f) and magnetic (g-k) field profiles of the bonding modes are compared against electric (i-o) and magnetic (p-s) field profiles of the anti-bonding modes.

data. In essence Fig. 4.3a shows that changing the orientation of the SRRs tunes the degree of normal mode mixing, where Ω_- and Ω_+ are the in- and out-of-phase normal mode energies whose mode profiles are shown in the EM field maps of Fig. 4.3b-s.

Moreover, the EM field maps in Fig. 4.3b-s show a phase change in the normal mode of the induced magnetic dipoles when the second coupled SRR changes orientation from $\phi = 0°$ to $\phi = 180°$. For example, the B-fields of the induced magnetic dipoles are in-phase in the lower energy normal mode at $\phi = 0°$, however, out-of-phase at $\phi = 180°$ (see Fig. 4.3g and k). This apparent inversion is due to Faraday's law of induction, i.e., changing the orientation of the coupled SRR from $\phi = 0$ to $\phi = 180°$ changes the direction of the induced current about its loop, and thus, changes the direction of the B-field normal to its plane.

Magnetic ordering of the SRR trimer

In Fig. 4.4, a planar trimer of SRRs (450 nm diameter, 270° arc length) is arranged in a D_{3h} symmetry to explore the effects of geometric frustration in the magnetic dipole ordering of its normal modes. EEL spectra are acquired at the inner arm and at the gap of the SRR trimer (see colored dots in the HAADF image in Fig. 4.4a) to preferentially excite the lower- and higher-energy normal modes, respectively. Note that the beam position located in the gap center (blue) excludes the lower-energy in-phase normal mode by symmetry. Fig. 4.4b shows the measured EEL spectra with resonant energies at 300 meV and 400 meV, while Fig. 4.4 c-d displays the measured spectrum images collected at these resonant energies. The results from numerical EEL simulation of the SRR trimer (Fig. 4.4e-h) show the electric and magnetic mode profiles of the in-phase lower-energy normal mode (Fig. 4.4e,g) and out-of-phase higher-energy normal mode (Fig. 4.4f,h), which is doubly degenerate. These field profiles are consistent with their respective measured spectrum images from panel c.

In the lower-energy normal mode, the electric dipoles are in-phase (all pointing head-to-tail), and in this point group symmetry, the direction of the circular current is the same on each loop of the SRR; this gives rise to magnetic dipole moments with ferromagnetic (FM) ordering (all pointing out-of-plane). In the higher-energy normal mode, however, the electric dipoles are out-of-phase, and thus, the direction of the circular current is different on each loop of the SRR; this gives rise to magnetic dipole moments with anti-ferromagnetic (AFM) ordering. Thus by correlating experimental EELS measurements with calculated induced electric and magnetic field profiles, Fig. 4 shows that the magnetic dipole ordering within a given SRR trimer normal mode is dictated by the specific current path about each loop of each SRR as excited by the STEM electron probe at particular impact parameters.

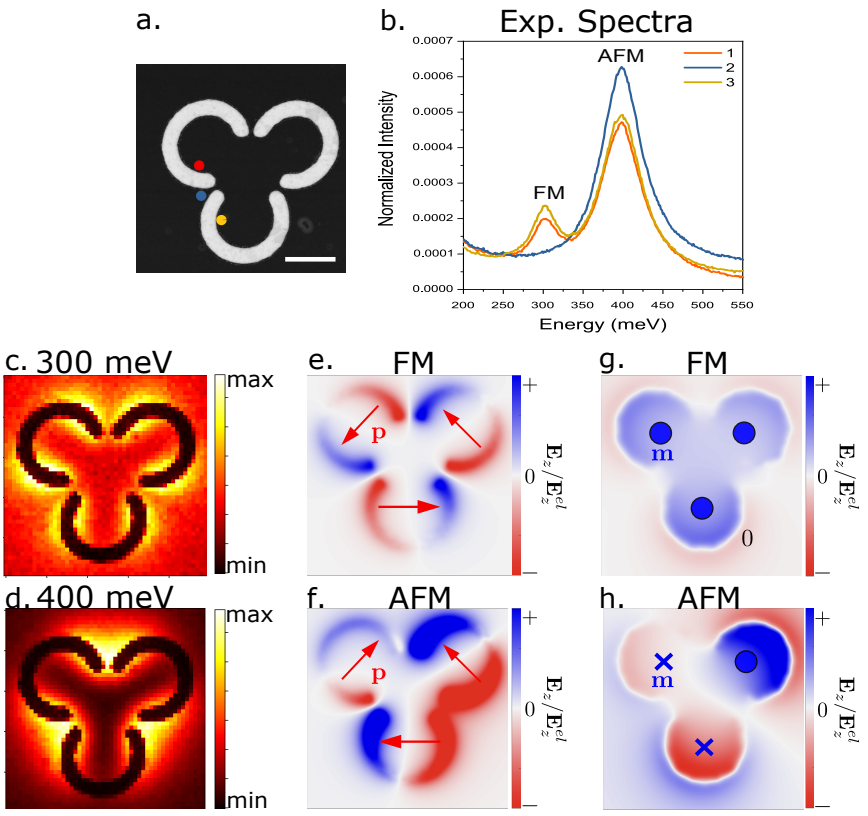

Figure 4.4: EEL point spectra, spectrum images, and induced electric and magnetic field profiles of a planar SRR trimer with D_{3h} symmetry. (a) HAADF image of the trimer. Scale bar = 300 nm. (b) Experimental EEL spectra acquired at the beam positions indicated in panel a. (c-d) Experimental spectrum images at the resonant energies of 300 meV and 400 meV with FM and AFM ordering, respectively, shown in the simulated field profiles of (e) the electric dipole in-phase lower-energy normal mode, (f) the electric dipole out-of-phase higher-energy normal mode, (g) the magnetic dipole in-phase lower-energy normal mode, (h) the magnetic dipole out-of-phase higher-energy normal mode.

4.4 Conclusion

In this paper, we combine STEM-EELS experiment with theoretical modeling to study the 3D geometric effects of electric and magnetic plasmon mode mixing in nanofabricated 3D SRR dimers with varying out-of-plane tilt angles. Spectral split-

ting of the normal modes arising from the 3D tilt has been interpreted by theoretically mapping the SRR electromagnetic responses onto effective dipole oscillators, with an effective coupling that reveals a competition between interactions mediated by electric and magnetic SRR dipole fields. Importantly, our results confirm that varying the 3D tilt angle between coupled SRRs diminishes the magnetic coupling, however, enhances the overall mode mixing, and for a certain planar orientation and tilt angle, the SRR dimer becomes uncoupled, with a response reminiscent of a single SRR. We have also described the influence of the electric dipole's circular current path on the magnetic ordering of a coupled SRR trimer arranged in a planar triangular D_{3h} symmetry, where the hybridized magnetic dipoles are ferromagnetically ordered in the lower-energy in-phase normal mode and anti-ferromagnetically ordered in the higher-energy out-of-phase normal mode. The EELS measurements and corresponding theoretical analysis presented in this study shed light on the rational design of a new class of NIR metamaterials formed from embedded 3D SRR units.

4.5 Materials and Methods

Planar SRR Fabrication. The planar split ring resonators are fabricated via electron-beam lithography (JEOL 9300FS) using a lift-off process. A 300 μm Si wafer with 30 nm of low pressure chemical vapor deposited SiNx is spin coated with PMMA 495 A4 and exposed. The pattern is then developed using methyl isobutyl ketone:isopropyl alcohol (IPA) (1:3). 25 nm of Au is sputter deposited via DC magnetron sputtering onto the substrate followed by soaking in a heated NMP bath, sonicating in NMP and acetone, and rinsing with IPA and deionized water. The backside of the wafer is then spin coated with P20 and S1818 and exposed using photolithography to create the windows of the TEM. Reactive ion etching is used to remove the backside nitride layer and the wafer is subsequently submerged in a heated KOH bath to etch the Si windows and TEM grid edges.

3D SRR Fabrication. 3D split ring resonators were fabricated using a hybrid

synthesis approach utilizing focused electron beam induced deposition (FEBID) as scaffold for plasmonic materials.[27] The FEBID scaffolds were subsequently coated with SiO_2 and Au. The 22 nm conformal SiO_2 layer was deposited via ALD to enhance the structural integrity of the scaffolds, which also isolates the Au layer from the PtC_x scaffold to minimize possible plasmon damping. Due to its well-known plasmonic properties as well as its stability in atmosphere, 25 nm Au was subsequently deposited on the scaffolds via dc magnetron sputtering (7 W, 3 mTorr).

Experimental STEM-EELS. Low-loss EEL spectra were collected using a Nion aberration-corrected high energy resolution monochromated EELS-STEM (Nion HERMES) operating at 100 kV accelerating voltage. Point spectra and spectrum images were collected with a convergence semiangle of 30 mrad and a collection semiangle of 15 mrad, with a beam current of ~ 8 pA [36, 37]. Scattered electrons were dispersed in a Nion Iris spectrometer at 1.2 meV/channel and the energy resolution (full width half maximum of the zero loss peak (ZLP)) was approximately 16 meV. Point spectra had their ZLP maxima normalized to unity.

Numerical EELS Simulations. Simulations of the EEL spectra were performed using the electron driven discrete dipole approximation (e-DDA) [38, 39]. The SRR shapes were modeled as toroids cut according to the geometry and dimensions of the experiment. We note that the nonmetal layers, substrates, and pillar were omitted to simplify the simulations. The electron beam energy was set at 100 keV, and the impact parameters for all spectra were taken between $9 - 12$ nm. The tabulated dielectric data for gold in Ref. [40] was used, and all field maps were calculated 45 nm above the plane containing the SRR structures.

4.6 Acknowledgements

G.P. and P.D.R. acknowledge support from the National Science Foundation under grant NSF DMR 1709275. Work at the University of Washington was supported by the U.S. National Science Foundation under Award Nos. CHE-1954393 and QII-

TAQS-1936100 (C.P.A., D.J.M.). All the authors acknowledge that the nanofabrication and high-energy resolution EELS measurements were conducted at the Center for Nanophase Materials Sciences, which is a DOE Office of Science User Facility. This research was conducted, in part, using instrumentation within ORNL's Materials Characterization Core provided by UT-Battelle, LLC, under contract no. DE-AC05-00OR22725 with the DOE, and sponsored by the Laboratory Directed Research and Development Program of Oak Ridge National Laboratory, managed by UT-Battelle, LLC, for the U.S. Department of Energy.

BIBLIOGRAPHY

[1] Mário G Silveirinha and Carlos A Fernandes. Nonresonant structured material with extreme effective parameters. *Physical Review B*, 78(3):033108, 2008.

[2] Richard W Ziolkowski. Propagation in and scattering from a matched metamaterial having a zero index of refraction. *Physical Review E*, 70(4):046608, 2004.

[3] John B Pendry, Anthony J Holden, David J Robbins, and WJ Stewart. Magnetism from conductors and enhanced nonlinear phenomena. *IEEE Transactions on Microwave Theory and Techniques*, 47(11):2075–2084, 1999.

[4] Yongmin Liu and Xiang Zhang. Metamaterials: a new frontier of science and technology. *Chemical Society Reviews*, 40:2494–2507, 2011.

[5] David R Smith, Willie J Padilla, DC Vier, Syrus C Nemat-Nasser, and Seldon Schultz. Composite medium with simultaneously negative permeability and permittivity. *Physical Review Letters*, 84(18):4184, 2000.

[6] Richard A Shelby, David R Smith, and Seldon Schultz. Experimental verification of a negative index of refraction. *Science*, 292(5514):77–79, 2001.

[7] David R Smith, John B Pendry, and Mike CK Wiltshire. Metamaterials and negative refractive index. *Science*, 305(5685):788–792, 2004.

[8] Vladimir M Shalaev. Optical negative-index metamaterials. *Nature Photonics*, 1(1):41–48, 2007.

[9] John Brian Pendry. Negative refraction makes a perfect lens. *Physical Review Letters*, 85(18):3966, 2000.

[10] JB Pendry and S Anantha Ramakrishna. Focusing light using negative refraction. *Journal of Physics: Condensed Matter*, 15(37):6345, 2003.

[11] John B Pendry, David Schurig, and David R Smith. Controlling electromagnetic fields. *Science*, 312(5781):1780–1782, 2006.

[12] Muamer Kadic, Graeme W Milton, Martin van Hecke, and Martin Wegener. 3d metamaterials. *Nature Reviews Physics*, 1(3):198–210, 2019.

[13] Hee-Jo Lee, Jung-Hyun Lee, Hui-Sung Moon, Ik-Soon Jang, Jong-Soon Choi, Jong-Gwan Yook, and Hyo-Il Jung. A planar split-ring resonator-based microwave biosensor for label-free detection of biomolecules. *Sensors and Actuators B: Chemical*, 169:26–31, 2012.

[14] Xinlong Xu, Bo Peng, Dehui Li, Jun Zhang, Lai Mun Wong, Qing Zhang, Shijie Wang, and Qihua Xiong. Flexible Visible–Infrared Metamaterials and Their Applications in Highly Sensitive Chemical and Biological Sensing. *Nano Letters*, 11(8):3232–3238, August 2011.

[15] Nanfang Yu, Francesco Aieta, Patrice Genevet, Mikhail A. Kats, Zeno Gaburro, and Federico Capasso. A broadband, background-free quarter-wave plate based on plasmonic metasurfaces. *Nano Letters*, 12(12):6328–6333, 2012.

[16] F. Falcone, T. Lopetegi, M. A. G. Laso, J. D. Baena, J. Bonache, M. Beruete, R. Marqués, F. Martín, and M. Sorolla. Babinet principle applied to the design of metasurfaces and metamaterials. *Physical Review Letters*, 93:197401, Nov 2004.

[17] Stanislav B Glybovski, Sergei A Tretyakov, Pavel A Belov, Yuri S Kivshar, and Constantin R Simovski. Metasurfaces: From microwaves to visible. *Physics Reports*, 634:1–72, 2016.

[18] Yongzhi Cheng, Helin Yang, Zhengze Cheng, and Nan Wu. Perfect metamaterial absorber based on a split-ring-cross resonator. *Applied Physics A*, 102:99–103, January 2011.

[19] Na Liu, Hui Liu, Shining Zhu, and Harald Giessen. Stereometamaterials. *Nature Photonics*, 3(3):157–162, 2009.

[20] David A Powell, Mikhail Lapine, Maxim V Gorkunov, Ilya V Shadrivov, and Yuri S Kivshar. Metamaterial tuning by manipulation of near-field interaction. *Physical Review B*, 82(15):155128, 2010.

[21] Na Liu and Harald Giessen. Coupling effects in optical metamaterials. *Angewandte Chemie International Edition*, 49(51):9838–9852, 2010.

[22] Na Liu, Stefan Kaiser, and Harald Giessen. Magnetoinductive and electroinductive coupling in plasmonic metamaterial molecules. *Advanced Materials*, 20(23):4521–4525, 2008.

[23] Felix von Cube, Stephan Irsen, Jens Niegemann, Christian Matyssek, Wolfram Hergert, Kurt Busch, and Stefan Linden. Spatio-spectral characterization of

photonic meta-atoms with electron energy-loss spectroscopy. *Optical Materials Express*, 1(5):1009–1018, Sep 2011.

[24] Felix von Cube, Stephan Irsen, Richard Diehl, Jens Niegemann, Kurt Busch, and Stefan Linden. From isolated metaatoms to photonic metamaterials: evolution of the plasmonic near-field. *Nano Letters*, 13(2):703–708, 2013.

[25] Qiuqun Liang, Yuren Wen, XiaoKe Mu, Thomas Reindl, Weixing Yu, Nahid Talebi, and Peter A. van Aken. Investigating hybridization schemes of coupled split-ring resonators by electron impacts. *Optics Express*, 23(16):20721, August 2015.

[26] Isobel C Bicket, Edson P Bellido, Sophie Meuret, Albert Polman, and Gianluigi A Botton. Correlative electron energy loss spectroscopy and cathodoluminescence spectroscopy on three-dimensional plasmonic split ring resonators. *Microscopy*, 67(suppl_1):i40–i51, 2018.

[27] Grace Pakeltis, Zhongwei Hu, Austin G Nixon, Eva Mutunga, C Praise Anyanwu, Claire A West, Juan Carlos Idrobo, Harald Plank, David J Masiello, Jason D Fowlkes, et al. Focused electron beam induced deposition synthesis of 3d photonic and magnetic nanoresonators. *ACS Applied Nano Materials*, 2(12):8075–8082, 2019.

[28] H Liu, DA Genov, DM Wu, YM Liu, JM Steele, C Sun, SN Zhu, and X Zhang. Magnetic plasmon propagation along a chain of connected subwavelength resonators at infrared frequencies. *Physical Review Letters*, 97(24):243902, 2006.

[29] Steven C. Quillin, Charles Cherqui, Nicholas P. Montoni, Guoliang Li, Jon P. Camden, and David J. Masiello. Imaging plasmon hybridization in metal nanoparticle aggregates with electron energy-loss spectroscopy. *The Journal of Physical Chemistry C*, 120(37):20852–20859, 2016.

[30] F. J. García de Abajo. Optical excitations in electron microscopy. *Reviews of Modern Physics*, 82(1):209, 2010.

[31] SS Seetharaman, CG King, IR Hooper, and WL Barnes. Electromagnetic interactions in a pair of coupled split-ring resonators. *Physical Review B*, 96(8):085426, 2017.

[32] David A Powell, Kirsty Hannam, Ilya V Shadrivov, and Yuri S Kivshar. Near-field interaction of twisted split-ring resonators. *Physical Review B*, 83(23):235420, 2011.

[33] H Liu, DA Genov, DM Wu, YM Liu, ZW Liu, C Sun, SN Zhu, and X Zhang. Magnetic plasmon hybridization and optical activity at optical frequencies in metallic nanostructures. *Physical Review B*, 76(7):073101, 2007.

[34] Frank Hesmer, Eugen Tatartschuk, Oleksandr Zhuromskyy, Anna A Radkovskaya, Mikahil Shamonin, Tong Hao, Chris J Stevens, Grahame Faulkner, David J Edwards, and Ekaterina Shamonina. Coupling mechanisms for split ring resonators: Theory and experiment. *Physica Status Solidi (b)*, 244(4):1170–1175, 2007.

[35] Kevin C Smith, Yueyang Chen, Arka Majumdar, and David J Masiello. Active tuning of hybridized modes in a heterogeneous photonic molecule. *Physical Review Applied*, 13(4):044041, 2020.

[36] Ondrej L Krivanek, Tracy C Lovejoy, Niklas Dellby, Toshihiro Aoki, RW Carpenter, Peter Rez, Emmanuel Soignard, Jiangtao Zhu, Philip E Batson, Maureen J Lagos, et al. Vibrational spectroscopy in the electron microscope. *Nature*, 514(7521):209–212, 2014.

[37] Jordan A Hachtel, Andrew R Lupini, and Juan Carlos Idrobo. Exploring the capabilities of monochromated electron energy loss spectroscopy in the infrared regime. *Scientific Reports*, 8(1):1–10, 2018.

[38] Nicholas W Bigelow, Alex Vaschillo, Vighter Iberi, Jon P Camden, and David J Masiello. Characterization of the electron-and photon-driven plasmonic excitations of metal nanorods. *ACS Nano*, 6(8):7497–7504, 2012.

[39] Nicholas W Bigelow, Alex Vaschillo, Jon P Camden, and David J Masiello. Signatures of fano interferences in the electron energy loss spectroscopy and cathodoluminescence of symmetry-broken nanorod dimers. *ACS Nano*, 7(5):4511–4519, 2013.

[40] Robert L Olmon, Brian Slovick, Timothy W Johnson, David Shelton, Sang-Hyun Oh, Glenn D Boreman, and Markus B Raschke. Optical dielectric function of gold. *Physical Review B*, 86(23):235147, 2012.